SISSA
Scuola
Internazionale
Superiore di
Studi Avanzati

Physics Area – PhD course in

Theory and Numerical Simulation of Condensed Matter

Simulating Plasmon Enhancement of Optical Properties in Hybrid Metal-Organic Nanoparticles

Candidate:

Jacopo Marcheselli

Advisor:

Marco Garavelli

Stefano Corni

Co-advisors:

Stefano Baroni

Academic Year 2018-19

"τί δ'ἐστὶ τοῦτο πρὸς ϑεῶν;"

Dam. fr. 1,2 K.-A

"To the chemist, colour is a bountiful clue to composition and, if measured carefully enough, can reveal delicate truths about molecular structure. It takes a particular turn of mind to see chromatic beauty lurking in the molecular structures of alizarin and indigo, to sense the rich hues within the stark, schematic depictions of these dye molecules. The Italian chemist and writer Primo Levi intimates how this relation between colour and constitution broadens the chemist's sensitivity to colour:
Per quella che è stata la mia esperienza, devo dire che la mia chimica, che poi era una chimica "bassa", quasi una cucina, mi ha fornito in primo luogo un vasto assortimento di metafore. Mi ritrovo più ricco di altri colleghi scrittori perché per me termini come "chiaro", "scuro", "pesante", "leggero", "azzurro" hanno una gamma di significati più estesa e più concreta. Per me l'azzurro non è soltanto quello del cielo, ho cinque o se azzurri a disposizione."

Philip Ball, *Bright Earth: The Invention of Colour*

SISSA

Abstract

Simulating plasmon enhancement of optical properties in hybrid metal-organic nanoparticles

by Jacopo MARCHESELLI

Hybrid organic-inorganic Nanoparticles (HNPs) are very interesting and widely studied materials, for their versatile applications in biotechnology and medicine, with high potential in biomedical imaging, gene and drug delivery, and photothermal cancer therapy, making them one of the most promising materials for early and accurate cancer diagnosis and effective cancer therapy. However, computing their physicochemical properties in details proves to be a challenge. While the nature of the organic component of the HNPs necessitates a full quantum chemical treatment, the size of the inorganic component renders this treatment computationally too expensive to be assessed with an homogeneous technique.

For this reason hybrid models have been developed combining a QM level treatment and a classical electromagnetism approach, respectively, for molecules and the inorganic nano-structures upon which they are adsorbed [1]. In particular, the inorganic component, usually a metal, is considered as a classical continuous body, characterized by its own frequency dependent dielectric function, for which the Maxwell equations are solved using the Boundary Element Method (BEM), while excitation energies due to the energy transfer from the molecule to the metal is evaluated exploiting Time Dependent Density Functional Theory (TDDFT).

After proving that the polarization charges distribution, used in BEM, well describe the optical properties of bare inorganic Nanoparticles, reproducing experimental spectra [2–4] of bare Gold Nanoparticles using BEM tools, we described the interactions of the organic molecular frame with the Nanoparticles. In order to reproduce the desired spectroscopic properties for the hybrid system we evaluated on one side the effects introduced by the presence of a Nanoparticle over the energies and the excited state dynamics of the isolated organic dyes (radiative and non radiative deactivation constants). On the other side we computed how the organic layer of dye and surfactant around the gold Nanoparticle affects the plasmonic excitation of the metallic subsystem adding this layer to the electrodynamic computations.

Contents

List of Figures

List of Abbreviations

BEM	**B**oundary **E**lement **M**ethod
DFT	**D**ensity **F**unctional **T**heory
EM	**E**lectro**M**agnetic
GGA	**G**eneral **G**radient **A**pproximation
GNB	**G**old **N**ano**B**ipyramids
HNP	**H**ybrid **N**ano**P**article
HOMO	**H**ighest **O**ccupied **M**olecular **O**rbital
LSPR	**L**ocal **S**urface **P**lasmon **R**esonance
LUMO	**L**owest **U**noccupied **M**olecular **O**rbital
NP	**N**ano**P**article
PBE	**P**erdew–**B**urke-**E**rnzerhof exchange-correlation functional
PCM	**P**olarizable **C**ontinuum **M**odel
QSA	**Q**uasi**S**tatic **A**pproximation
scf	**s**elf **c**onsistent **f**ield
SERS	**S**urface **E**nhanced **R**aman **S**cattering
TDDFT	**T**ime **D**ependent **D**ensity **F**unctional **T**heory
TDM	**T**ransition **D**ipole **M**oment
TEM	**T**ransmission **E**lectron **M**icroscope

Chapter 1

Introduction

Hybrid NanoParticles (HNP) are NanoSystems in which two or more disparate materials are combined, resulting in a joined system whose properties are not, usually, the simple sum of the single materials' features, and develop a synergistic interaction that allows to go beyond the range of capabilities of the individual components. These materials can be obtained using the most diverse mixes of substances of various nature, from the colloidal metals, semiconductor or insulating nanocrystals, molecular materials, etc. In particular, these properties have been demonstrated in two main categories: metal-semiconductor nanoparticles, where the metallic part is attached to an inorganic semiconductor nanocrystal, and metal-chromophore nanoparticles, where the metal nanoparticles is functionalized with organic chromophores adsorbed or grafted onto the surface of the metal, usually coated with a surfactant that mechanically isolates the system from the environment.

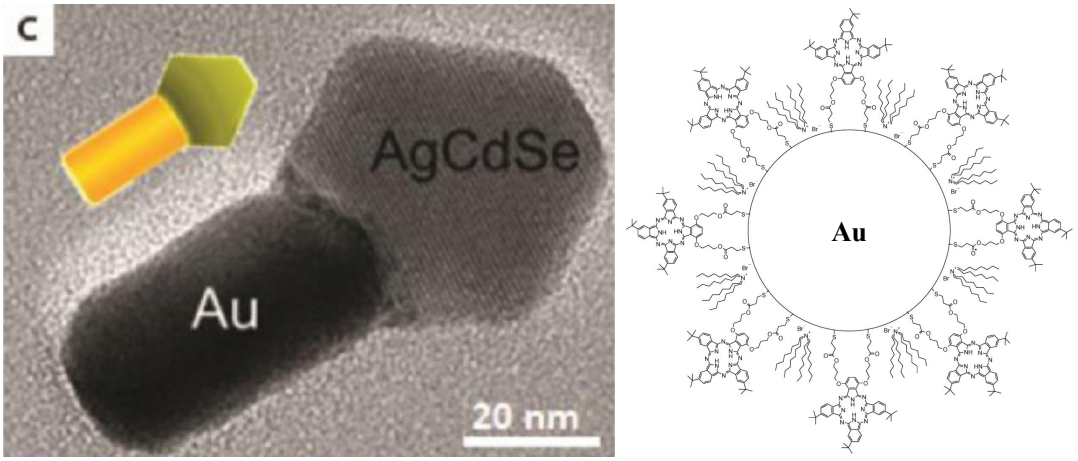

FIGURE 1.1: Two examples of hybrid nanoparticles: a TEM image of a metal NP + semiconductor on the left [5]; a schematic representation of a metal NP + chromophore on the right [6].

Hybrid nanoparticles present many interesting properties and capabilities: the easy tunability, the field enhancement properties, the charge transfer (CT), or energy transfer (ET) excited states, and the general robustness, allow for a incredibly wide variety of possible applications [7] Firstly, the easy tunability: the employment of metal nanoparticles allows for an extremely wide variety regarding the optical properties. Variations in size, shape, and element allow for covering all the electromagnetic spectrum, from far infrared to the UV, with different absorption wavelengths, spectrum broadening, spectrum shapes. In ref. [8] for example is shown how the

shape of similar sized Silver nanoparticles greatly affects the absorption spectrum: while spheres possess a quite narrow spectrum, Ag wires and cubes have a much broader and more complex spectrum shape, being noticeably blue and red shifted, respectively. In ref. [9] are presented optical spectra of gold nanospheres with different diameters, with a strong red shift for larger nanoparticles. In ref. [10] is presented an extensive discourse of the capabilities of this kind of tuning: size, shape and materials are compared, showing that the spectral variability is very huge. Even within the same shape family different aspect ratios, features and proportions can modify the optical properties [2, 3, 11–16]. On the other side of the hybrid, also the variety of organic chromophores available give enormous freedom in choosing the most fitting pairs of organic and inorganic materials to best achieve the desired properties. In ref. [17] silver nanoparticles were coupled with different chromophores, achieving interesting results in modifying the properties of either the silver nanoparticles and the organic chromophores. In particular, as can be seen in fig. 1.2, the chromophores were composed of the same backbone structure, a porphyrin, functionalized with aminophenyl, carboxyphenyl, and metylphenyl synthons. The optical spectra clearly show that the combined systems have very different absorption properties with respect to the single materials isolated, and, more importantly, simply changing the substituent on the porphyrin modifies the behaviour of the hybrid nanoparticle.

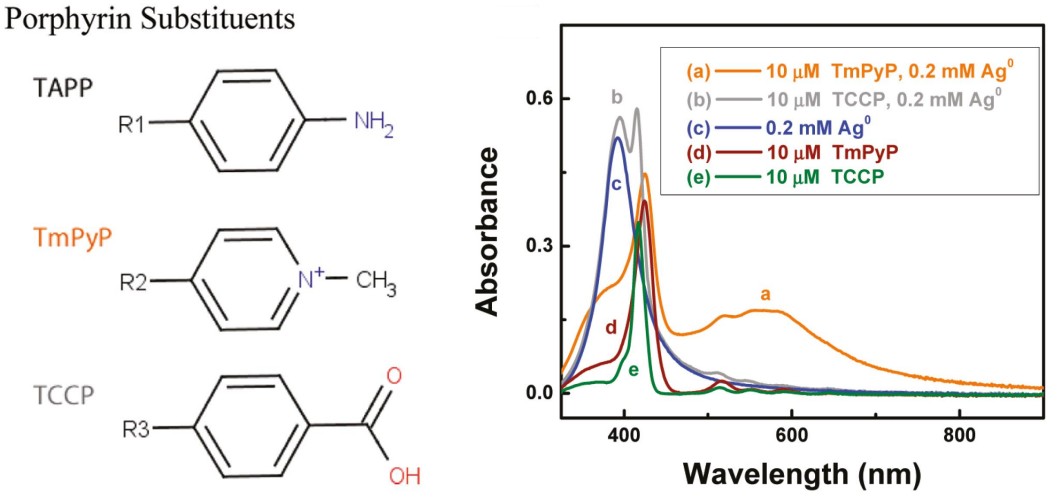

FIGURE 1.2: Substituent effects on ground state absorption spectra for hybrid NPs, bare silver NPs and organic molecules in solution [17].

The main mechanism underlying the different optical behaviour of metal nanoparticles, with respect to bulk metal, is called plasmon resonance, more specifically Local Surface Plasmon Resonance (LSPR). A plasmon resonance is a coherent non-propagating excitation of the conduction electrons in small metallic particles at the sub-wavelength scale. When light hits a nanoparticle, the surface of the metal actively exerts a restoring force on the oscillating electromagnetic field, leading to a resonance, and to field amplifications around the vicinity of the nanoparticle. This causes a very important property of hybrid nanoparticles: field enhancement. As it is displayed in ref. [5], from which fig.1.3 is extracted, the extinction cross section of a

suspension of hybrid nanoparticle of CdS nanorods combined with Gold nanoparticles (thick black line, green area) is more intense than either a suspension of just CdS nanorods (dashed black curve), a suspension of just Gold nanoparticles (red dotted curve and yellow area), and a mixture of Gold nanoparticles and CdS nanorods (thin black curve, yellow and blue area), all with similar sizes with the hybrid nanoparticles. This means that the two components joint together enhance each other's cross section, increasing the amount of light absorbed for comparable sizes.

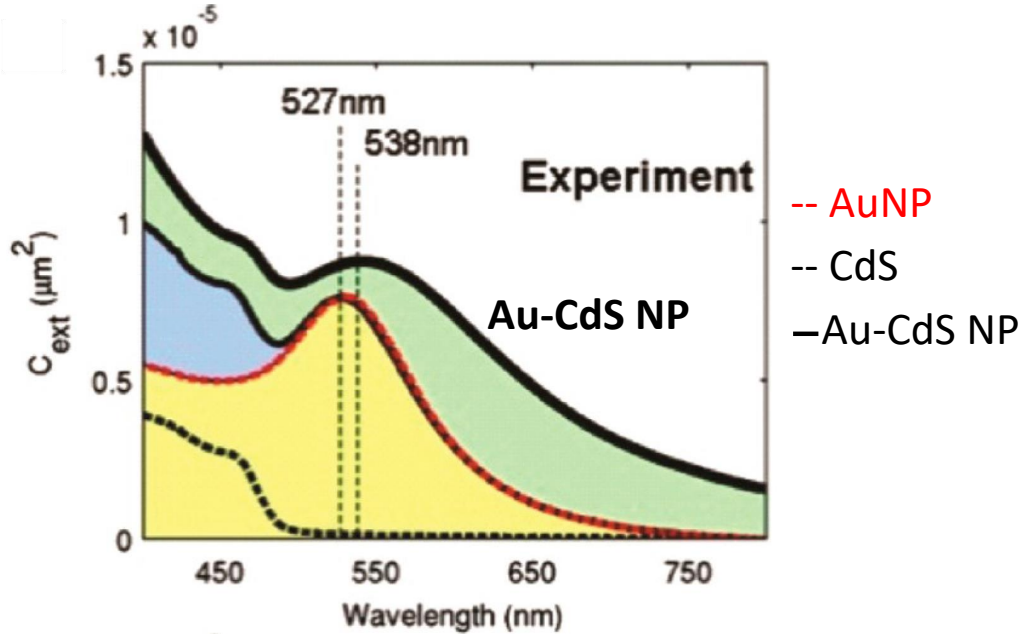

FIGURE 1.3: Enhanced absorption of the hybrid systems with respect to isolated single components [5].

Another important consequence of the plasmonic behaviour of metal nanoparticles, when joined with organic semiconductors, is the ability to strongly couple the molecular electronic transitions with the plasmon resonance, forming hybrid excited states [18]. This can lead to energy or charge transfer phenomena that can heavily vary electrochemical and optical properties of the chromophores involved, leading to many desirable applications. One example is seen in ref. [17]: in fig. 1.4 are represented the pump-and-probe femtosecond transient absorption spectra of amynophenylporphyrin in solution in neat form (on the left, A), and when attached to Silver nanoparticles (on the right, B), showing a clear disappearance of one of the absorption bands increasing the probing delay, when the bands are stable and unperturbed when the molecule is alone in solution.

All these properties lead to a long list of possible applications for these systems, ranging from reaction catalysis, enhancement of optical signals, solar cells, and many biotechnological employments. The catalysis of reactions can spread to many applications: photodegradation of pollutants [19, 20], photosynthesis of organic molecules [21, 22], photocatalytic production of Hydrogen from water, as a potential clean energy source [23, 24], and the photocatalitic reduction of CO_2 [25]. All these applications are based on two main mechanisms, illustrated in fig. 1.5: the energy transfer from the metal to the semiconductor due to the field enhancement

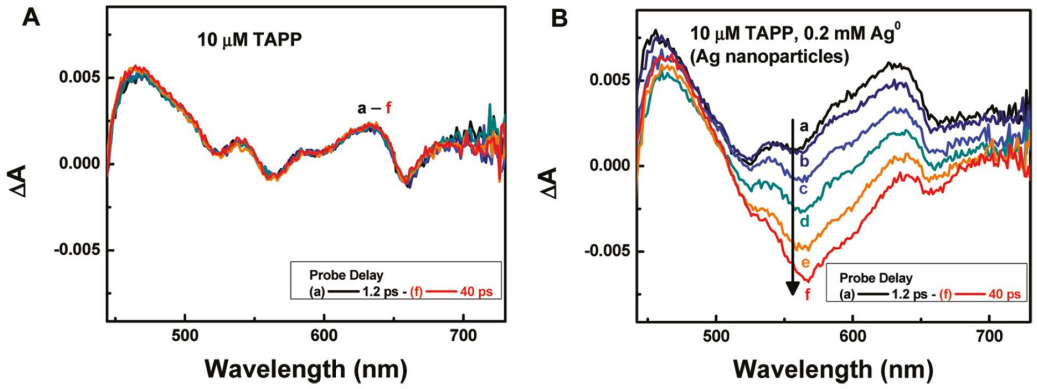

FIGURE 1.4: Charge transfer observed in hybrid organic-inorganic molecules, as seen in [17].

from the plasmon (fig. 1.5a), and the charge transfer (fig. 1.5b) due to the pouring of hot electrons from the metal into the conduction band (fig. 1.5c, for inorganic semiconductors, while for organic chromophores it would be the LUMO).

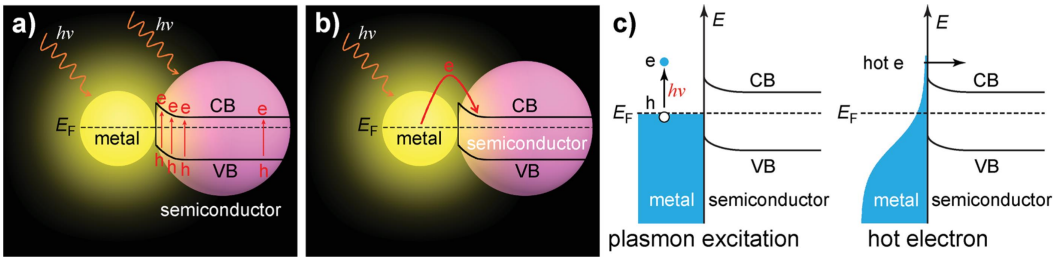

FIGURE 1.5: CT and ET mechanisms for plasmon enhanced photoactivated chemical reactions, as presented in ref. [7].

A fundamental application of hybrid organic-inorganic systems is the enhancement of optical signals, in particular for photoluminescence. The intense amplification of the electric field in the proximity of the metal, as seen earlier, can considerably increase the optical cross section of the attached semiconductor, being it either organic or inorganic. While the local field enhancement always bring an enhancing effect on the absorption of nearby molecules, increasing the excitation rate, on the other hand the effects on emission are less obvious. In principle the presence of a metallic surface should quench the radiative transitions, opening a non-radiative decay path through energy or charge transfer, but, on the other hand, near field enhancement should amplify the emission intensity of the radiative emissions as well as the excitations. The net effect is highly dependent on geometrical factors, such as the distance and the orientation of the molecules with respect to the metallic surface, and on the nature of the involved materials. A positive gain in photoluminescence intensity has been observed in many cases. In fig. 1.6 are presented two examples: on the left (ref. [26]), hybrid nanoparticles composed of Ag nanoparticles and ZnO nanorods show a strong increase in luminescence with respect to the ZnO rods alone; on the right (ref. [27]) Au–CdS core-shell nanoparticles, specifically designed for emission enhancement, present a photoluminescence intensity that is more than a whole order of magnitude increased with respect to bare CdS nanoparticles.

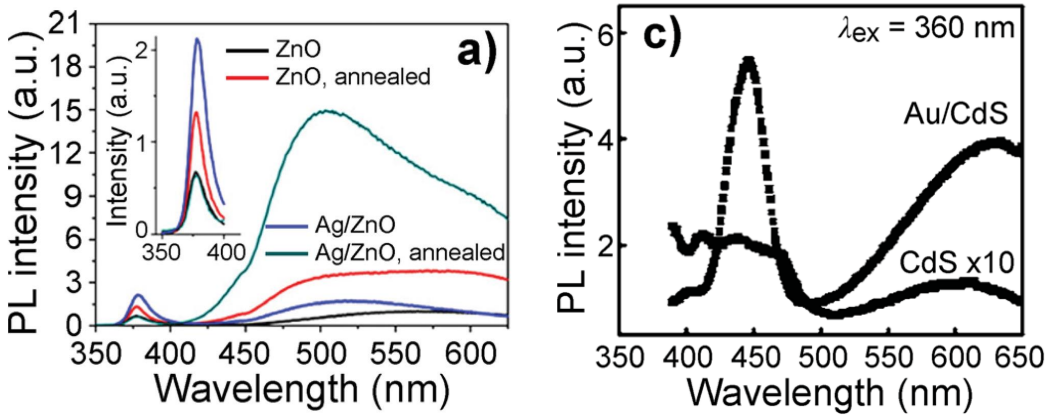

FIGURE 1.6: Photoluminescence enhancement in Ag/ZnO (left) and Au/CdS hybrid nanoparticles, as presented in refs. [26] and [27].

These are very important features of hybrid nanoparticles, allowing for strongly increasing optical signals in probes, markers, switches, and all the enormous amount of engineering or biomedical applications, such as diagnostic, imaging, and therapy. One example is presented in ref. [28], where a nanocomposite with a core of Fe_3O_4 and a Gold shell is easily prepared and applied to mice, showing great potential for magnetic resonance imaging (MRI)-guided photothermal therapy for tumor treatment, under near-IR laser radiation, presenting a strong effect, when the bare Fe_3O_4 show near to none heating on the target area of the ill mice, either under confocal microscopy *in vitro* and infrared thermal imaging *in vivo*. This is a fundamental point: *in vivo* applications of photophisical or photochemical processes are usually very difficult and rare, since light mildly penetrates organic tissues, forcing to either use high concentrations or high irradiation intensity, and limiting the medical applications to the skin, or laser surgery. In this regard, hybrid nanoparticles can be even functionalized with proteins that are tailored to bind to desired target, as is presented in ref. [29]. There, dark field imaging shows how free prostate-specific antigen conjugated with Fe_3O_4/Au nanoshells present a stronger cellular uptake with respect to the bare Fe_3O_4 nanoparticles, working well as constrast agents as well, and a much stronger phototermal effetc.

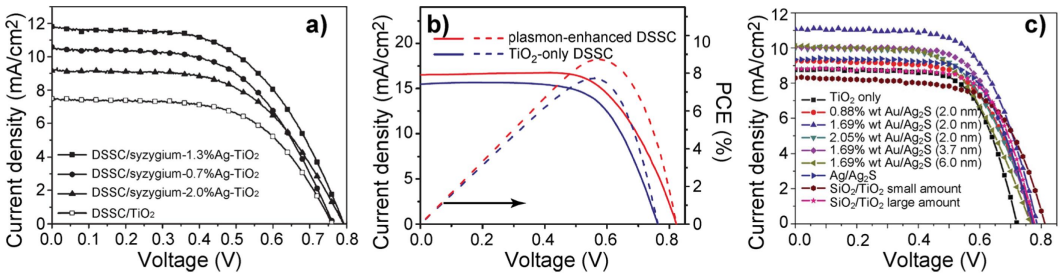

FIGURE 1.7: Solar cell performance improvement, probed by current density, due to the hybrid nanostructures, as presented in refs. [30] (a), [31] (b), and [32] (c).

Another field where the strong absorption enhancement, due to the near field effects of the plasmonic behaviour of the metallic counterpart, is very promising is

in solar cells. In fig. 1.7 are presented a few examples from various references ([30–32]) of plasmonic enhancement of the performance of TiO_2 Die Sensitized Solar Cells (DSSC), where the presence of Silver or Gold nanoparticles strongly increase the current density, and therefore the efficiency of the cells.

Considering the great interest of these systems, the goal of this work is to provide a theoretical model to compute optical properties exploiting various methods present in literature. In particular the focus will be on hybrid organic-inorganic nanoparticles where the metal is Gold. The choice of the metal is easily explained: it is hugely present in the literature, with a multitude of shapes and sizes (see fig.1.8), and the possibility of handily functionalize the metallic surface with molecules, exploiting the covalent bonding of Gold with thiolic groups, or the non-covalent bond that forms with amines.

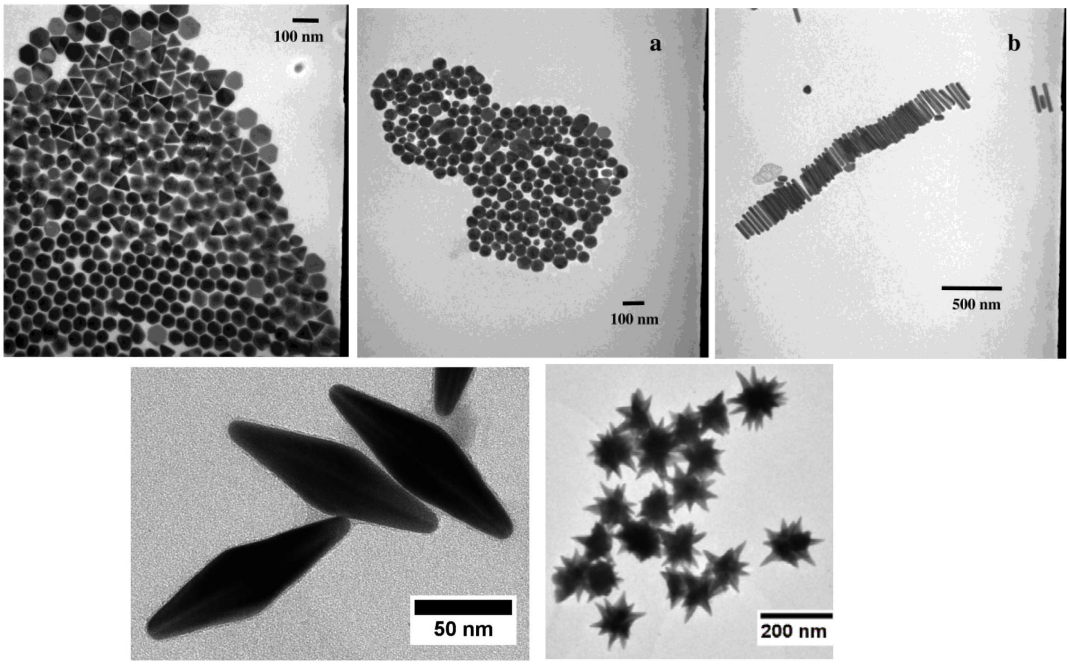

FIGURE 1.8: A collection of Gold nanoparticles in various shapes and sizes, ranging from spheres, pyramids, octahedra, rods, to bipyramids, and stars. refs. [16], and [11]

The model development will tackle the problem from various angles. In chapter 3 we probed the potential of using Gold nanoclusters, up to a few tenth of atoms, to simulate the interaction between the molecular and metallic portions, *via* TDDFT. This method, though, is bound to fail since the affordable sizes for the metallic counterpart are too small to actually observe a proper plasmonic behaviour of the nanoclusters, considering the current state of computational power for TDDFT. Then, we resorted to a purely classical representation of the Gold nanoparticle. In chapter 4 we narrowed the interest over Gold nanobipyramids to check the capabilities of the Boundary Element Method (BEM) technique to classically compute electromagnetic scattering of bare Gold nanoparticles in solution, applying it over a class of nanoparticles that were not previously investigated with this technique. The result is that BEM is a very accurate approach for this class of nanoparticles, provided an accurate modelization of their geometry by means of a surface. Another goal of proving

the BEM model accurate for this class of nanoparticles is a preliminary validation for the hybrid nanoparticle model. In literature have been presented many instances in which the interaction between the metal nanoparticle and the organic chromophore is modelled from a Polarizable Continuum Model (PCM) standpoint: the electrostatic effects of the metal over the molecular excitations are represented by the polarization charges in the PCM model and their interaction with the molecular transition densities, computed with a quantum mechanical method, in this case DFT. In chapter 5 we employed an even simpler model: the exciting molecule is seen as a point-like transition dipole moment, allowing for swiftly probing the effects over the molecular optical properties of positioning, distance, orientation, and transition energy, between the molecule and the nanoparticles. This allows to building up the tools to construct a theoretical database with qualitative instructions to maximize some desired features regarding the synthesis of hybrid Gold-dye Nanoparticles, how to chose the gold NPs, the dyes and where to put them onto the surface, either when fluorescent emission and the absorption are taken into account. The last step is to probe if the classical electrodynamic model is a good approximation to affordably describe the hybrid system as a whole. The hybrid system is then divided in three parts: the gold NP, described from its surface by a mesh using experimental dielectric function; the layer composed by the dye and the surfactant, described with an outer-shell surface, filled with an effective dielectric function, which can be computed using quantum mechanics, exploiting effective models such as Maxwell-Garnett, or given experimentally; last, the solvent, described by its relative dielectric permittivity. This is presented in chapter 6.

Chapter 2

Theoretical background

2.1 Density Functional Theory

Density functional theory is a fundamental tool for chemists and physicists. In its primary implementation, it provides a way to compute ground-state electronic structures, based on the electron density distribution $\rho(\boldsymbol{r})$. Applying the mathematical tools of mean-field theory to the solution of Schrödinger equation expressed in terms of $\rho(\boldsymbol{r})$, instead of the electronic wavefunction, leads to an exact theoretical solution, which unfortunately can be applied only in an approximated way, in real world scenarios. The main sources for writing this paragraph are: [33–42], and lecture notes from [43].

2.1.1 Hohenberg and Kohn Theorems

The Schrödinger equation is: $\hat{H}\psi = E\psi$, where the Hamiltonian operator is $\hat{H} = \hat{T} + \hat{U}_{ext} + \hat{V}_{ee}$. The Ritz variational theorem states that the Schrödinger functional $E[\Psi] = \langle \Psi | \hat{H} | \Psi \rangle$ is stationary around the eigenfunctions of the Schrödinger equation, if the eigenfunctions Ψ are normalized, which means that the functional derivative of the Schrödinger functional must be zero

$$\frac{\delta E[\Psi]}{\delta \Psi} = 0 \Rightarrow \hat{H}\Psi = \varepsilon\Psi \tag{2.1}$$

Where ε is the energy eigenvalue.
For a molecular system of N electrons and M nuclei, applying the Born-Oppenheimer approximation, the wavefunction Ψ is:

$$\Psi = \Psi(\boldsymbol{r}_1, \ldots, \boldsymbol{r}_N) \tag{2.2}$$

The kinetic energy operator $\hat{T}$ is:

$$\hat{T} = -\frac{1}{2}\sum_{i=1}^{N} \nabla_i^2 \tag{2.3}$$

The electron-electron repulsion is:

$$\hat{V}_{ee} = \sum\sum_{i<j} \frac{1}{r_{ij}} \tag{2.4}$$

And the external potential due to the M nuclei is:

$$\hat{\upsilon}_{ext} = -\sum_{i=1}^{N}\sum_{A=1}^{M}\frac{Z_A}{|\boldsymbol{R}_A - \boldsymbol{r}_i|} \tag{2.5}$$

The presence of $\hat{V}_{ee}$ makes the solution of the Schrödinger equation impossible for many body-problems. One way to tackle this hurdle is bypass the calculation of the N electron wavefunction using the electron density ρ, defined as:

$$\rho(\boldsymbol{r}) = N\langle\Psi|\,\hat{\rho}(\boldsymbol{r})|\Psi\rangle \tag{2.6}$$

Where $\hat{\rho}(\boldsymbol{r})$ is an operator that counts the number of electrons in a given point of space: $\hat{\rho}(\boldsymbol{r}) = \sum_i \delta(\boldsymbol{r} - \boldsymbol{r}_i)$ with δ being the Dirac delta. Then the expectation value at each point of space is:

$$\rho(\boldsymbol{r}) = \int d\boldsymbol{r}_1 \ldots d\boldsymbol{r}_N |\Psi(\boldsymbol{r}_1, \ldots, \boldsymbol{r}_N)|^2 \sum_{i=1}^{N}\delta(\boldsymbol{r} - \boldsymbol{r}_i) \tag{2.7}$$

Since the wavefunction is antisymmetric, any of the spatial coordinate can be left out of the integration, giving:

$$\rho(\boldsymbol{r}) = N\int d\boldsymbol{r}_1 \ldots d\boldsymbol{r}_N |\Psi(\boldsymbol{r}_1, \ldots, \boldsymbol{r}_N)|^2 \tag{2.8}$$

For a given set of nuclear positions, the external potential is:

$$\hat{\upsilon}_{ext} = \sum_i \upsilon_{ext}(\boldsymbol{r}_i) = \int \hat{\rho}(\boldsymbol{r})\upsilon_{ext}(\boldsymbol{r})d\boldsymbol{r} \tag{2.9}$$

Therefore: $\langle\Psi|\hat{V}|\Psi\rangle = \int \upsilon_{ext}(\boldsymbol{r})\langle\Psi|\,\hat{\rho}(\boldsymbol{r})|\Psi\rangle d\boldsymbol{r} = \int \rho(\boldsymbol{r})\upsilon_{ext}(\boldsymbol{r})d\boldsymbol{r}$.
The total energy E can then be written as:

$$E = \langle\Psi|\hat{H}|\Psi\rangle = \int \rho(\boldsymbol{r})\upsilon_{ext}(\boldsymbol{r})d\boldsymbol{r} + \langle\Psi|\hat{T} + \hat{V}_{ee}|\Psi\rangle \tag{2.10}$$

This shows that the total energy depends on the external potential υ through a linear coupling to the electron charge density. Therefore the functional derivative of E with respect to υ is:

$$\rho = \frac{\delta E[\upsilon]}{\delta\upsilon} \tag{2.11}$$

Making the energy E a *functional* of the electronic density of the ground state. For a given external potential υ_{ext} then $E = E[\rho(\boldsymbol{r})]$. The first Hohenberg-Kohn theorem states that this relation between E and ρ is biunivocal, meaning that it is not possible to find two different densities that will give the same energy:

$$E[\rho_1] \neq E[\rho_2] \;\text{ if }\; \rho_1 \neq \rho_2$$

The total energy E can then be separated in two parts:

$$E[\rho] = \int \rho(\boldsymbol{r}) \upsilon_{ext}(\boldsymbol{r}) d\boldsymbol{r} + \langle \Psi | \hat{T} + \hat{V}_{ee} | \Psi \rangle = \int \rho(\boldsymbol{r}) \upsilon_{ext}(\boldsymbol{r}) d\boldsymbol{r} + F[\rho]$$

Where $F[\rho]$ is a universal functional that depends only on ρ and not from the external potential υ_{ext}, and is called *Hohenberg-Kohn functional*. Combining all these pieces and applying the variational principle it can be stated that:

$$E[\rho] = \min_{\rho} \{F[\rho] + \int \rho(\boldsymbol{r}) \upsilon_{ext}(\boldsymbol{r}) d\boldsymbol{r}\} \tag{2.12}$$

Which is the *second Hohenberg-Kohn theorem*

2.1.2 Kohn-Sham solution

The ground state energy is then the minimum over a functional upon three dimensions (the H-K functional) summed to the coupling between the conjugate variables U and ρ. This procedure transformed the wavefunction many-body problem into a different variational principle with a limited number of variables. The main issue of the procedure is that the H-K functional, although being exact and universal, has no obvious explicit form for any given problem. Kohn and Sham developed a way to develop this framework into a practically applicable procedure. Starting from Eq.2.12, finding the minimum means that the functional derivative $\delta E[\rho]/\delta\rho = 0$, therefore:

$$\frac{\delta F[\rho]}{\delta \rho(\boldsymbol{r})} + \upsilon_{ext}(\boldsymbol{r}) = \begin{cases} 0 & \text{if normalized } \left(\int \rho(\boldsymbol{r}) = N\right) \\ \mu & \text{if not normalized} \end{cases}$$

Rearranging $F[\rho] = T_0[\rho] + (F[\rho] - T_0[\rho])$, with $T_0[\rho]$ being the ground state kinetic energy of the non-interacting electrons inside the external potential υ_{ext}, then:

$$\frac{\delta T_0[\rho]}{\delta \rho} + \frac{\delta}{\delta \rho}(F[\rho] - T_0[\rho]) + \upsilon_{ext}(\boldsymbol{r}) = \mu \tag{2.13}$$

The second Hohenberg-Kohn theorem reassures that it exists only one system of non-interacting electrons that has the same ρ as the initial many-body problem. The main issue at this stage is to find the right approximation, which can be done by first splitting the system into known parts and leaving out as an additional term what cannot be computed. Since most of the term $\hat{V}_{ee}$ is due to the coulombic interaction of the charge density with itself, it can be expressed using the Hartree coulombic energy from Hartree-Fock, coming from the classical electrostatic repulsion of an electron density with itself. Then $F[\rho]$ can be further expanded into:

$$F[\rho] = T_0[\rho] + \underbrace{\frac{1}{2}\int \frac{\rho(\boldsymbol{r})\rho(\boldsymbol{r}')}{|\boldsymbol{r}-\boldsymbol{r}'|} d\boldsymbol{r} d\boldsymbol{r}'}_{E_H} + \underbrace{(F[\rho] - T_0[\rho] - E_H[\rho])}_{E_{xc}} \tag{2.14}$$

With E_H being the Hartree coulombic energy and E_{xc} the exchange correlation energy, which represent all the terms that cannot be computed exactly. Therefore the expression 2.13 becomes:

$$\frac{\delta T_0}{\delta \rho} + \frac{\delta E_H}{\delta \rho} + \frac{\delta E_{xc}}{\delta \rho} + \upsilon_{ext}(\boldsymbol{r}) = \mu \tag{2.15}$$

Allowing the definition of an effective potential υ_{eff} as:

$$\upsilon_{eff} = \upsilon_{ext} + \upsilon_H + \upsilon_{xc} \tag{2.16}$$

With:

$$\upsilon_H[\rho(\boldsymbol{r})] = \frac{\delta E_H[\rho(\boldsymbol{r})]}{\delta \rho} = \int \frac{\rho(\boldsymbol{r'})}{|\boldsymbol{r} - \boldsymbol{r'}|} d\boldsymbol{r}$$

And:

$$\upsilon_{xc}[\rho(\boldsymbol{r})] = \frac{\delta E_{xc}[\rho(\boldsymbol{r})]}{\delta \rho(\boldsymbol{r})}$$

Then the total energy of the electronic system can be written as:

$$E[\rho(\boldsymbol{r})] = \int \rho(\boldsymbol{r}) \upsilon_{ext}(\boldsymbol{r}) d\boldsymbol{r} + T_0[\rho(\boldsymbol{r})] + E_H[\rho(\boldsymbol{r})] + E_{xc}[\rho(\boldsymbol{r})] \tag{2.17}$$

All of these terms, except the exchange-correlation one, can be calculated from the wavefunction of the non-interacting system. Equation 2.17 serves also as a definition for the exchange-correlation potential, since it represent the quantity which, added to the non-interacting solution, result into the fully-interacting energy and electron density. If E_{xc} was known exactly, the total energy could be minimized with respect to the density ρ. This leads to the Kohn-Sham equations, that can be solved self-consistently:

$$\left[-\frac{1}{2}\nabla^2 + \upsilon_{eff} \right] \varphi_n(\boldsymbol{r}) = \varepsilon_n \varphi_n(\boldsymbol{r}) \tag{2.18}$$

Where $\varphi_n(\boldsymbol{r})$ is the one-electron orbital. Equation 2.18 needs to be solved for as many states as there are electrons. The wavefunction of this non-interactive system isthe determinant composed from the orbitals φ_n:

$$\Psi = \det|\varphi_1 \varphi_2 \dots \varphi_N| \tag{2.19}$$

Ψ, thought, is not the wavefunction of the real systema, and neither the φ_n. The total electron density can be computed exploiting the non interaction of the single-electron orbitals and therefore is:

$$\rho(\boldsymbol{r}) = \sum_n |\varphi_n(\boldsymbol{r})|^2 \tag{2.20}$$

The Kohn-Sham procedure consists in a series of steps:

1. guess $\rho_{in}(\boldsymbol{r})$
2. from $\rho_{in}(\boldsymbol{r})$ compute $\upsilon_{eff} = \upsilon_{ext} + \upsilon_H + \upsilon_{xc}$

3. solve K-S equation $\left[-\frac{1}{2}\nabla^2 + \upsilon_{eff}\right]\varphi_n(\boldsymbol{r}) = \varepsilon_n\varphi_n(\boldsymbol{r})$
4. compute $\rho_{out} = \sum_n |\varphi_n|^2$
5. $\rho_{out} = \rho_{in} \pm \Delta\rho$ where $\Delta\rho$ is the convergence parameter
6. $\rho_{in} = \rho_{out}$ and the start again from 1.

2.1.3 Exchange-Correlation Functionals

The premises of DFT, up to this point, do not provide any information on the structure of the exchange-correlation functional, which is unknown. The only known solution is the one of the homogeneous electron gas, where the density is just a single parameter which is the same in all the system. The XC functional then becomes a function and allows for an exact solution, but no real system is so well-behaved. One approach is to consider the electron density not as uniform, but as varying very smoothly. This way the system can be divided in many subsystems, each one with a fixed energy density e, and with small changes between neighbouring subsystems. In general, for a non-homogeneous system, $E_{tot} = \int e(\boldsymbol{r})d(\boldsymbol{r})$, and the distribution depends on the properties of all the system, but, if the electron density varies smoothly, the energy density of the volume of the subsystem can be approximated to the energy of a system that has the same density of the volume everywhere:

$$E(n) = N \cdot \varepsilon(n) \tag{2.21}$$

Where N is the number of electrons and $\varepsilon(n)$ is the energy per electron at that given electron density. This is true only for homogeneous systems, but can be used as an approximation if the density has very small variations within the system itself. Then the total energy becomes:

$$E(n) = \int dE = \int dN \cdot \varepsilon = \int \varepsilon\left[n(\boldsymbol{r})\right] n(\boldsymbol{r}) d\boldsymbol{r} \tag{2.22}$$

This is the main idea behind the Local Density Approximation, or LDA. This approximation turns out to be fairly good when applied to the exchange-correlation potential υ_{xc}. In this picture, the exchange-correlation functional is:

$$E_{xc}^{LDA}\left[\rho\right] = \int \varepsilon_{xc}\left[\rho(\boldsymbol{r})\right] \rho(\boldsymbol{r}) d\boldsymbol{r} \tag{2.23}$$

Where $\varepsilon_{xc}\left[\rho(\boldsymbol{r})\right]$ is an empirical parameter that is extracted from the difference in energy per particle between a homogeneous electron gas, at density n, and independent electrons. The functional derivative gives the LDA exchange correlation potential:

$$\upsilon_{xc}^{LDA} = \varepsilon_{xc}\left[\rho(\boldsymbol{r})\right] + \rho(\boldsymbol{r})\varepsilon'_{xc}\left[\rho(\boldsymbol{r})\right] \tag{2.24}$$

LDA is asymptotically exact in two limits:

- For very large densities $\rho(\boldsymbol{r}) \cdot a_0^3 \gg 1$

- For slowly varying densities $\frac{\Delta\rho(\boldsymbol{r})}{\rho(\boldsymbol{r})} \ll k_F(\boldsymbol{r})$

Where $k_F(\boldsymbol{r}) = \left(3\pi^2\rho(\boldsymbol{r})\right)^{1/3}$ is the local Fermi momentum.
While LDA shows predictive capabilities far beyond the expectations set from the defining constraints, many real materials, and especially molecular systems, require a much deeper parametrization of the exchange-correlation functional. Many examples have been developed in time, such as the Generalized Gradient Approximation(s), where the correlation energy per particle is extended to depend not only on the density, but also on the density gradients, or the Hybrid Functionals, where the XC functional is complemented, at various degrees, by the Hartree exact exchange term taken from Hartree-Fock. In any case, all of these implementations are based on empirical terms and have wide ranges of applications and drawback, making the XC functional landscape very widely varying and widespread.

2.1.4 Time-Dependent Density Functional Theory

DFT is a very powerful tool that allows to compute many ground state properties of rather large systems with small or reasonable computational effort, but, since its formulation is based on the static electron density and time independent Schrödinger equation, it lacks the ability to give insights on non-static properties of matter such as excited states. This introduced the necessity to develop a set of tools to go beyond the only-ground state description. Time-Dependent Density Functional Theory (TDDFT) was derived to complete such a task. As DFT begins with time-indepentend Schrödinger equation, TDDFT is rooted in time-dependent Schrödinger equation:

$$\hat{H}(t)\Psi(t) = i\frac{\partial\Psi(t)}{\partial t} \tag{2.25}$$

For this relation, the Runge-Gross theorem states that it exists a unique mapping between the external time-dependent potential $v(\boldsymbol{r},t)$ and the electronic density $\rho(\boldsymbol{r},t)$: for any given initial condition and any given potential, it exists only a unique timed-dependent density that satisfies the relation. This therefore become a unique and well-defined evolution, and this represents for TDDFT the equivalent of what H-K theorem is for DFT. Given a timed-dependent density $\rho(\boldsymbol{r},t)$ and a timed-dependent wavefunction $\Psi(t)$, the relation:

$$\rho(\boldsymbol{r},t) = \langle\Psi(t)|\,\hat{\rho}(\boldsymbol{r})|\Psi(t)\rangle \tag{2.26}$$

Since the Runge-Gross theorem states that this mapping can be inverted, then for any electron density and wavefunction at time 0:

$$\forall\rho(\boldsymbol{r},t)\wedge\Psi\left(t=0\right):\langle\Psi\left(0\right)|\,\hat{\rho}(\boldsymbol{r})|\Psi\left(0\right)\rangle = \rho\left(\boldsymbol{r},0\right) \tag{2.27}$$

$$\Rightarrow \exists! \quad v(\boldsymbol{r},t) : v(\boldsymbol{r},t) \mapsto \rho(\boldsymbol{r},t)$$

Since the R-G theorem holds for any form of coulombic potential, the choice of V_{ee} does not change the relation presented above, therefore the simplest choice is

assign to it a null value. Here it was assumed that the initial conditions entail an unperturbed potential, which is equivalent to assume that the initial conditions are the ground-state of the DFT calculation of the same system. The time-dependent Kohn-Sham (or better called Runge-Gross) equations become then:

$$\rho(\boldsymbol{r},t) = \sum_{v} |\varphi_v(\boldsymbol{r},t)|^2 \tag{2.28}$$

Where the timed-dependent orbitals $\varphi_v(\boldsymbol{r},t)$ satisfy the timed-dependent relation:

$$i\frac{\partial \varphi_v(\boldsymbol{r},t)}{\partial t} = \left[-\frac{\nabla^2}{2} + \upsilon_{ks}(\boldsymbol{r},t)\right]\varphi_v(\boldsymbol{r},t) \tag{2.29}$$

Where the Kohn-Sham potential $\upsilon_{ks}(\boldsymbol{r},t)$ is:

$$\upsilon_{ks}[\rho(\boldsymbol{r},t)] = \upsilon_{ext}[\rho(\boldsymbol{r},t);\Psi_0] + \int \frac{\rho(\boldsymbol{r},t)'}{|\boldsymbol{r}-\boldsymbol{r}'|}d\boldsymbol{r}' + \upsilon_{xc}[\rho(\boldsymbol{r},t);\Psi_0] \tag{2.30}$$

Where $\upsilon_{ext}[\rho(\boldsymbol{r},t);\Psi_0]$ is the time-dependent external field at time t with an initial state Ψ_0, and $\upsilon_{xc}[\rho(\boldsymbol{r},t);\Psi_0]$ us the time-dependent exchange-correlation potential. Most approximations state that the dependence of υ_{xc} is only on the instantaneous ρ, allowing to use the same functional form that is used for the ground state computations. This Ansatz is not really justified by *a priori* arguments, but it is the only simple way to carry on the calculations and provides accurate results, once implemented.

2.2 Modelling the Dielectric Function

The main sources for the writing of this paragraph are: [44–53]

2.2.1 Drude-Lorentz model

The description of the interaction between metals and the electromagnetic field can be achieved employing a framework based almost totally on the classical electrodynamics provided by the Maxwell's equations. This proves to be true also for metallic nano-structures much smaller than the wavelength of the applied electromagnetic field, as long as the spacing between electron energy levels is smaller than the thermal excitation k_BT. Even though for the low frequency regime metals can often be approximated to perfect conductors, therefore implying an infinite conductivity, at a frequency regime approaching the visible spectrum of light, they must be described adopting a dielectric representation, thus including dissipation, absorption and propagation of the electromagnetic field, forcing the introduction of a frequency dependent complex dielectric function $\varepsilon(\omega)$ to solve the Maxwell equations for the system at hand. Usually, this is achieved through a depiction called *plasma model*, in which a rigid structure of positive ions confines a gas of free electrons. This neglects the lattice potential, along with the electron-electron interaction. Upon the application of an electromagnetic field, the electrons start to oscillate following the driving field with a dampening due to the collisions with the ion lattice, taking place with a

frequency $\gamma = 1/\tau$, where τ represents the relaxation time of the electron gas. The motion for a single electron, along the vector $\boldsymbol{x}$, then becomes:

$$m\boldsymbol{x}'' + m\gamma\boldsymbol{x}' = -e\boldsymbol{E} \tag{2.31}$$

Where m and e are the mass and the charge of the electron respectively. The driving field oscillation is expected to be harmonic (which is expressed as $\boldsymbol{E}(t) = \boldsymbol{E_0}e^{-i\omega t}$), therefore one possible solution of the equation becomes:

$$\boldsymbol{x}(t) = \frac{e}{m(\omega^2 + i\gamma\omega)}\boldsymbol{E} \tag{2.32}$$

Conveying the polarization as $\boldsymbol{P} = -ne\boldsymbol{x}$, it gives:

$$\boldsymbol{P} = -\frac{ne^2}{m(\omega^2 + i\gamma\omega)}\boldsymbol{E} \tag{2.33}$$

The relation that links polarization and electric field is $\boldsymbol{D} = \varepsilon_0\boldsymbol{E} + \boldsymbol{P}$, therefore:

$$\boldsymbol{D} = \varepsilon_0\left(1 - \frac{\omega_p^2}{\omega^2 + i\gamma\omega}\right)\boldsymbol{E} \tag{2.34}$$

Where $\omega_p^2 = \frac{ne^2}{\varepsilon_0 m}$ is called *plasma frequency* and is a value characteristic for each material, as it is the dampening frequency γ.

From which it can be extracted a relation that describes the frequency dependence of the complex dielectric function $\varepsilon(\omega)$:

$$\varepsilon(\omega) = 1 - \frac{\omega_p^2}{\omega^2 + i\gamma\omega} \tag{2.35}$$

The real and imaginary parts of this dielectric function are given by:

$$\mathfrak{Re}\{\varepsilon(\omega)\} = 1 - \frac{\omega_p^2\tau^2}{1 + \omega^2\tau^2} \tag{2.36}$$

$$\mathfrak{Im}\{\varepsilon(\omega)\} = \frac{\omega_p^2\tau}{\omega(1 + \omega^2\tau^2)} \tag{2.37}$$

This is the Drude-Lorentz model for the dielectric function of a metal.
Since for many metals $\omega_p \gg \gamma$, then at the plasma frequency the dielectric function changes sign, the real part goes to zero, while the imaginary part reaches a maximum. At this particular frequency the dispersive waves created by the oscillation of the electron density within the rigid structure of the positive ions in the plasma model display a resonant behaviour, they can be quantized and the resulting quasi particle is called *plasmon*.

2.2.2 When Drude-Lorentz fails: empirical models for the dielectric constant

Gold, conversely from many other metals, does not follow the Drude-Lorentz model for the modelization of its dielectric constant. This is due to the presence of two interband transitions at 470 nm and 330 nm, that play an important role in determining the colour and many other optical properties of this valuable metal. The transitions have asymmetric band shapes and thus do not allow for simple representations with additional Lorentz oscillators to be taken into account. In literature works many attempts have been done in order to analytically describe the Gold dielectric function [51, 53] using many different approaches. We chose in particular the approach in [51] of its ease of implementation and small number of parameters required. The dielectric function of Gold reads as:

$$\varepsilon_{Au}(\omega) = \varepsilon_\infty - \frac{\omega_p^2}{\omega^2 + i\Gamma\omega} + G_1(\omega) + G_2(\omega) \tag{2.38}$$

Where the first and second term are the standard Drude model, with a high frequency limit ε_∞, a plasma frequency ω_p, and a damping term Γ. $G_1(\omega)$ and $G_2(\omega)$ are the contributions from the interband transitions, that are expressed as:

$$G_i(\omega) = C_i\left[e^{i\phi_i}(\omega_i - \omega - i\Gamma_i)^{\mu_i} + e^{-i\phi_i}(\omega_i - \omega - i\Gamma_i)^{\mu_i}\right] \tag{2.39}$$

Where C_i is the amplitude, ϕ_i the phase, ω_i the energy of the interband transition, Γ_i the broadening, and μ_i the order of the pole. These values were fitted over the experimental results in order to provide the best representation possible, and are listed in ref.[52].

2.3 Electromagnetic scattering by metal particles

The source for the writing of this section are: [50, 54–56]. When a particle is hit by an electromagnetic wave the light is absorbed and scattered by the particle, and the general behaviour of this process is determined by the shape, the size and the material of the particle, as well as the characteristics of the electromagnetic wave, such as the wavelength and the polarization. Dividing the time dependent fields into two parts, inside and outside the particle, must satisfy the Maxwell equations within the boundary conditions imposed by the separation of space introduced by the presence of the particle. These boundary conditions require that the tangential components of the electric and magnetic fields are continuous across the boundary separating the two media with different properties. This leads to the construction of an amplitude scattering matrix that represent the relation between incident and scattered fields, which can be used, along with Stokes parameters of the light scattered by a particle, to determine what is called the *scattering matrix*, which is the Mueller matrix for scattering by a single particle. All of this mathematical tools can be used to determine the extinction cross section C_{ext}.

Considering a single arbitrary particle embedded in a nonabsorbing medium, when this is hit by a plane wave, the rate of electromagnetic energy that crosses

an imaginary sphere around the particle, with radius r and surface A, can be written as:

$$W_{abs} = -\int_A \boldsymbol{S} \cdot \hat{\boldsymbol{e}}_r dA \tag{2.40}$$

Where $\hat{\boldsymbol{e}}_r$ is the direction where the scattering intensity is evaluated. If $W_{abs} > 0$ then the particle absorbs energy. Defining W_{sca} as the rate at which the energy is scattered across the surface, the extinction rate W_{ext} can be expressed as the sum of these two terms: $W_{ext} = W_{sca} + W_{abs}$. With some massage of the terms, using the tools named above, the extinction energy rate can be written as:

$$\begin{aligned} W_{ext} = & \frac{-k}{2\omega\mu}|E|^2 \mathfrak{Re}\left\{ \frac{e^{-ikr}}{ikr} \int_A e^{-ikz} \hat{\boldsymbol{e}}_x \cdot \boldsymbol{X}^* dA \right. \\ & - \frac{e^{-ikr}}{ikr} \int_A e^{-ikz} \cos\theta \hat{\boldsymbol{e}}_x \cdot \boldsymbol{X} dA \\ & \left. \frac{e^{-ikr}}{ikr} \int_A e^{-ikz} \sin\theta \cos\phi \hat{\boldsymbol{e}}_x \cdot \boldsymbol{X} dA \right\} \end{aligned} \tag{2.41}$$

Where ω is the field frequency, μ the medium permeability, k the imaginary part of the refractive index, $\hat{e}_x$ an orthonormal basis vector perpendicular to the propagation direction and parallel to the polarization, θ and ϕ the scattering and polarization angles, and $\boldsymbol{X}$ the vector scattering amplitude, which is related to the aforementioned amplitude scattering matrix.

Considering an incident wave with irradiance I_i, the ratio between W_{ext} and I_i is the *extinction cross section* C_{ext}, which may be written as the sum of the absorption and scattering cross sections:

$$C_{ext} = C_{abs} + C_{sca} \tag{2.42}$$

Other useful quantities can be defined from the cross sections: the extinction, scattering and absorption efficiencies, using the area of the particle projected onto the plane perpendicular to the incident beam G.

$$Q_{ext} = \frac{C_{ext}}{G} \quad , \quad Q_{abs} = \frac{C_{abs}}{G} \quad , \quad Q_{sca} = \frac{C_{sca}}{G}$$

For a particular case, when the particle is spherical, the absorption and scattering efficiencies can be written as:

$$Q_{abs} = 4x \cdot \mathfrak{Im}\left\{ \frac{\varepsilon_m(\omega) - \varepsilon_s}{\varepsilon_m(\omega) + 2\varepsilon_s} \right\} \cdot \left[1 + \frac{4}{3} x^3 \cdot \mathfrak{Im}\left\{ \frac{\varepsilon_m(\omega) - \varepsilon_s}{\varepsilon_m(\omega) + 2\varepsilon_s} \right\} \right] \tag{2.43}$$

$$Q_{sca} = \frac{8}{3} x^4 \left| \frac{\varepsilon_m(\omega) - \varepsilon_s}{\varepsilon_m(\omega) + 2\varepsilon_s} \right|^2 \tag{2.44}$$

With $x = \frac{2\pi Na}{\lambda}$ being the size parameter defined with a the radius of the particle, N the refractive index of the particle, and λ the exciting beam wavelength. It is noteworthy that, of the two terms inside the square brackets in the expression of Q_{abs},

one shows a dependence from the size of the particle, while the other is independent of the size. When the size of the particle becomes much lower than the exciting wavelength, $a \ll \lambda$, then the term containing $x^3 \ll 1$, allowing to drop all the size dependent term inside the brackets, and simplifying the expression for the absorption efficiency, that now becomes:

$$Q_{abs} = 4x \cdot \Im\mathfrak{m}\left\{\frac{\varepsilon_m(\omega) - \varepsilon_s}{\varepsilon_m(\omega) + 2\varepsilon_s}\right\} \tag{2.45}$$

This result brings to what is called *quasistatic approximation*, and is effective for particles with a size much smaller than the exciting wavelength. As long as 2.45 is a good approximation, the absorption cross section of a sphere can be written as:

$$C_{abs} = \pi a^2 Q_{abs} \tag{2.46}$$

Which is proportional to the volume of the particle. The scattering cross section can be written as:

$$C_{sca} = \frac{k^4}{6\pi}|\alpha| = \pi a^2 \frac{8}{3} x^4 \left|\frac{\varepsilon_m(\omega) - \varepsilon_s}{\varepsilon_m(\omega) + 2\varepsilon_s}\right|^2 \tag{2.47}$$

Where α is the polarizability of a sphere, written as:

$$\alpha = 4\pi a^3 \frac{\varepsilon_m(\omega) - \varepsilon_s}{\varepsilon_m(\omega) + 2\varepsilon_s} \tag{2.48}$$

2.3.1 Local Surface Plasmon Resonance

The source for the writing of this section are: [48, 49]. As presented in section 2.2.1, we know that the dielectric behaviours of the electrons in a metallic system can be represented with a plasma model. At the dielectric interface of conductive bulk metal with an external dielectric, an oscillating electromagnetic field can couple with the electron plasma, creating propagating, and dispersive, waves, that are called Surface Plasmon Polaritons. When the metallic system becomes small enough, with respect to the oscillating field wavelength, the curvature of the object starts to apply a restoring force on the driven electrons, opening to the surge of a resonant behaviour within the conduction electrons of the metallic structure. The arising resonance behaves like a proper non propagating excitation confined within the boundaries of the small metal particle. This resonance is called Localized Surface Plasmon Resonance (LSPR), and is a direct consequence of the excitation of the electron plasma by an incident electromagnetic wave in small metallic systems. This behaviour can be very well described by the means of electrodynamics, since the plasmonic behaviour depends mostly on the polarizability of the system, and the nature of α is well depicted within the Maxwell equations.

A very peculiar property of LSPR is the ability to enhance the fluorescence of neighbouring emitters, due to the heightened electromagnetic fields near the metallic surface.

2.4 Maxwell-Garnett Effective Model

In some complex cases, computing the macroscopic properties of composite systems, starting from the microscopic features, can be a very hard task. This is why effective models have been developed to simply approach the macroscopic properties starting from a few microscopic ones and extending them to a homogeneous, effective system that epitomizes their properties. The source for this paragraph is: [50, 57]. The Clausius-Mossotti relation can be written as:

$$\frac{\varepsilon - 1}{\varepsilon + 2} = \frac{4\pi}{3} \sum_j N_j \alpha_j \tag{2.49}$$

This relates a macroscopic property, the dielectric constant ε to a microscopic one, the molecular polarizability α_j, through the quantity N_j that refers to the number of molecules per unit volume. Maxwell-Garnett theory is the extension of this model to arbitrary composite systems, and it is developed supposing a system composed of a matrix with spherical inclusions, and exploiting simple models for evaluating the polarizability α. For a spherical molecule with dielectric constant ε_i and radius a, the polarizability is:

$$\alpha = \left(\frac{\varepsilon_i - 1}{\varepsilon_i + 2} \right) a^3 \tag{2.50}$$

Substituting eq. 2.50 into eq. 2.49, it follows:

$$\left(\frac{\varepsilon - 1}{\varepsilon + 2} \right) = \delta_i \left(\frac{\varepsilon_i - 1}{\varepsilon_i + 2} \right) \tag{2.51}$$

Where δ_i is the volume fraction of inclusions. For a host matrix with dielectric constant ε_m the relation becomes:

$$\left(\frac{\varepsilon_{\text{eff}} - \varepsilon_m}{\varepsilon_{\text{eff}} + 2\varepsilon_m} \right) = \delta_i \left(\frac{\varepsilon_i - \varepsilon_m}{\varepsilon_i + 2\varepsilon_m} \right) \tag{2.52}$$

Where ε_{eff} is the effective medium dielectric constant, which can be computed with the following relation:

$$\varepsilon_{\text{eff}} = \varepsilon_m \frac{2\delta_i(\varepsilon_i - \varepsilon_m) + \varepsilon_i + 2\varepsilon_m}{2\varepsilon_m + \varepsilon_i - \delta_i(\varepsilon_i - \varepsilon_m)} \tag{2.53}$$

2.5 Polarizable Continuum Model

This section is writte using the following refs: [40, 58, 59]. Solvation Gibbs' free energy is defined as:

$$\Delta G_s = W_{ms} + \Delta G_m \tag{2.54}$$

Where W_{ms} is the static work necessary to bring the molecule inside the solvent at a fixed geometry, and ΔG_m is the free energy spent by the molecule to modify its

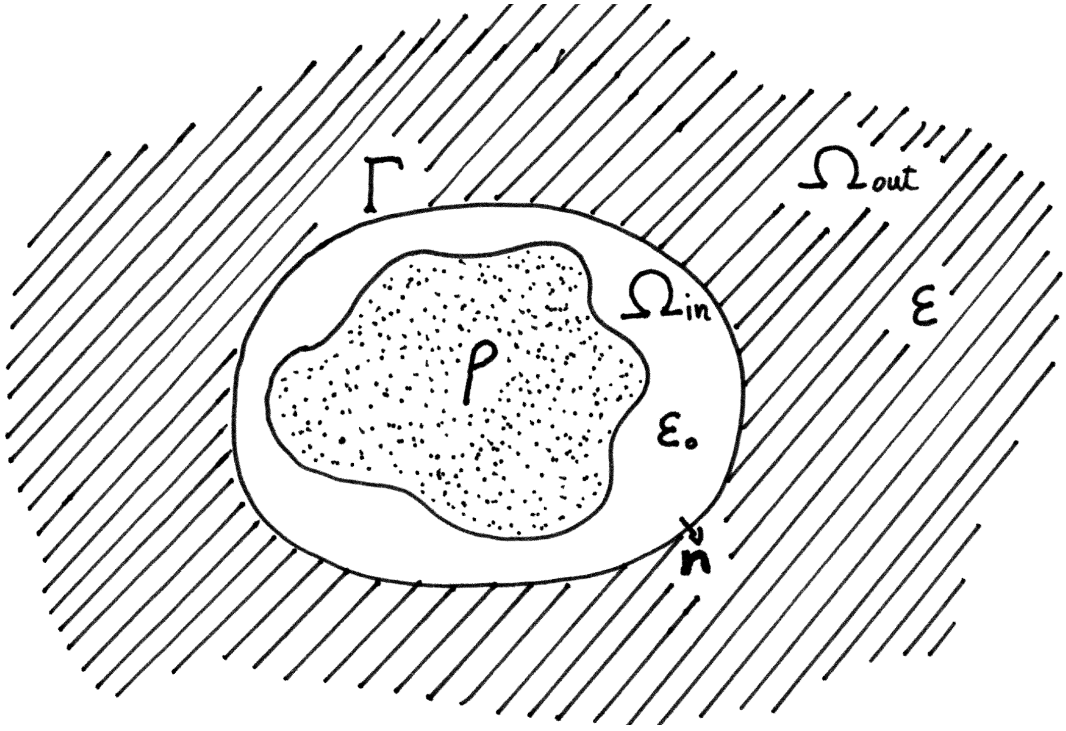

FIGURE 2.1: A schematic representation of the model

geometry to adapt to the change of environment with respect to the vacuum. PCM works whithin the premises of W_{ms}, which can be expanded as:

$$W_{ms} = G_{cav} + G_{es} + G_{VdW} \tag{2.55}$$

Where G_{cav}, G_{es}, and G_{VdW} are the cavitation energy, which is the work spent to dig into the solvent the space necessary to accommodate the solute, the electrostatic interaction energy and the Van der Waals term. PCM is used to compute only the electrostatic part of W_{ms}.

The electrostatic work can be expressed as:

$$W_{es} = \frac{1}{2}\int d^3\boldsymbol{r}\,\rho(\boldsymbol{r})V_r(\boldsymbol{r}) \tag{2.56}$$

Being $\rho(\boldsymbol{r})$ the molecular charge density, and $V_r(\boldsymbol{r})$ is the potential coming from the solvent. This takes into consideration only the electrostatic interaction between solvent and solute, any other term, like the magnetic interaction, is not included. If the system is non-magnetic, the Maxwell equations become:

$$\begin{cases} \boldsymbol{\nabla}\cdot\boldsymbol{D} = 4\pi\rho \\ \boldsymbol{\nabla}\times\boldsymbol{E} = 0 \end{cases} \tag{2.57}$$

Since a cavity is needed to host the solute inside the solvent, the volume can be divided in two zones Ω_{in} and Ω_{out}, with the former contained inside the latter, separated by an arbitrary continuous three-dimensional closed surface called Γ. The

general solution is then split in two parts: the integral over the space and the integral over the surface Γ. The task now is to compute the potential associated to the charge density ρ, *via* the Poisson equation, with the constraint that the potential goes to zero at infinite distance. While the general Poisson equation occurs with the following appearance:

$$-\boldsymbol{\nabla}\left[\varepsilon\nabla V(\boldsymbol{r})\right] = 4\pi\rho(\boldsymbol{r}) \tag{2.58}$$

It can be simplified in two different forms inside and outside the boundary surface, which are:

$$\begin{cases} -\boldsymbol{\nabla}^2 V(\boldsymbol{r}) = 4\pi\rho(\boldsymbol{r}) & \text{if } \boldsymbol{r} \in \Omega_{in} \\ -\varepsilon\boldsymbol{\nabla}^2 V(\boldsymbol{r}) = 0 & \text{if } \boldsymbol{r} \in \Omega_{out} \end{cases} \tag{2.59}$$

With the total potential $V(\boldsymbol{r})$ being the sum of the electrostatic potential $V_M(\boldsymbol{r})$ generated by ρ, and the reaction potential $V_R(\boldsymbol{r})$

$$V(\boldsymbol{r}) = V_M(\boldsymbol{r}) + V_R(\boldsymbol{r}) \tag{2.60}$$

Some conditions must be met for the system to be physical, notably the boundary conditions for $\boldsymbol{r} \to \infty$:

$$\begin{cases} \lim\limits_{\boldsymbol{r}\to\infty} rV(\boldsymbol{r}) = \alpha \\ \lim\limits_{\boldsymbol{r}\to\infty} r^2 V(\boldsymbol{r}) = \beta \end{cases} \tag{2.61}$$

With α and β being fine values, forcing the potential not to diverge, and the jump conditions around the surface Γ, which imposes the continuity of the potential across the surface:

$$\begin{cases} [V] = V_{in} - V_{out} = 0 & \text{on } \Gamma \\ [\partial V] = \left.\frac{\partial V}{\partial \boldsymbol{n}}\right|_{in} - \varepsilon \left.\frac{\partial V}{\partial \boldsymbol{n}}\right|_{out} & \text{on } \Gamma \end{cases} \tag{2.62}$$

Where $\boldsymbol{n}$ is a versor normal to the surface Γ, allowing for a directional derivative over the surface. Also the relative dielectric permittivity becomes a function of the space:

$$\varepsilon(\boldsymbol{r}) = \varepsilon_0\gamma_{in}(\boldsymbol{r}) + \varepsilon\gamma_{out}(\boldsymbol{r}) \tag{2.63}$$

Chapter 3

Simulation of Gold Nanoclusters *via* plane-waves DFT

3.1 Introduction

Shrinking the size of Gold particles up to the nanoscale originates behaviours diverging from the bulk properties. While the size and shape tunable plasmon resonance is a characteristic of the sub-wavelength sized nanoparticles, when the size scale of Fermi wavelength is reached, the nanoparticles, which now are composed of a few atoms, start exhibiting quantized electronic transitions, rather than diffuse plasmon resonances [60]. From this in mind, it is evident the necessity to approach the problem within the quantum mechanical world, being DFT probably the most widely used method in this regard [61–70]. These works concentrated, *in primis*, to find and compute the equilibrium geometries for nanoclusters of increasing number of atoms, from 2 to N, and amongst these finding the most stable and more probable structures at this size scale. The main result is that, unlike other metal nanoclusters, which tend to acquire a three-dimensional structure quite early in the climb of atom numbers, being Ag_n and Cu_n [63] already three dimensional for N=7, in the case of Gold DFT calculations show that the equilibrium structure in vacuo is planar up to N=14 [71]. The main reason for this is the relativistic enhancement of *sd* hybridization [63], and *d*-*d* interaction in Gold, with respect to Ag and Cu. The $nd_{10}\,(n+1)\,s_1$ electronic structure allows for a simplified treatment of Ag and Cu as s_1 electron systems, with some perturbation by the underlying *d* shell. In the case of Gold, this approach is definitely oversimplified, for the relativistic effects that arise in the high speed electrons that populate the *5d* shell, leading to the necessity of considering both the *5d* and *6s* electrons in the calculations. The main goal of this chapter is to reproduce the behaviours of these Gold nanoclusters, and investigate the feasibility of using Gold nanoclusters of sufficient size as models for the metal counterpart in hybrid nanoparticles. One potential for modelling the metallic counterpart in hybrid nanoparticles using explicit Gold is the ability to include charge transfer behaviours into the system. This is excluded when employing continuum models that use polarization to model the plasmon resonance, since they cannot take into account changes in the number of electrons, as the point charges that are used in PCM model (see Chapter 2.5)

3.2 Computational details

All simulations have been performed using the code package QuantumEspresso[72]. The DFT calculations have been performed using plane-waves based wavefunctions, a GGA based exchange correlation functional in the terms of PBE, and a non-relativistic PAW pseudopotential with 11 valence electrons. The DFT computations were performed at the Γ point with a box that allowed at least 25 Bohr of vacuum in any direction, in order to avoid self-interactions due to the periodic boundary conditions. The kinetic energy cutoff was 40 Rydberg, and the charge density cutoff was 300 Rydberg. The Marzari-Vanderbilt smearing [73] was used at 0.01 Ry. In the case of odd number of electrons, polarization was allowed unrestricting the spin orientation, but in the case of even number of electron the polarization was restricted to zero forcing the symmetry in spin distribution due to issues in converging the wavefunction during the scf process. No other symmetry was implemented. The geometries have been generated taking the topology of the clusters from literature, then optimized with classical molecular dynamics (conjugate gradient) to find a geometry closer to the actual minimum, and then a full-quantum relaxation was performed in order to find the equilibrium geometry. TDDFT was performed using Liouville-Lanczos approach in Quantum-Espresso [74–76].

3.3 Results and discussion

Binding energy is defined as: $E_B(n) = nE_1 - E_n$, where E_1 is the energy of a single Gold atom, and E_n is the energy of the n-atom nanocluster, while the second order binding energy difference is $\Delta^2 E(n) = E_B(n+1) + (n-1) - 2E_B(n)$. Equilibrium geometries proved to be planar for Au_n up to N=13, showing good agreement with previous calculations [71]. In fig. 3.1 are listed the most stable geometries found for the Gold clusters between 3 and 13 atoms, and with 20 atoms. The order is set in decreasing stability, within clusters with the same number of atoms, so the nomenclature will be of the kind N.X, where N is the number of atoms present, and X another number that follows the stability order. The most stable geometry for Au_3 is the equilateral triangle (3.1), with 60° angles and a bond distance of 2.67 Å, and a binding energy of 1.186 eV/atom. The linear structure (3.2) has a lower binding energy at 1.166 eV/atom. The most stable Au_4 structure is the planar parallelogram (4.1), with a binding energy of 1.525 eV/atom, while the tetrahedral structure has a lower stability at 1.185 eV/atom. For all the clusters from Au_5 to Au_{13} the most stable geometries proved to be the close flat configurations, with Au_5 shaped as a trapezoid (5.1), Au_6 as an equilateral triangle with shortened tips (6.1); for Au_7 the most stable geometry is mostly similar to the triangular shape of Au_6 with one added atom at one of the edges (7.1), while the hexagonal geometry shows a slightly lower binding energy (7.2). The most stable geometries from 9 to 13 atoms are based on the same basic structure (9.1 or 10.1), with an additional atom every time that completes the closed geometry. For the Au_{20} nanocluster, the tetrahedron is the most stable geometry (20.1). In fig. 3.2 are presented the binding energies of the inquired geometries. In all the cases considered, up to Au_{13}, the most stable geometry proved to be planar, as expected from the literature. The binding energy increases dramatically adding the first 4 atoms from Au_3, it can also be noticed that even numbered nanoclusters

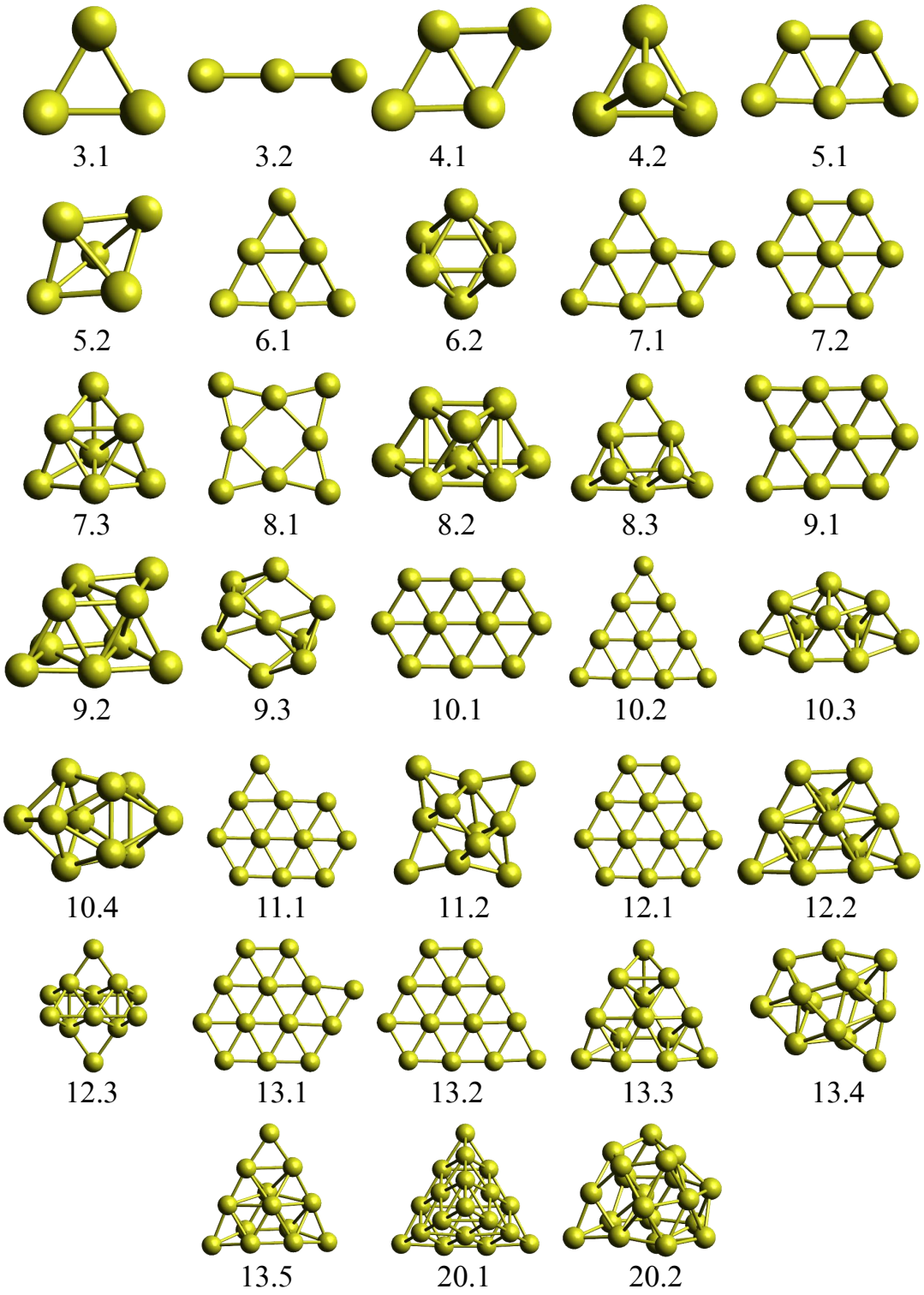

FIGURE 3.1: Schematic representation of the Gold nanoclusters

are more stable thane the neighbouring odd numbered ones. As is shown in fig. 3.3, the behaviour is consistent with literature [71], following the very same trend with an offset of additional 0.09 eV/atom on average. The offset is probably due to the different implementation of DFT used. In fig. 3.4 the second order binding energy difference shows clearly how the even numbered Gold clusters are more stable than the odd numbered ones. In fig. 3.5 are presented the HOMO-LUMO gaps at different numbers of atoms. Only the stable even numbered clusters have been plotted, since the unrestricted calculations do not give a proper HOMO-LUMO gap. For some stable geometries it was possible to compute also the TDDFT spectra, depicted in fig. 3.6. The HOMO-LUMO gaps, which are finite, and the optical spectra, which show no absorption for energies lower than a few eV, show that, for nanoclusters up to this size, the behaviour of the electronic density is comparable to molecular systems rather than plasmonic materials.

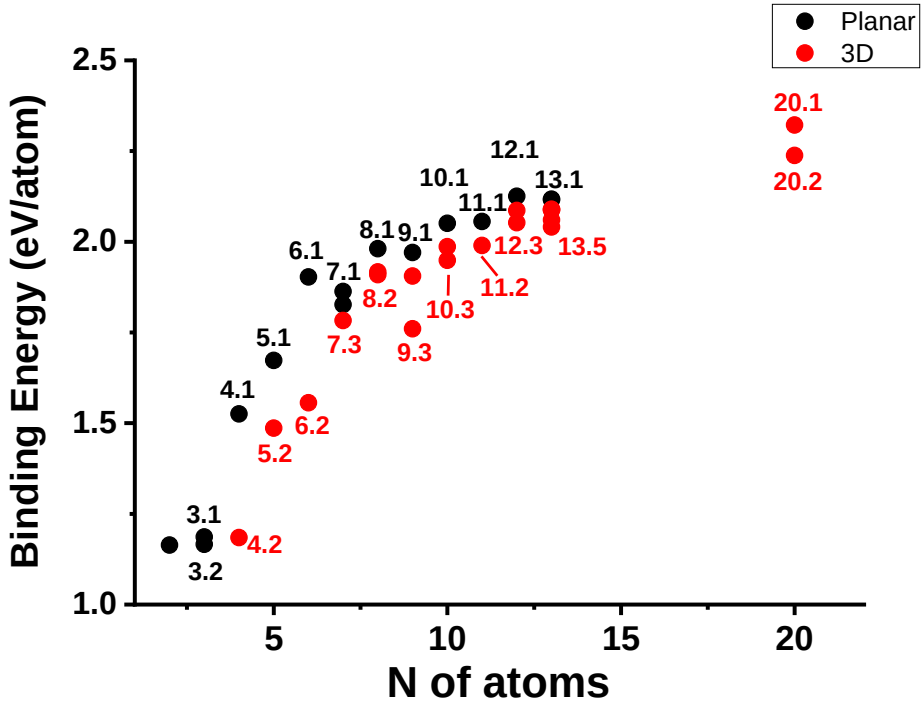

FIGURE 3.2: Binding energies of the clusters computed. The geometries they represent are pointed by the labels. In black are the planar geometries and in red the three-dimensional ones.

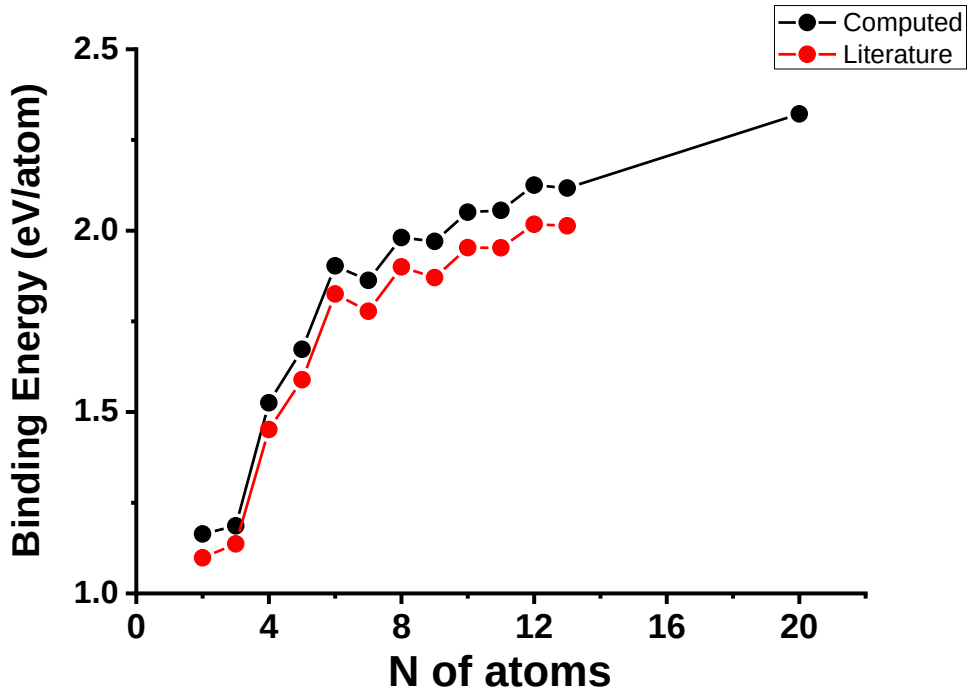

FIGURE 3.3: Binding energy of the most stable structures by number of atoms, compared to literature values from ref. [71]. The average offset is 0.09 eV

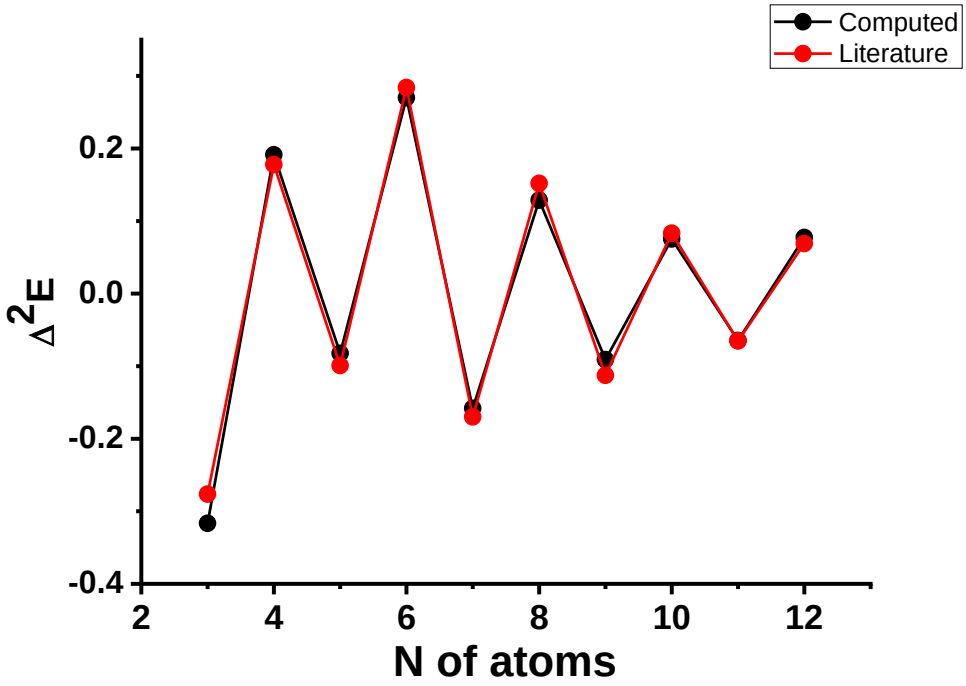

FIGURE 3.4: Second order binding energy difference ($\Delta^2 E$) against the number of atoms, compared to literature [71].

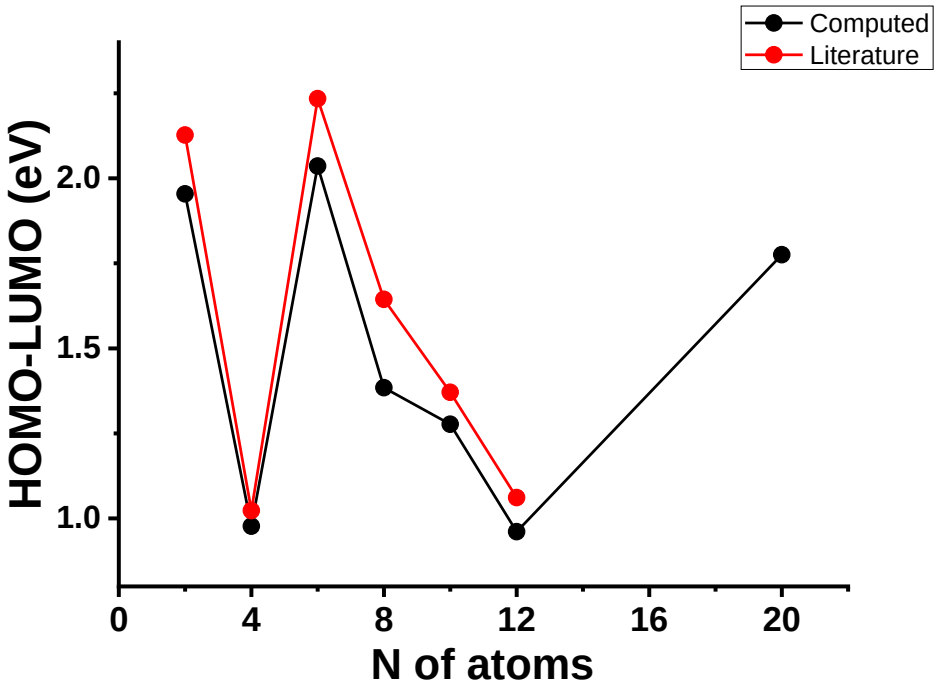

FIGURE 3.5: HOMO-LUMO gaps compared to literature [71]

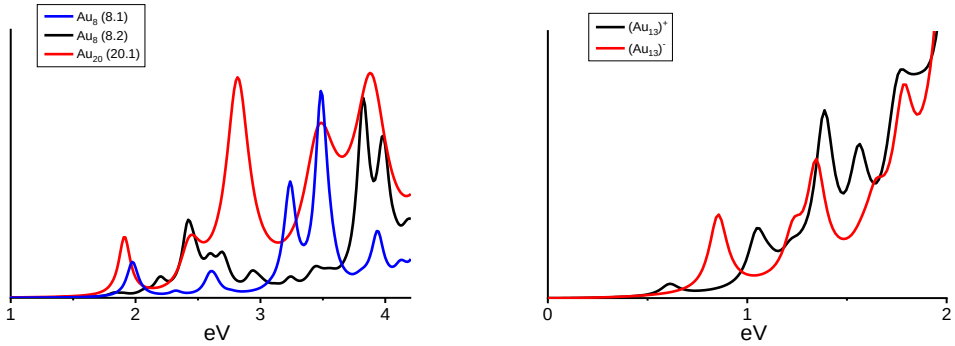

FIGURE 3.6: Computed spectra of some clusters, on the right the spectra of positive and negative ions of Au_{13}

3.4 Conclusions

The results showed that the nanoclusters of Gold keep the closed-flat configuration as the most stable one up to 13 atoms clusters. Due to great difficulties in converging the wavefunctions during the scf process in DFT calculations for many configurations, and due to the lengthy and expensive computations that are needed to process Gold nanoclusters with plane-waves DFT, the conclusion is that it is not worth the amount of effort needed. The size of clusters available for quantum mechanics simulations is not big enough to show a strong arise in plasmonic behaviours, and thus would not make for an effective approximation in computing charge transfer properties, which are excluded by default when treating hybrid nanoparticles with classical continuum models, since structurally they cannot account for exchanges of electrons.

Chapter 4

Classical Electro-Magnetic simulations of Gold Nanoparticles

This chapter is based on a paper submitted to the Journal of Chemical Theory and Computation.

4.1 Introduction

Hybrid organic-inorganic Nanoparticles (HNPs) are very interesting and widely studied materials, for their versatile employments in many different technological or medical applications. These materials can be used to manufacture nanoscaled devices with specific photonic, magnetic, or reactivity properties, that allow numerous and varied functions such as bio-imaging, photo-catalysis, optics, solar cells and biotechnology [7, 77]. When the inorganic portion is metallic, the main feature characterizing these nanomaterials is the interaction between the optically induced collective excitations of free charges confined in the highly conductive premises of the metallic portion, called Localized Surface Plasmon Resonance (LSPR) [50], with the excitons of the organic semiconductive counterpart in the hybrid system [78]. Another relevant property of plasmonic nanosystems is electric field localization: upon resonant excitation, LSPR can exceed the diffraction limit and collect light into a sub-wavelength region. This greatly enhances the optical electric field, maximising the effects of such field over optically active molecules adjacent (or adsorbed) to the metal surface [79–81]. In many cases the LSPR operates quenching or enhancing the photo-physical properties of the nearby molecular systems, resulting, to make a few examples, in increased luminosity or absorbance, or in preserving the photochemical stability of the chromophores opening non-reactive deactivation processes of the excited state of chromophore [16, 82], allowing for intriguing synergistic optical properties and very versatile technological applications.

Metal nanoparticles, noble metals in particular, allow for a wide variety of spectral tuning of the LSPR, varying their size, shape and dielectric environment [83–90]. Combining this with the vast assortment of possible chromophores opens up to a versatile family of luminescent organic-inorganic materials.

Finding a proper computational procedure to model these systems can bring to the ability to drive the design of new experimental systems starting from the properties predicted by the theoretical models, which likewise can be used to rationalise experimental results.

However, computing in details the physical-chemical properties of these systems proves to be a challenge. While the nature of the organic component of the HNPs requires a full quantum chemical treatment in order to be predictive and properly interpret properties at this length scale, the size of the inorganic component renders this treatment computationally too expensive to be assessed with an homogeneous technique. For this reason hybrid models have been developed combining a QM level treatment and a classical electromagnetism approach, respectively, for molecules and the inorganic nano-structures upon which they are adsorbed [91]. In particular, in the model developed in refs. [92–96], the inorganic component, usually a metal, is considered as a continuous body, characterized by its own frequency dependent dielectric function (Polarizable Continuum Model, PCM), while excitation energies due to the energy transfer from the molecule to the metal is evaluated exploiting Time Dependent Density Functional Theory (TDDFT).

The basic step to implement such approaches is an assessment of how well the PCM framework describe, with its own limitations, the optical properties of the metallic counterpart of the hybrid system. The theoretical treatment of LSPR in non-functionalised noble metal nanoparticles has long been established [49, 50], with methods that generally stem from numerical solutions of Maxwell equations over a modelisation of the dielectric environment of the metallic object. These methods have been proved to be very effective in the description of LSPR spectra and near-field enhancements. These simulations have been used in many cases to interpret experimental observations [47] or design new materials for technological applications [97].

Among the broad assortment of possible combinations, in this work we took into consideration Gold nanoparticles with bipyramidal shape (GNB). In general, sharp and edgy structures present high sensitivity to local changes in the dielectric environment [9, 98–101] and in particular bipyramidal shaped NPs not only allow to fine tune the plasmon resonance energy [2, 13, 14, 16, 102–104], but present a narrower plasmon band with respect to other nanoparticles with non-spherical shapes, like rods or dog-bone [84, 105–107]. Moreover, the presence of two tips enhance the effects of the local electric field generated by the metal nanoparticle which has important effects over the near-field enhancement of the organic counterpart's excitons in the hybrid nanoparticles. Notably, in recent literature were reported high yield syntheses of Gold Nanoparticles with such shapes, in various sizes and aspect ratios in mono-dispersed samples [2, 3, 9, 13, 14, 98, 99, 102, 103, 108, 109].

Another reason for this choice is that some of the NPs taken into account still lack a theoretical modelisation [3] or they present some non-explained deviations between experiment and theory [2]. In this work we focused on providing a comprehensive theoretical investigation of these GNBs to link the absorption maxima to their morphological characteristics, even when a distribution of GNBs (as synthesised GNBs in a solution usually appear) is taken into account instead of a single GNB. We also inquired how the standard deviation of the distribution of geometrical parameters affect the absorption of the set of GNB with respect to the single GNB. We also checked if it is possible to distinguish the effects of using different shapes of the GNBs in the calculations, for example discerning between various kind of tips or possible base geometries.

Therefore we probed the capabilities of full Electro-Magnetic (EM) scattering

approach in simulating the cross section of the aforementioned bipyramidal class of Gold NPs. The spectra of Gold Nanbipyramids (GNBs) were computed exploiting the principles of classical electrodynamics scattering theory. This theory gives analytical results only for spherical and ellipsoidal shaped objects, therefore a numerical approach is needed. We described the metal response to the electric fields using the widespread assumption that the metal behaves as a perfect conductor for static fields and as a dielectric for time dependent fields. The solvent was described as a continuum dielectric which occupies all the space free from the metal specimen. The equation that describes EM absorption for spheres is:

$$Q_{abs} = 4x \cdot \Im\mathfrak{m}\left\{\frac{\varepsilon_m(\omega)-\varepsilon_s}{\varepsilon_m(\omega)+2\varepsilon_s}\right\} \cdot \left[1+\frac{4}{3}x^3 \cdot \Im\mathfrak{m}\left\{\frac{\varepsilon_m(\omega)-\varepsilon_s}{\varepsilon_m(\omega)+2\varepsilon_s}\right\}\right] \tag{4.1}$$

With $\varepsilon_m(\omega)$ being the complex, frequency dependent dielectric function of the metal, ε_s the dielectric constant of the surrounding solvent, and x a size parameter $x \propto \frac{a}{\lambda}$, where a is the radius of the spherical NP and λ is the wavelength of the incident electromagnetic radiation. Factoring out the overall linear dependence on the object's size, the relation is left with two terms: one which depends on the NP's size and one which is size-independent. If the size of the NP is comparable to the size of the incident wave, then the full EM equation is needed. If the size of the NP is much smaller than the incident wave, the full EM (i.e. Maxwell) equations reduce to just a time dependent Poisson problem, and the size-dependent term goes to zero very fast, to the third power of x and can be neglected. This approximation is called *quasi-static approximation* (QSA) or *dipole approximation* and it allows straightforwardly to couple organic chromophores described by first principle approaches with the metal NP [91]. The absorption becomes then:

$$Q_{abs} = 4x \cdot \Im\mathfrak{m}\left\{\frac{\varepsilon_m(\omega)-\varepsilon_s}{\varepsilon_m(\omega)+2\varepsilon_s}\right\} \tag{4.2}$$

Mie scattering equations are analytical only for spheres and ellipsoids, but in order to compute EM scattering properties for arbitrary shapes a numerical approach is needed. For instance, in ref. [2] Discrete Dipole Approximation (DDA) [46] approach was applied to bipyramidal nanoparticles. DDA consists in solving the EM scattering equations for an object, where the three-dimensional solid particle is replaced by a finite array of polirazable point dipoles, with the spacing between the dipoles small compared to the wavelength of the incoming light. Each of these dipoles has an oscillating polarization in response to both an incident plane wave and the electric fields due to all of the other dipoles in the array. This method allows the employment of arbitrary shapes, instead of being restricted to a small number of regular shapes like spheres, spheroids and infinite cylinders, along with the opportunity to introduce anisotropies inside the particle. However, this approach has some limitations in terms of affordability with respect to the number of dipoles employed, which does not allow for a very detailed representation of complex shapes. An alternative approach would be to solve numerically the EM scattering equations exploiting the Boundary Element Method (BEM). BEM, in general, is a numerical computational method of solving linear partial differential equations which were reformulated as

integral equations. Rather than solving a numerical problem of a set of partial differential equations defined throughout the whole space, BEM maps the problem into an integral equation defined over the boundary of the system. In practice, a three dimensional problem (e.g. DDA) is mapped onto a two dimensional surface, thus demanding a computational cost that scales with the size of the surface instead of the volume, also allowing for a greater control of the details of the chosen object. In this particular case, the solid particle is represented by a set of apparent surface charges and currents, which determine an apparent surface charge density that can be used to solve EM scattering equations and compute the absorption and scattering of the dielectric object [92–96, 110–118]. In this work, we report the unprecedented modeling of GNBs by means of the BEM approach, comparing the resulting optical properties with DDA results and with a large set of experimental data, and we introduce a BEM-based modeling for future studies of organic-inorganic nano-hybrids based on GNBs. We first focused on providing a comprehensive theoretical investigation of GNBs to link the LSPR absorption maxima to their morphological characteristics, i.e. various kind of tips or possible base geometries, even when a distribution of GNBs (as synthetic nanoparticles usually appear in solution) is taken into account, thus determining the effect of the statistical distribution of geometrical parameters on the LSPR absorption of GNBs with respect to single GNBs. Then, since the QSA allows for evaluating the coupling between organic chromophores' electronic transitions with the Nanoparticles' plasmon resonance, we employed the BEM approach within the QSA to determine the maximum size of the GNBs that can be modeled with reasonable accuracy, paving the way to the study of GNB-based nanohybrids optical properties.

4.2 Computational details

4.2.1 Codes

Numerical computations of LSPR absorption maxima have been performed using two different codes: SCUFF-EM, a free, open-source software implementation of the BEM method developed by Reid et al. [113, 119]. This code solves the full EM scattering equations, taking into account explicitly the size of the GNBs; and TD-PLAS [118], that is routinely used to compute interaction between molecular electron densities and metal NPs, and presently relies on the QSA approximation.

4.2.2 Sources of data

GNBs' modeling is based on experimental geometrical parameters extracted from transmission electron microscopy (TEM) data of synthetic GNBs, as reported by Chateau et al. [2], Sánchez-Iglesias et al. [3] and from ref.[4]. Among the GNBs synthesized by Chateau et al. [2] we have considered the NPs for which the DDA simulated and the experimental LSPR maxima were reported and whose volumes were explicitly indicated, as determined from TEM images. For the GNBs synthesized by Sánchez-Iglesias et al. [3], we selected the samples where the NPs appeared less aggregated, allowing a more accurate image analysis of the TEM pictures (i.e. the GNBs reported in fig. S10a-c in the Supporting Information of Ref. [3]).

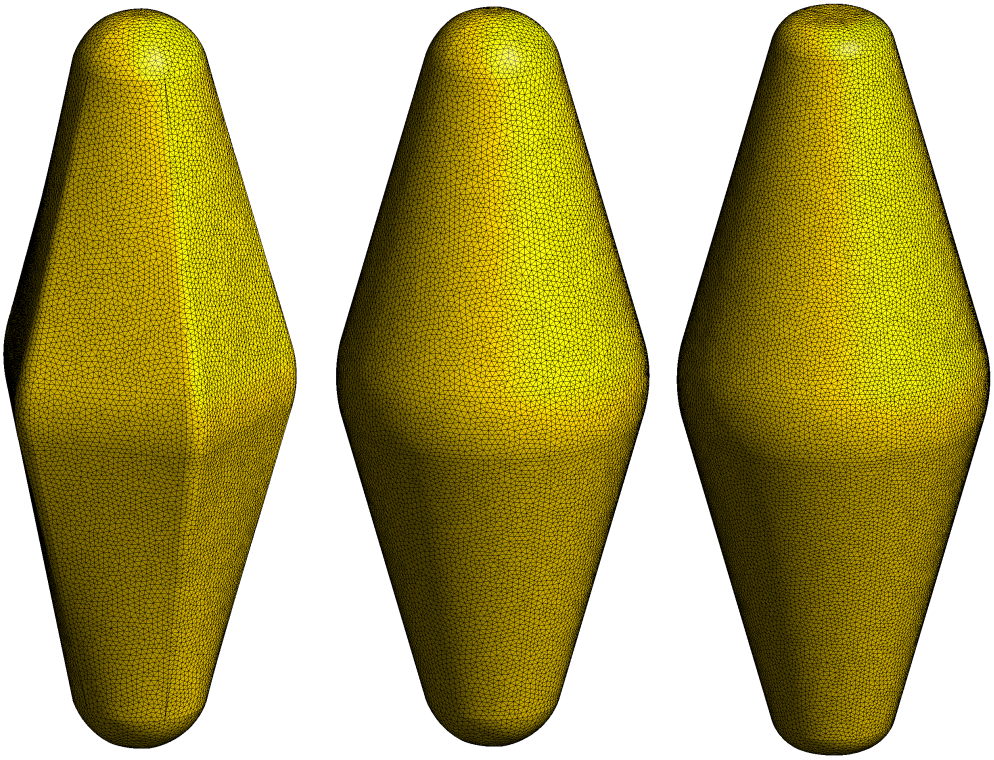

FIGURE 4.1: The three shapes used. From left to right: 1) bipyramid (BPS), 2) spherical tipped bicone (BCS) 3) flat tipped bicone (BCF).

4.2.3 GNBs' modelling

The analysis of TEM images show that the selected GNBs could have either a pentagonal (bipyramids) or a spherical (bicones) base shape. Indeed, the penta-twinned seeds used for the synthesis of GNBs have pentagonal base but GNBs' edges are generally strongly smoothed, as observed in 3D tomographic electron microscopy at the single-particle level and in high-resolution TEM images [13, 103, 109]. Therefore, three GNB model shapes have been here considered:

1. BPS: bipyramid with pentagonal base and spherical tip (BiPyramidal Spherical)

2. BCS: bicone with spherical tip (BiCone Spherical)

3. BCF: bicone with flat tip (BiCone Flat)

The model shapes and their meshes, built using the code GMSH [120], are shown in fig. 4.1. The smoothed edges are necessary to comply with the BEM method requirement of continuously differentiable surfaces and to minimize as much as possible the nonphysical effects arising from infinitely sharp edges, providing realistic descriptions of tip or edge effects. While for the GNBs synthesized by Chateau et al. [2] the shape (biconical), the *AR* (including the truncation level from ideal bipyramids), and the size of GNBs (in terms of volume) were explicitly reported, for the remaining GNBs, these parameters were extracted from the TEM images using the image analysis tools provided by ImageJ [121]. The GNBs models have been thus

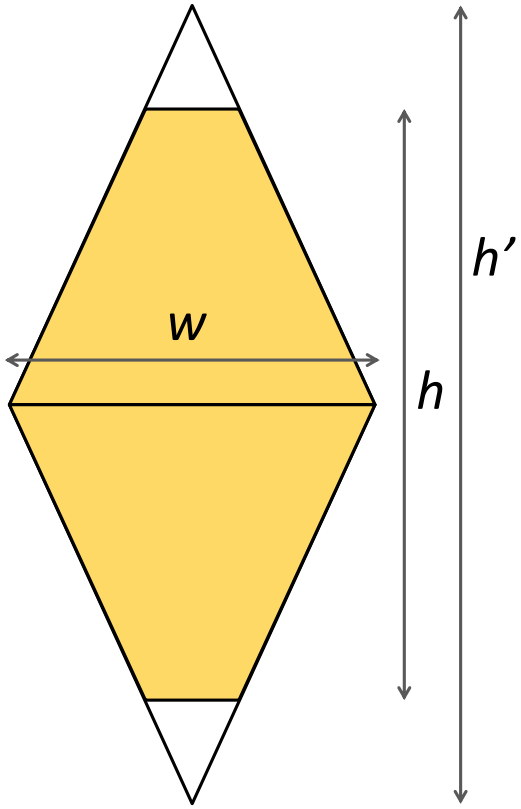

FIGURE 4.2: A graphic representation of the parameters extracted from TEM images in order to build up GNBs for the simulations. w is the GNBs' width, h is the height and h' is the non-truncated ideal height.

determined, for all shapes, from three experimental geometrical parameters for each single NP: i) the width of the bipyramidal base (w); ii) the AR (h/w), where w and height (h) of single particles were considered to be the Feret's minimum and maximum diameter, respectively [122]; and iii) the "ideal" AR (h'/w), namely AR_{Id}, as computed by approximating the 2D projection of the GNB to a truncated rhombus (or the union of two symmetric isosceles trapezoids), as depicted in fig. 4.2. By simple geometrical considerations, the AR_{Id} can be rewritten as function of parameters that can be directly extracted from TEM images, reading

$$AR_{Id} = \frac{h^2}{2(h \cdot w - A)}$$

where A is the 2D projected area of the GNBs as obtained from ImageJ analysis of the TEM images. To build the GNB model of a given sample (associated to an experimental LSPR spectrum), thus, we extracted from its TEM image the w, h and A values for each NP, allowing computing the average $\langle w \rangle$, $\langle AR \rangle$ and $\langle AR_{Id} \rangle$ over the full set of NPs present in the sample. These three averaged parameters allow the construction of an average GNB structure for each sample. The standard deviations

TABLE 4.1: NPs' Parameters

LSPR	Base size (nm)	Aspect ratio	"Ideal" aspect ratio	Shapes investigated
		DATA FROM REF. [2]		
640	11	2.25	3.6	1,2,3
705	15	2.4	3.6	1,2,3
775	22	2.75	3.6	1,2,3
840	25	3.1	3.6	1,2,3
1050	34	4.05	4.7	2
		DATA FROM REF. [3]		
677	18.1 ± 0.9	2.39 ± 0.10	3.67 ± 0.24	2
698	20.1 ± 0.9	2.46 ± 0.13	3.82 ± 0.27	2
732	36.3 ± 2.0	2.73 ± 0.13	3.86 ± 0.29	2
		DATA FROM REF. [4]		
639	34.3 ± 1.4	1.84 ± 0.14	3.25 ± 0.27	2
650	36.7 ± 2.6	2.08 ± 0.14	3.16 ± 0.51	2
650	23.0 ± 0.9	1.97 ± 0.09	3.77 ± 0.20	2
714	21.9 ± 0.8	2.78 ± 0.09	4.38 ± 0.24	2
787	26.3 ± 1.0	3.12 ± 0.12	4.54 ± 0.30	2

of these structural parameters, i.e. $\sigma(\langle w \rangle)$, $\sigma(\langle AR \rangle)$ and $\sigma(\langle AR_{Id} \rangle)$, were also computed, providing a way to estimate the geometrical uncertainty over the simulated LSPR values, due to the use of a single, average GNB structure as representative of each sample. A full list of the GNBs's parameters is reported in the SI, see tab. 4.1. Finally, for the dielectric properties of gold, we employed the analytic approach reported in ref.[51, 52].

4.3 Results and discussion

4.3.1 Assessment of GNBs' model shapes

Figure 4.3 illustrates the effects of *AR* and base size on the LSPR absorption maxima of GNBs particles with the same AR_{Id} and shows the comparison between experimental and theoretical values computed solving the full EM scattering equations, i.e. without limitation in accuracy due to the specific particle sizes and light wavelengths. Previously reported experimental data (in red) and DDA simulations [2] (in blue) are compared with our BEM results, computed with the SCUFFEM code for the three model shapes (being the BPS in yellow, the BCS in green and the BCF in violet) here considered (see section 4.2.3). First, we point out that the DDA results (obtained with a biconical shape) match experimental LSPR absorption maxima only for larger ARs, while at smaller *AR*s the absolute errors increase and also the trend is not perfectly reproduced (see fig. 4.3 and tab. 4.2). This behavior is most likely

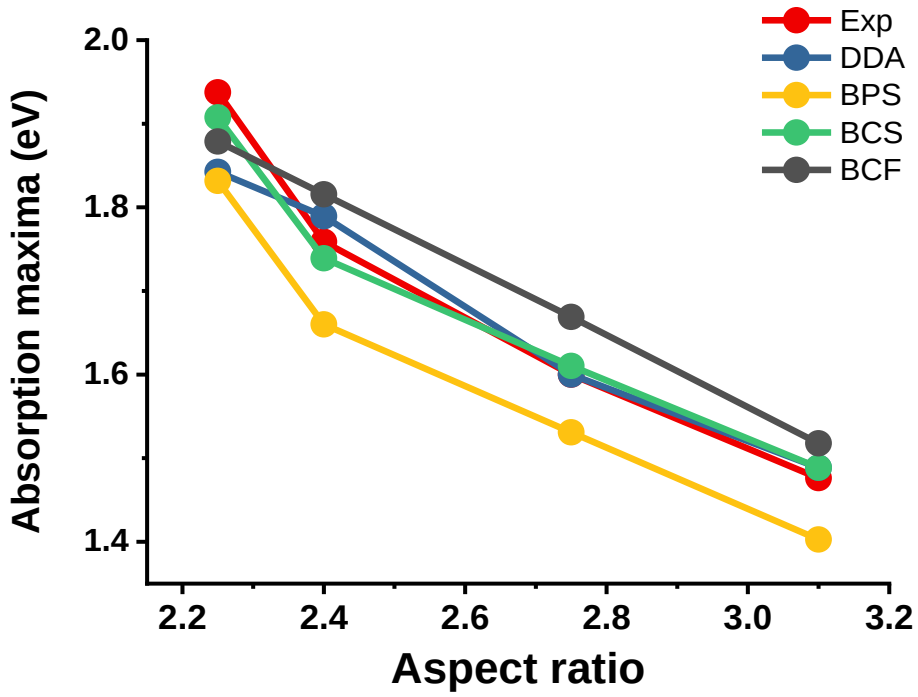

FIGURE 4.3: Effects of *AR* on the LSPR absorption maxima of GNBs particles.

due to the limitations of DDA approach in defining with great details the GNB shape (due to the computational cost of the 3D mapping), which become marginal only when the *AR* and the size of the NP increase significantly. Our BEM computations, instead, do not suffer of such limitations and indeed they provide excellent agreement with experimental data even at small *AR*s if the BCS model, i.e. with round base and spherical tips, is chosen. Notably, if the pentagonal base is considered instead, i.e. the BPS model, the BEM simulations reproduce properly the experimental trends but the LSPR maxima are offset by a consistent and systematic red-shift, always larger than 0.07 eV (see tab. 4.2). This systematic red-shift with respect to the biconical BCS shape is due to the presence of the extended lateral edges associated with the pentagonal base, an effect that is clearly out-weighting the (small) blue-shift one should expect when the overall particle volume reduces by passing from a biconical to a bipyramidal shape. In fact, the decrease of metal NPs size is generally accompanied by a blue-shift of the plasmonic resonance absorption. By comparing the two biconical models, BCS and BCF, it is possible to define the effect of flattening the GNB's tip, which showed to feature two main contributions: i) the increase of volume particle passing from a spherical to a flat tip for GNBs, which blue-shifts the BCS's LSPR absorption with respect to BCF; and ii) the effect of surface sharpening due to the presence of tips, which induces a red-shift of the plasmonic resonance. As shown in fig. 4.3, when the GNB with the smallest *AR* is considered (i.e. $AR = 2.25$), which also features the smallest base size (i.e. $w = 11$ nm), the volume variation due to change of tip shape is significant if related to the overall, relatively small particle volume, indicating the former "volume" effect is probably the dominant one. In

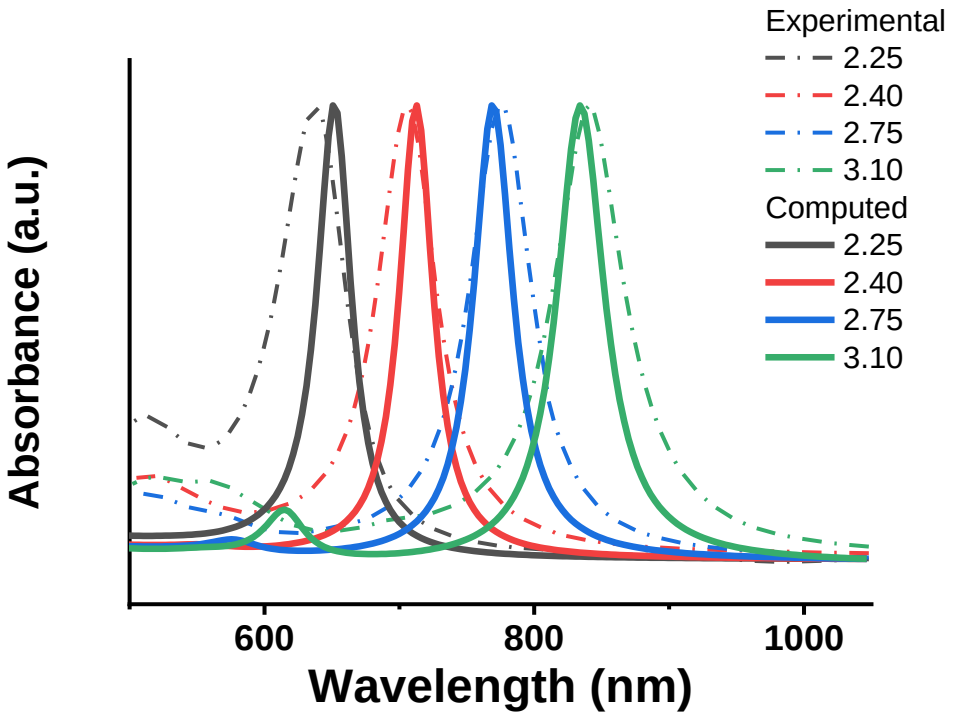

FIGURE 4.4: Simulated absorption electronic spectra of GNBs featuring the various *AR*s showing the AR-dependent shifting of plasmon resonance and the weaker multi-polar resonance at short wavelengths.

fact, this smallest GNB also features a significant truncation percentage of 38% (see tab. 4.2), defined as $(1 - h/h')$ in %, and thus possesses a blunt tip, this minimizing the tip effect independently on the tips shape (spherical or flat). Overall, this explain why, in this case, the BCS's absorption is blue-shifts with respect to the BCF one. Conversely, as the *AR* and the base size are slightly increased (i.e. to $AR = 2.40$ and $w = 15$ nm) and the truncation percentage reduced to 27%, the BCS absorption is red-shifted with respect to the BCF model. This result indicates that, in this case, the volume modification has a smaller contribution than in the previous case (reducing the LSPR blue-shift) and the presence of a sharpened tip determines a sizable tip effect (and thus a red-shift) that is clearly larger for the sharp spherical tip than for the planar flat tip. This trend is essentially maintained if the *AR* and the base size are further increased and the truncation percentage further reduced, but the BCS *vs* BCF absorption difference tends to shrink as a consequence of the reducing size of the tip with the elongation of the GNB particle, which will make fading the importance of the choice of the tip shape as the *AR* increases, see fig. 4.3. The BCS model thus provides the best agreement with experimental evidences and hereafter will be used as the reference shape for all remaining simulations. In fig. 4.4, the absorption spectra of the GNBs at different *AR*s are reported using the BCS reference shape and the BEM methodology. The computed plasmon resonances are, as expected, strongly prominent over the inter-band transitions of bulk Gold (lying at shorter wavelengths, towards the UV spectral window, and not shown in fig. 4.4) and the intensities of

TABLE 4.2: Comparison between full-EM simulations of different GNBs' models and experimental LSPR absorption maxima

w (nm)	11	15	22	25
AR_{id}	3.6	3.6	3.6	3.6
AR	2.25	2.4	2.75	3.1
Tip truncation	38%	27%	19%	11%
	Energies (eV)#			
EXP*	1.94	1.76	1.60	1.48
DDA*	1.84 (-0.10)	1.79 (+0.03)	1.60 (+0.00)	1.49 (+0.01)
BPS	1.83 (-0.11)	1.66 (-0.10)	1.53 (-0.07)	1.40 (-0.08)
BCS	1.91 (-0.03)	1.74 (-0.02)	1.61 (+0.01)	1.49 (+0.01)
BCF	1.88 (-0.06)	1.82 (+0.06)	1.67 (+0.07)	1.52 (+0.04)

*from literature, see main text.
#experimental values in nm (in square brackets); deviations from experiments (in brackets)

the plasmonic bands depend on the volume of the GNBs, i.e. the greater the volume of the particle the more intense is its absorption band. Moreover, for the largest GNB (AR = 3.1) an additional absorption peak due to multi-polar resonance can be detected, which is consistent with the experimental observation of an absorption at around 600 nm for this GNB [2]. Finally, we also checked the effects of the polarization of the exciting electromagnetic field over the plasmonic resonances, see figures 4.10. Thus, for the BCS models described above, we computed the transverse plasmon resonances by considering light polarized along the short axis of GNBs and we found that, for all GNBs here considered, the transverse resonances are located at 506 nm (see fig. 4.10), consistently with the observed experimental ones at around 500 nm.

4.3.2 Assessing base size and truncation effects

Given the good agreement between experimental LSPR maxima and computed values using BEM method for the BSC model, with better accuracy than previously reported DDA computations, we performed simulations on a larger set of synthetic GNBs featuring a wider range of base sizes (up to ca. 37 nm), AR and AR_{Id} (low to 1.84 and 3.16, respectively) and tip truncation percentages (up to 48%), as reported in figure 4.5 and tab. 4.1. As reported in tab. 4.3, the LSPR absorption maxima computed, within the full EM framework, with the BEM approach and BCS geometrical model feature overall a good agreement with all experimental data, with energy difference discrepancies always below 0.06 eV (see fig. 4.6). The simulated LSPR absorptions are computed using an average GNB particle, i.e. averaging the geometrical parameters, i.e. height $\langle h \rangle$, aspect ratios $\langle AR \rangle$ and $\langle AR_{Id} \rangle$, that can be extracted

from the experimental TEM images, as described in section 4.2.3. Computational details,

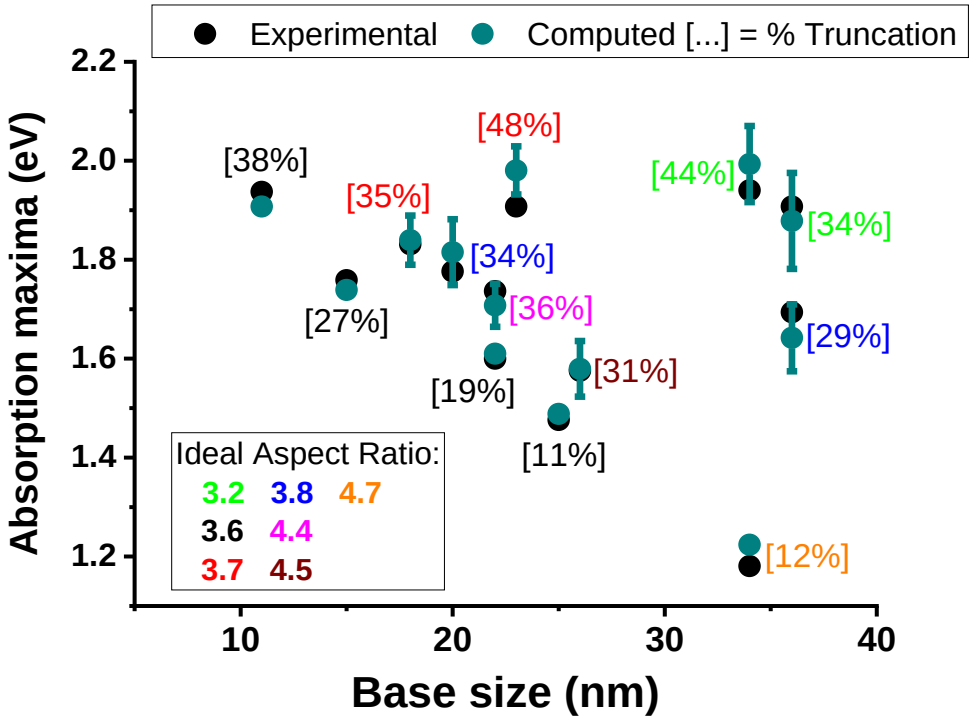

FIGURE 4.5: Summary of the experimental and computed LSPR peaks (with their geometrical uncertainties).

In order to assess the uncertainty of the computed LSPR associated with the geometrical variance of the synthetic GNBs, we analyzed TEM images from the samples reported in [3] and [4]. We used the standard deviations ($\pm 1\sigma$) of the three geometrical parameters $\langle w \rangle$, $\langle AR \rangle$ and $\langle AR_{Id} \rangle$ (see section 4.2.3) to build eight (2^3) GNBs' "extreme cases" models for each sample and we computed their individual LSPR absorption maxima to have a rough estimate of their variation as function of these parameters. In fig. 4.5 we report the largest difference (ξ) in LSPR energy with respect to the average GNBs as ($\pm\xi$) error bars, showing that the geometrical uncertainty derived from the extraction of the GNBs' parameters from TEM images is significantly large at already $\pm 1\sigma$ from the average, and generally even larger than the difference between the simulated and experimental LSPR absorption maxima. This fact suggests that the sensitivity and accuracy of the BEM approach is sufficiently high that the results of the simulations are mostly affected by the choice of the NP extracted from the TEM image and from the corresponding geometrical parameters. This outcome highlights the importance of averaging all the geometrical parameters extracted from TEM images rather than selecting one random single NP from the sample. Finally, we tested how much the result of such protocol differs from the explicit computations of all the LSPR absorption maxima of any NP present in the sample. Since these explicit ensemble computations have a computational cost significantly larger than a (averaged) single particle computation, we performed the simulations for only one representative sample. In particular, we selected the GNB

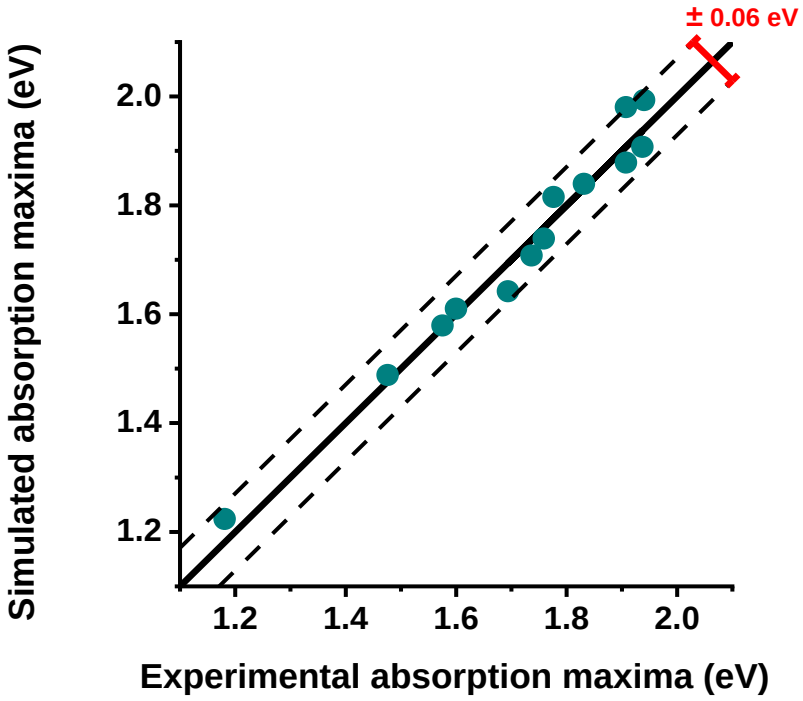

FIGURE 4.6: Experimental absorption maxima vs simulated absorption maxima.

sample featuring both a large geometrically-induced variation on the LSPR energy (i.e. a large ξ) and one of the largest discrepancy between the experimental LSPR maximum and the single-particle theoretical value (i.e. a "large" ΔE(Exp$-$Comp)). We have thus computed the LSPR spectrum of the full ensemble of the GNB featuring an experimental LSPR maximum at 639 nm (i.e. 1.940 eV), featuring ξ = 0.08 and ΔE(Exp$-$Comp) = -0.05, and compared it with the spectrum of the (averaged) single-particle, showing a deviation of LSPR maximum of only 0.01 eV and an almost identical LSPR spectra (with obviously a broader lineshape in the full ensemble spectrum), as reported in figs. 4.8 and 4.9.

In order to verify that the transversal and longitudinal resonances are independent of each other, a simulation has been produced using the NP with *AR* of 2.25, in which the light polarization is rotated from the longitudinal axis to the transversal axis. The intensity has then been normalized up to a value in which the absorption intensity does not depend on the orientation in order to eliminate the difference in size of the cross section when rotating the polarization (the projection on the polarization plane of the NP changes in size while rotating). As is clearly shown in fig. 4.11, we observed a point in the spectrum at 542 nm in which the absorption intensity does not depend on the orientation. The presence of this "isosbestic-like" point shows that the two absorption are independent of each other. This is indeed not surprising, since the framework of these computations is based on first order effects, and thus it would be impossible to observe couplings between orthogonal resonances.

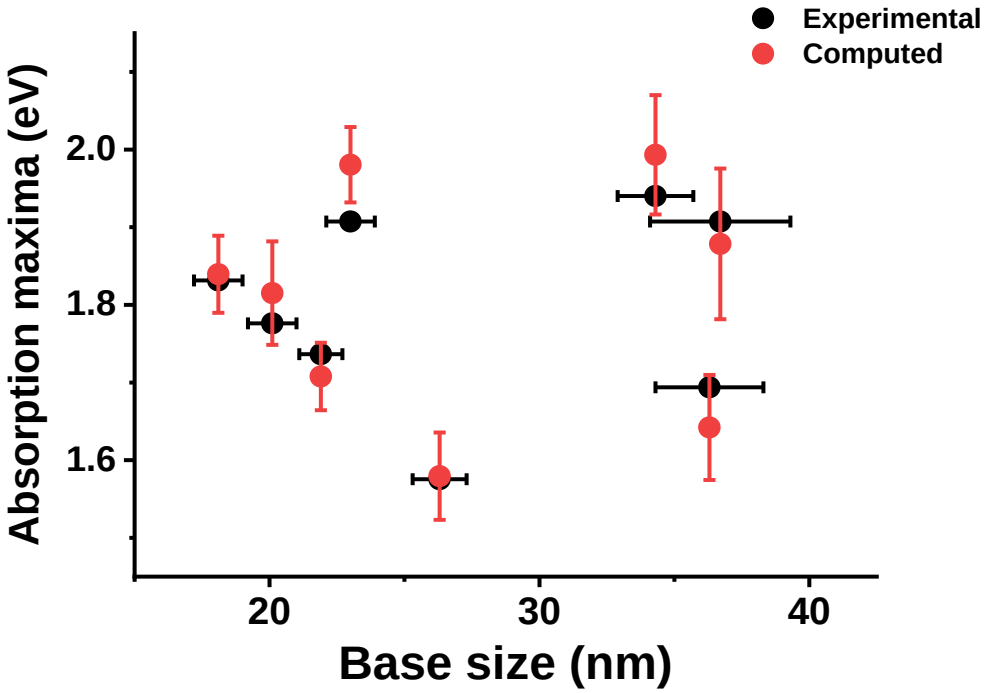

FIGURE 4.7: Computed LSPR with the error bars introduced by the geometrical uncertainty.

4.3.3 Base size limits for quasi-static computations

After validating BEM approach to EM scattering for GNBs particles with broad geometrical variety in terms of base size, AR_{Id} and tip truncation (i.e. AR), we investigated how well QSA results could compare against full-EM computations. The assessment of QSA computations, in fact, is crucial to allow theoretical estimation of interactions between GNBs and molecular transition dipole moments in nano-hybrids materials. Fig. 4.13 reports the comparison of the experimental and full-EM simulations data described in section 4.3.1 with the QSA estimates of the LSPR absorption maxima using the BSC model. The outcome shows good agreement between the QSA results and the full-EM (and the experimental) data. As expected from the intrinsic limitation of the QSA approach (see section 4.1), the accordance worsens while increasing the GNBs' particle size, which (in the reported cases) is associated to an increase of the AR.

In order to estimate the error of the quasi-static calculations associated with the NPs' size, we built a number of NP models with increasing base size (w), keeping AR and AR_{Id} fixed and compared LSPR peaks computed using a full-EM approach (*via* SCUFFEM) or a quasi-static one (*via* TDPLAS). We then computed many different NPs with increasing base size (w), keeping the same aspect ratios (h/w and h'/w, sorted by colour), and the results are summarized in fig. 4.14. The full points are the size dependent SCUFFEM data, the flat lines are the size independent values obtained with TDPLAS and the bigger void circles represent the experimental data. Experimental data fall well into the size dependency expected from simulations. It can

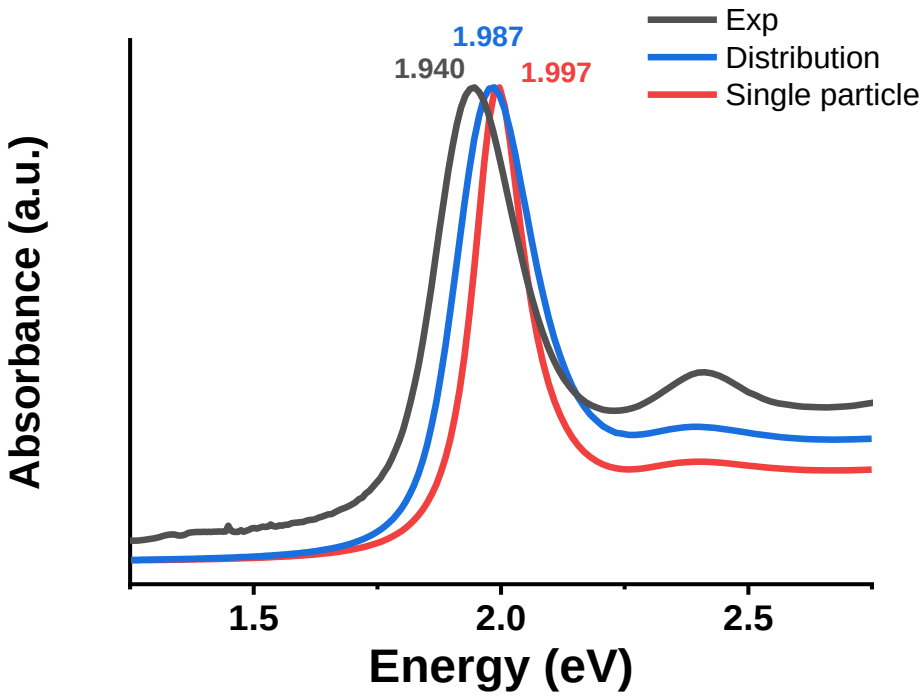

FIGURE 4.8: Experimental LSPR spectrum (black line) of GNB particles with absorption maximum at 639 nm (i.e. 1.940 eV) compared with full-EM theoretical spectra computed.

be observed that the small size limit for the size dependent calculations correspond exactly with the value obtained including the small-size (or *quasi-static*) approximation. As previously mentioned, the full-EM computations show how the increase of the particle base size (that, for a given AR and AR_{Id}, corresponds to an increase of particle volume) is associated with a red-shift of the LSPR absorption, limiting the accuracy of the QSA computations to a finite range of base sizes, which depends on the chosen AR and AR_{Id}. Thus, in order to evaluate the extension of this range we computed the error (in percentage) in QSA absorption energies with respect to full-EM results as function of the base size, for each AR and for a fixed AR_{Id} (equal to 3.6, see tab. 4.2). As shown in fig. 4.15, to stay within an error of 5% in LSPR absorption energy, the maximum base size should be lower than 36 nm for this class of GNBs. Considering that the typical base sizes of GNB objects are below 40 nm (as all GNBs investigated here, see tab. 4.2 and tab. 4.1) and that AR_{Id}s smaller than the one selected (that eventually would slightly reduce the maximum base size value) are not quite common, our result definitively represents a good estimation of the typical base size limit that one can reach one modeling GNBs LSPR absorption spectra within the QSA methodology.

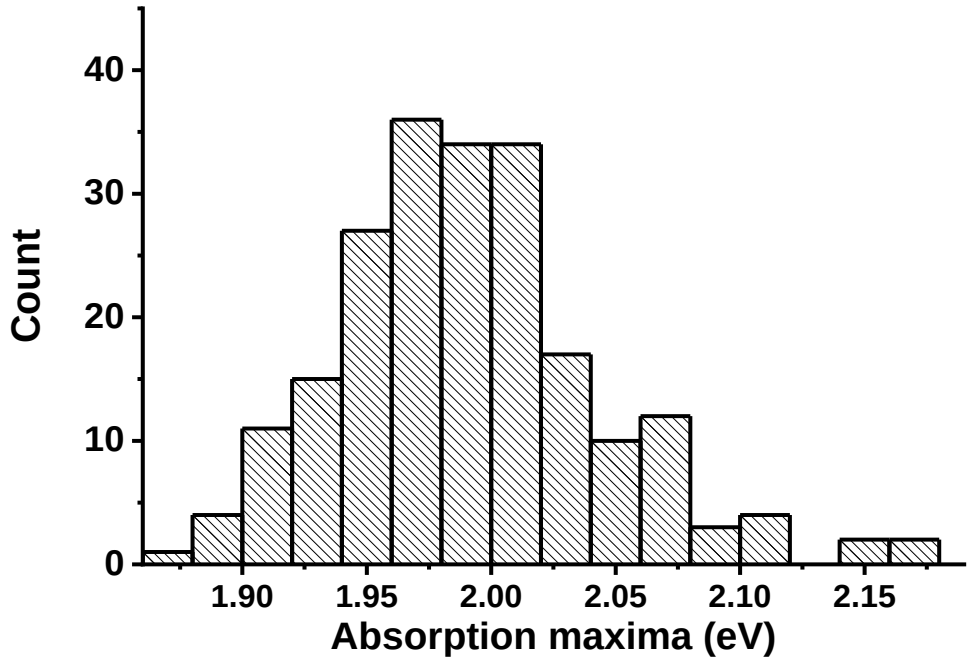

FIGURE 4.9: Histogram representation of LSPR absorption maxima distribution for the full ensemble spectrum reported in fig. 4.8

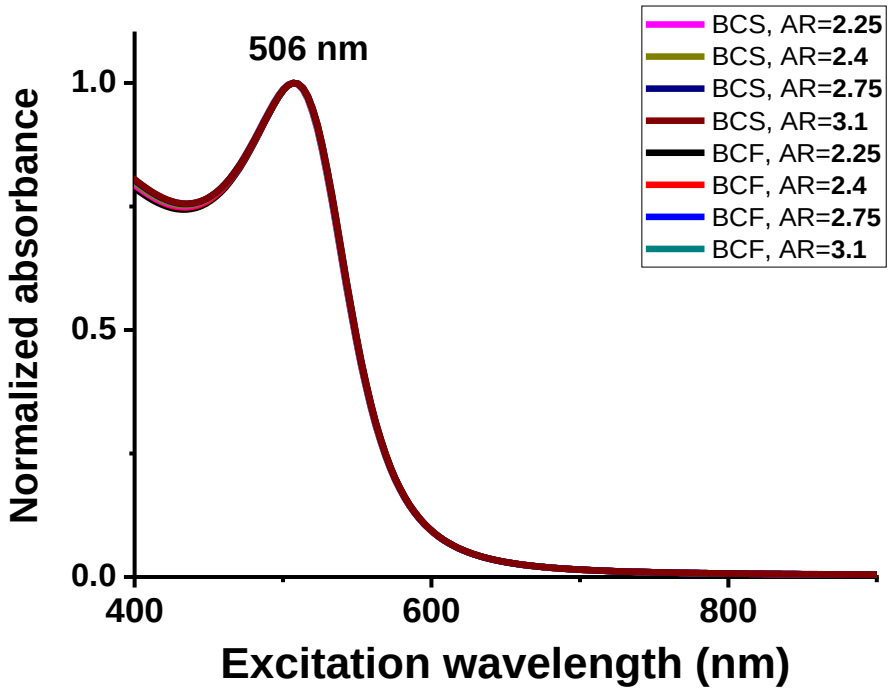

FIGURE 4.10: Normalized absorption spectra polarized along the transversal axis.

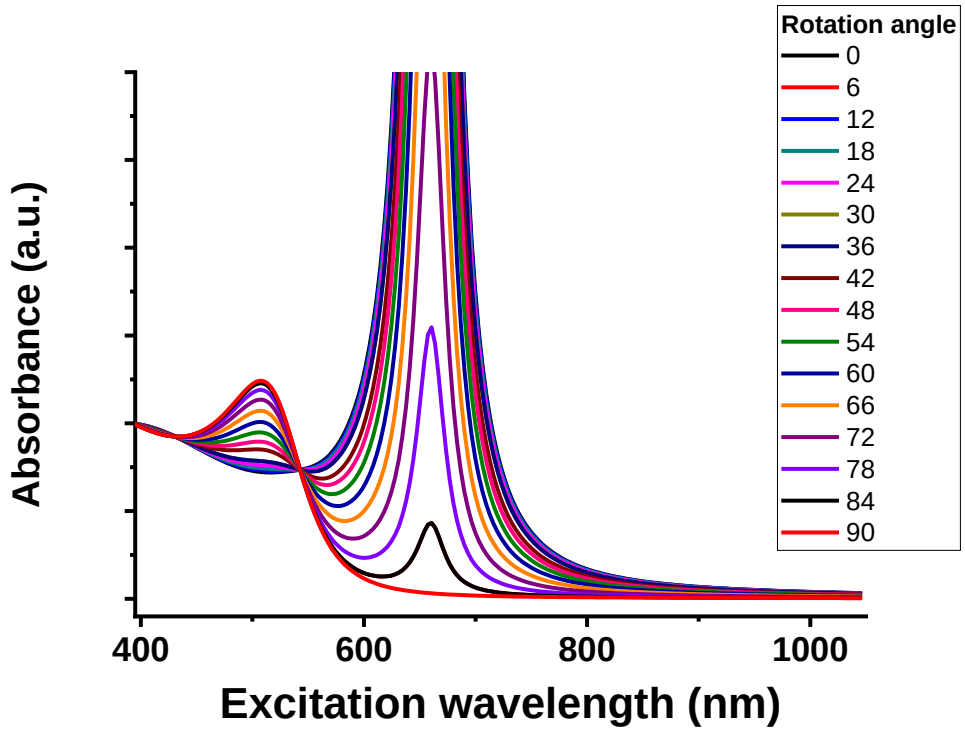

FIGURE 4.11: Normalised absorption spectra upon rotation of the light polarization from the longitudinal to the transversal axis.

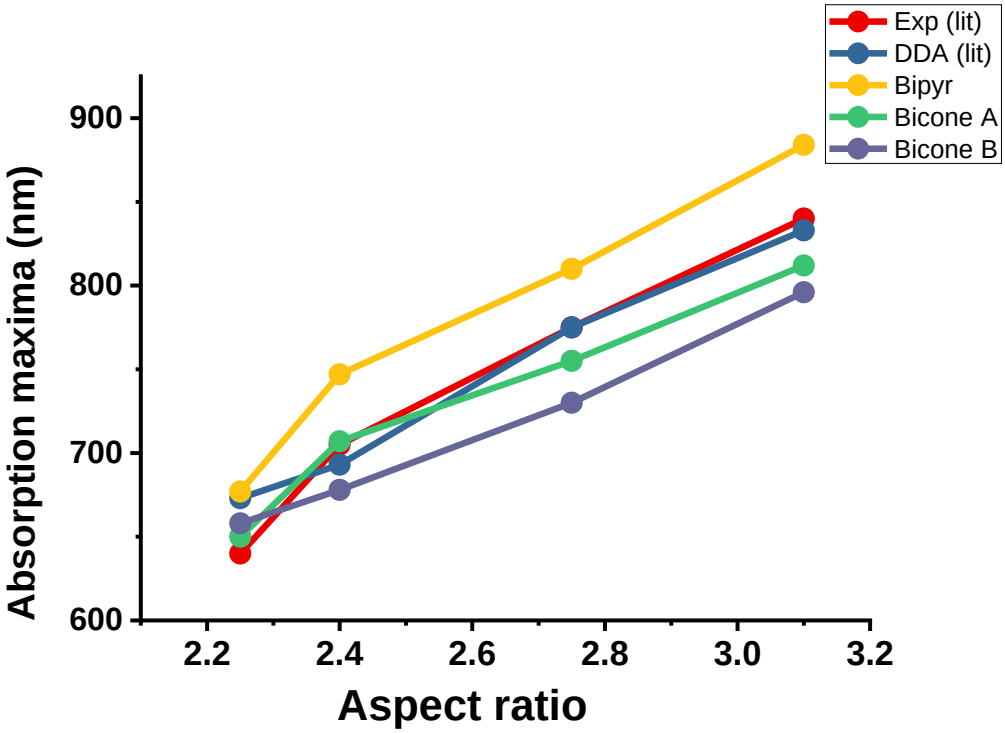

FIGURE 4.12: Effects of aspect ratio over the LSPR, obtained with TDPLAS.

TABLE 4.3: Summary of computed LSPR energies and geometrical uncertainties

Exp LSPR	Computed LSPR	Computed LSPR (eV)	Exp - Comp error (eV)	Geom error (eV)
DATA FROM REF. [2]				
640	650	1.907	0.03	n.a.
705	713	1.739	0.02	n.a.
775	770	1.610	-0.01	n.a.
840	833	1.488	-0.01	n.a.
1050	1013	1.224	-0.04	n.a.
DATA FROM REF. [3]				
677	674	1.839	-0.008	0.05
698	683	1.815	-0.04	0.07
732	755	1.642	0.05	0.07
DATA FROM REF. [4]				
639	622	1.993	-0.05	0.08
650	660	1.878	0.03	0.1
650	626	1.981	-0.07	0.05
714	726	1.708	0.03	0.04
787	785	1.579	-0.004	0.06

TABLE 4.4: Summary of TDPLAS Results

Aspect ratio	2.25	2.4	2.75	3.1
SHAPES	Energies (eV) (in brackets the deviation from EXP)			
EXP (lit)	1.94	1.76	1.60	1.48
DDA (lit)	1.84 (-0.10)	1.79 (+0.03)	1.60 (+0.00)	1.49 (+0.01)
Bipyramid	1.72 (-0.22)	1.67 (-0.09)	1.52 (-0.08)	1.44 (-0.04)
BCS	1.91 (-0.03)	1.75 (-0.01)	1.64 (+0.04)	1.53 (+0.05)
BCF	1.88 (-0.06)	1.83 (+0.07)	1.70 (+0.10)	1.56 (+0.08)

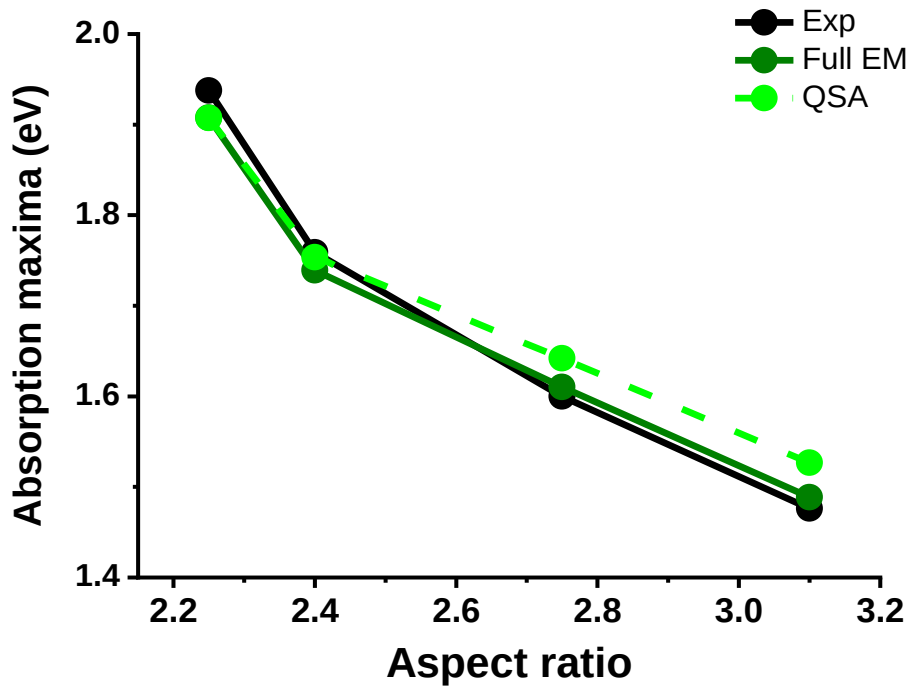

FIGURE 4.13: TDPLAS LSPR peaks compared to SCUFFEM, using only BCS.

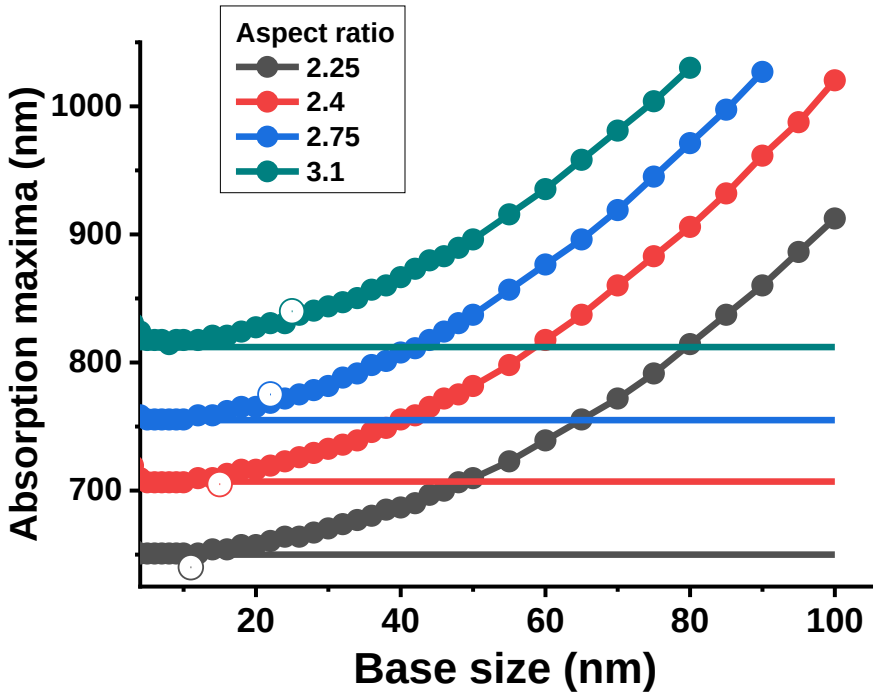

FIGURE 4.14: Size effects over the LSPR. Comparison between full-EM (SCUFFEM) and quasi-static (TDPLAS) calculations.

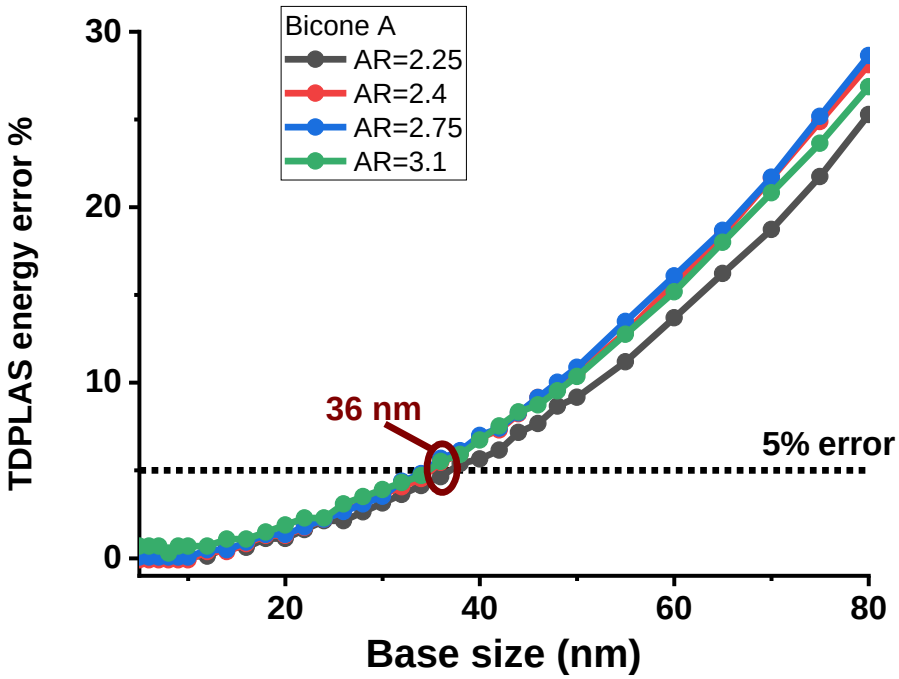

FIGURE 4.15: Error percentage on absorption energy peaks (in eV) between SCUFFEM (full EM) and TDPLAS (QSA) simulations with respect to different base sizes.

4.4 Conclusions

In this work we proved that classical electrodynamics full-EM scattering calculations, solved numerically employing BEM approaches, can accurately describe the LSPR absorption properties of synthetic GNBs' samples, if biconical models with spherical tips are employed. BEM simulations are sensitive enough to the GNBs' geometries that can provide results fully consistent with experimental evidences and with higher accuracy than DDA computations. The GNBs' models can be constructed by extracting geometrical parameters from TEM images of synthetic samples, using a single (random) representative particle, the full set of particles, or an average single-particle obtained by averaging the geometrical parameters over the ensemble of particles. Our results demonstrate that the latter option provides results very similar to the full-ensemble computations, with a gain in computational cost, and suggest that random selection of a single nanoparticle from TEM images to model a GNB could entail a large error on the computed LSPR absorption. Finally, the performances of QSA simulations of GNBs' LSPR absorption spectra have been compared to the accurate full-EM approach, since reliable QSA computations would allow appropriate characterization of the interactions between molecular electron densities and gold nanoparticles that occur in GNB-based organic nanohybrids. Despite QSA computations of LSPR absorption energies are not sensitive to the particle sizes, they proved to be in good agreement with full-EM calculations for an extended range of GNBs' base sizes, proving the applicability of this approach to synthetic GNBs and paving the way to the study of the optical properties of GNB-based nanohybrid materials.

Chapter 5

A Database of the near field enhancement over organic dyes

5.1 Introduction

The presence of a metallic surface in the vicinity of a molecule can deeply modify its optical properties. One of first and most important examples is Surface Enhanced Raman Scattering (SERS), a technique that exploits the enhancement of the Raman scattering of molecules in the vicinity of a rough metallic surface or plasmonic nanoparticles [123–125]. Apart from the very intense amplification of Raman signal, however, the effect of the metal presence can be exceedingly ambiguous, ranging from strong enhancements to complete quenching of the molecular optical signals. This apparently antithetical behaviour might emerge from the intense sensitivity of these systems to the finest of their detail. Many parameters can be modified, achieving compelling differences: which metal is employed, the size and shape of the particle, the position and orientation of the dye with respect to the metal surface, and the overall surroundings around the hybrid system. For example, the surface-chromophore distance plays a strong role in determining the nature of the effect of the metal, drifting from quench to enhancement of the fluorescence brightness [125–127]. While *ab initio* description of the interaction of the molecule with small metal clusters, counting just a few atoms, have been implemented to represent the chemisorption effects [128–130], these small systems cannot reproduce the behaviours of plasmonic metallic nanoparticles, which are composed of thousands of atoms, as is already stated in chapter 3 of this work. Other approaches have been implemented in the many years that these systems have been studied at a theoretical level since their discovery, and can be found in some reviews, such as [91, 131]. If the chemical bond between the chromophore and the metal surface is not a main contributor to the optical properties, *i.e.* the molecules are not chemically bound to the surface, or are far enough to consider them as physisorbed onto the surface, the wavefunctions do not overlap and the direct electron transfer is negligible. This allows to treat the interaction with the tools of the solvation model, where the metal is described as a continuous body characterized by electric response properties only [92]. While other works develop further this implementation of PCM [1, 93, 95, 117], the focus has always been describing the interaction of some specific dye, with its optical properties, in a specific environment. This approach is very useful in order to give insights on the mechanisms involved, and interpret *post hoc* experimental data, but does not provide directly with directions and clues on which systems are

more suitable for a desired application. Therefore, in this chapter, we focused on exploiting the existing tools to provide a routine that allows to build up a detailed database of the optical enhancement, or contraction, of some key parameters that define the performance of the combined system. The goal is to map the surface effects, surveying all the possible parameters with the finest grain possible, taking into account the size and shape of the metallic nanoparticle, the dye-metal distance, the orientation of the dye with respect to the surface, and the characteristics of the chromophore optical properties, such as the absorption and fluorescence wavelengths, the intensity of the transition to, and from, the excited state, or the orientation of the transition dipole moment (TDM). Since the number of parameters considered is high, this results in a huge amount of simulations to be performed, therefore, we adopted a rather simplified approximation, where the metal nanoparticle is represented by its surface polarization charges, according to the PCM tools, and the molecular absorption and emission are represented by the point-like transition dipole moments of the excitation, and deactivation, involved. The code used is TDPLAS (all the details are listed in chapter 4), that has been developed exactly with the purpose of studying the metal-chromophore interactions in the hybrid system.

5.2 Computational Details

5.2.1 Main Parameters

To compute the radiative decay constant the Einstein relation has been used:

$$\Gamma_r = \frac{4\omega^3}{3\hbar c^3}|\vec{\mu}_{k0}^{tot}|^2$$

Where ω is the energy of the transition from the ground to the k^{th} state and $\vec{\mu}_{k0}^{tot}$ it transition dipole moment. This works either for an isolated molecule, where the $\vec{\mu}$ is just the TDM of the molecule, and in the presence of a metal surface or object, where the total TDM is given summing the molecular TDM with the correction computed by Tdplas:

$$\vec{\mu}_{k0}^{tot} = \vec{\mu}_{k0}^{0} + \vec{\tilde{\mu}}$$

Where $\vec{\mu}_{k0}$ is the TDM of the molecule in the complex environment, while $\vec{\tilde{\mu}}$ is the dipole induced in the metal/solvent by the molecular transition

The nonradiative decay constant is computed by Tdplas using the relation:

$$\Gamma_{nr} = \Im\mathfrak{m}\left\{K_{st,uv}^{pol}\right\}$$

Where

$$K_{st,uv}^{pol} = \sum_i q_\omega(s_i,[\psi_s^*\psi_t])V(s_i,[\psi_u^*\psi_v])$$

Where $V(s_i,[\psi_u^*\psi_v])$ is the electrostatic potential generated by the distribution of charge $\psi_u^*\psi_v$ at the point s_i on the cavity surface, and $q_\omega(s_i,[\psi_s^*\psi_t])$ is the apparent charge placed in s_i. The real part of $K_{st,uv}^{pol}$ results into the excitation energy corrections.

We know also that the value for the i^{th} component of the induced TDM can be written as:

$$\vec{\tilde{\mu}}_i = -(\mathbf{A}\mathbf{D}^{-1}\mathbf{n}_i)\mathbf{V}^{tr}$$

Where **A** is the diagonal matrix of the tesserae areas, **D** is the characteristic matrix of DPCM (dielectric PCM, opposed to the Green's function approach to PCM that is not available for arbitrary shape), $\mathbf{V}^{tr}$ is the molecular electrostatic potential, and $\mathbf{n}_i$ is the i^{th} tessera vector, perpendicular to the tessera surface.

It is possible to quantitatively evaluate the effect of the metal on the absorption efficiency, using the following relation:

$$A = \frac{2\pi}{3\hbar^2 c n_1}|\vec{\mu}_{k0}^{tot}|^2$$

Along with the very same ingredients used for the emission process.

Other quantities have been computed from these main parameters, which are more interesting on a experimental point of view since they give a more immediate grasp of the effect of the NP over the transitions. These are: The adjusted quantum yield (Φ_{adj}), a quantum yield corrected with an additional Γ_{nr} that accounts for all the nonradiative deactivation processes that are present within the molecule *in vacuo*. These can be computed either from some QM method, or, much simpler, can be extracted starting from a hypothetical internal fluorescence quantum yield (Φ_{int}, chosen by us), and then calculating this additional Γ_{nr}^0 knowing the Γ_r from the TDM (which is one of the external inputs), using the following relation:

$$\Gamma_{nr}^0 = \frac{\Gamma_r(1-\Phi_{int})}{\Phi_{int}}$$

Therefore, the adjusted quantum yield (or Φ_{adj}) becomes:

$$\Phi_{adj} = \frac{\Gamma_r}{\Gamma_r + \Gamma_{nr} + \Gamma_{nr}^0}$$

For a chosen Φ_{int}.
This advanced parameter gives a better idea on the actual effects of the NP on the photonics of the dye: if the $\Phi_{adj} > \Phi_{int}$, or better, $\frac{\Phi_{adj}}{\Phi_{int}} > 1$, for any value of TDM, transition energy or others, it means that with those parameters the NP not only enhances the intensity of the luminescence, but it also enhances the actual quantum yield.

Another advanced parameter is the relative brightness, that gives an idea of the enhancement of the luminescence magnitude of the system with and without the NP.

It is computed as:

$$M = \Phi_{adj}\frac{A}{A_0}$$

Where A is the absorption computed using the $\vec{\mu}_{k0}^{tot}$ as written previously, and the A_0 is the absorption computed using the unitary TDM, $\vec{\mu}_{k0}$

Another parameter that can be computed to investigate the photonic enhancement due to LSPR is the number of excited states, relative to the amount of excited states created without the presence of the gold nanoparticle. This quantity (ξ) is proportional to the absorption ratio and the lifetime of the excited state, and it should be normalized with respect to the same parameter computed without the nanoparticle, therefore it can be computed as such:

$$\xi = \frac{A\tau}{A_0\tau_0} = \frac{A}{\Gamma_r + \Gamma_{nr} + \Gamma_{nr}^0} \frac{\Gamma_r^0 + \Gamma_{nr}^0}{A_0}$$

With this form, this parameter is simplifiable to the Φ_{adj}, but it has the peculiarity to take into account both the absorption process and the emission. This gives the chance to introduce the dependency on the energy of the two processes independently, in particular when the energy of the absorption is different from the fluorescence one. Therefore this parameter makes it possible to give an idea on the impact on the enhancement intensity of an eventual Stokes shift. Supposing that the absorption process happens at wavelength λ and the Stokes shift is δ, we can write:

$$\xi(\delta) = \frac{A(\lambda)}{\sum \Gamma_i(\lambda + \delta)} \frac{\sum \Gamma_i^0(\lambda + \delta)}{A_0(\lambda)}$$

These last two parameters give lots of experimental information since they include both the effects of the enhancement in the absorption and the increase, or decrease, of efficiency of the emission process, giving the result of the balancing of these two effects. If the presence of the NP decreases slightly the Φ_{adj} but greatly increases the absorption of the dye, the total effect is an increase of the luminescence, and this shows either in M and ξ. On the other side, if the increase of the absorption is accompanied by a strong quench of the emission, the total effect is going to be a quench of the luminescence, which shows in both parameters as well.

5.2.2 Numerical Setup

In order to check the effects of different aspect ratios of the nanoparticles, two NPs were chosen, in such a way that one has a lower aspect ratio and less tip effects, and one a higher aspect ratio, resulting in a sharper tip. The base geometry is the spherical tipped bicone from Chapter 4. The first NP has a AR of 1.84 and an AR_{id} of 3.25, while, for the second NP, the AR is 2.75 and AR_{id} is 3.6. These values correspond to two of the experimental NPs treated in the previous chapter, in particular with the ones presenting LSPR at 639 nm and 775 respectively. Using the *quasi-static* approximation through TDPLAS, the absorption maximum (which means the LSPR energy level) are computed at 600 nm and 723 nm respectively. The blue-shifted error is due to the absence of size-dependent effects through the electrostatic approximation. A full Mie treatment using SCUFF-EM gives a LSPR at 622 nm and 770 nm, much nearer to the experimental values with an error of just 0.05 and 0.01 eV

In order to have a broader idea of the effects of the NP over the optical properties of molecules, instead of real-life dyes' parameters, a whole spectrum of excited states from 300nm to 900nm have been used with unitary point-like transition dipole

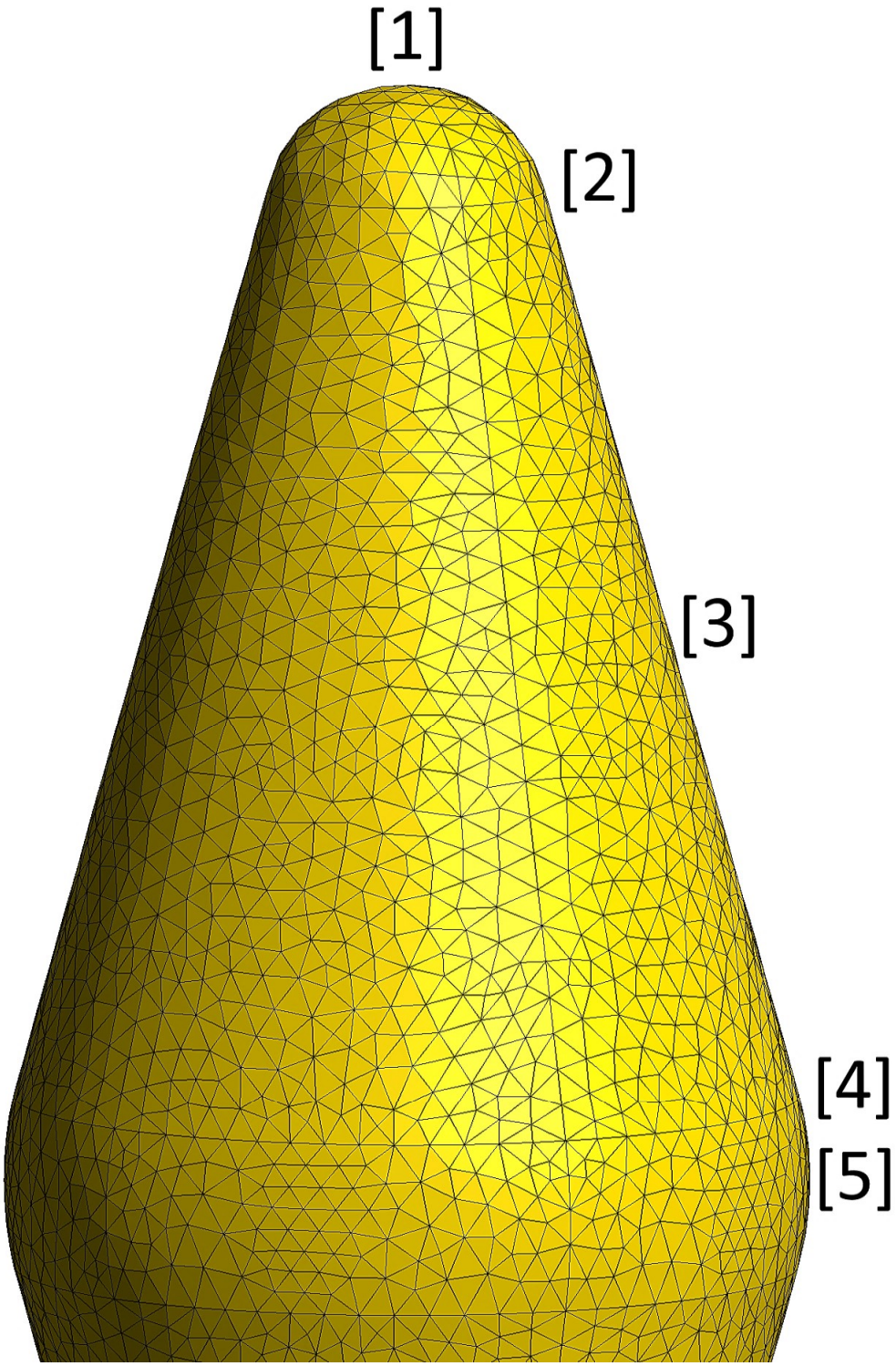

FIGURE 5.1: Positions considered as location of the interacting dye: [1] is “tip", [2] is “tip_side", [3] is “middle", [4] is “side_up", [5] is “side"

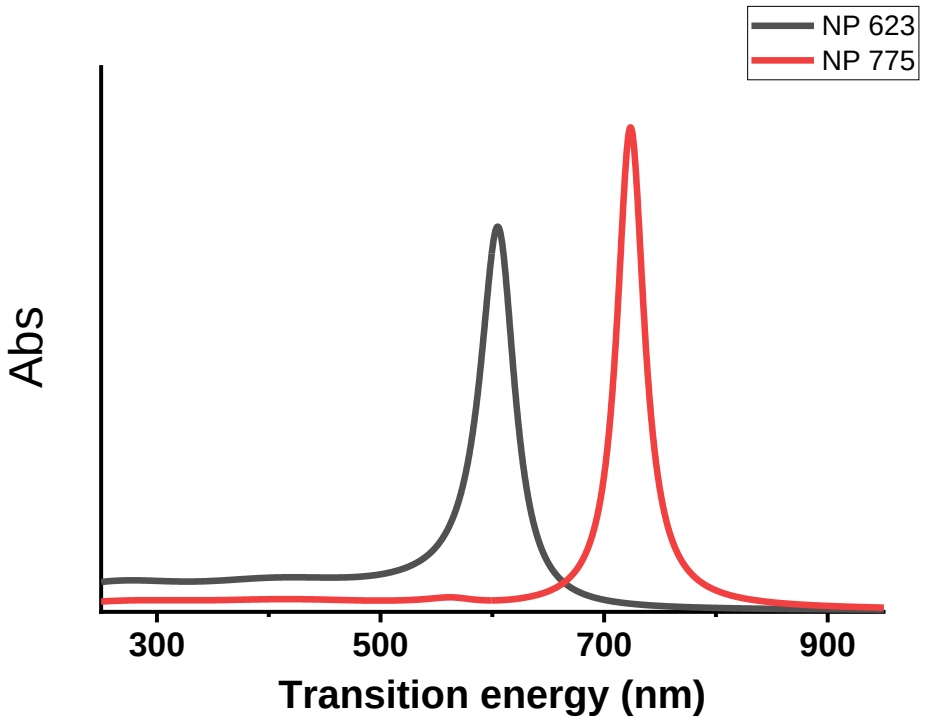

FIGURE 5.2: Computed spectra of the two NPs studied

moment. This means that computations give an idea of different effects of the interaction between the plasmon resonance and the molecular excited states at different excited states energies. Five different positions have been used for the molecular models (see fig. 5.1). These are called respectively:

- position [1] is named “tip"
- position [2] is named “tip_side"
- position [3] is named “middle"
- position [4] is named “side_up"
- position [5] is named “side"

For each position molecules have been put at different distances from the surface, ranging from 10 to 100 Bohr. In particular, here are reported distances at 10, 55, and 100 Bohr. Different orientations have been investigated too: perpendicular to the surface, parallel to the surface, and tilted 45°in various symmetrically-relevant directions.

To show where on the spectrum the two nanoparticles interact, in fig. 5.2 are presented the absorption spectra of the two nanoparticles taken into account when excited with an external oscillating electromagnetic field.

5.3 Results for NP 623

5.3.1 Emission

Dye perpendicular to the surface

In fig. 5.3 is shown the Quantum Efficiency Φ of the probing molecular excitations, located at the tip position at the three different distances. It is evident that the Φ increases with the increase of the distance, with a maximum around the LSPR energy. This is due to the high increase in the value of the non-radiative decay constant (see fig. 5.10) that increases exponentially getting closer to the surface, which neglects the effect of the slight increase of the radiative decay constant (fig. 5.7). This shows its strongest effect in the lifetimes of the excited states, since a difference of 3 orders of magnitude is observed passing from near to far from the surface, as seen in fig. 5.13.

The effects of position of the molecules over the surface of the NP is also quite interesting: as it can be seen from fig. 5.4 when near the surface, Φ is very dependent on the frequency of the transition, and this dependence is influenced strongly by the position. The nearest to the top of the tip, the strongest is the effect at the LSPR frequency, with a strong quench happening at slightly higher frequencies (or lower wavelengths). When near the side (positions 4 and 5) this LSPR effect is almost neglected. One interesting thing is seen in fig. 5.8, where you can observe the arise of interaction with longitudinal or vertical LSPR getting nearer to the side or the tip respectively, with humps of both at in-between positions.

Lifetimes reflect these characteristics: the nearer you get to the surface, the faster is the decay process. The energy transfer from the molecule to the metal is exponentially stronger the nearest the molecule is to the metal surface and this reflects into a much faster decay process of the excited state through Γ_{nr}.

The intensity of the enhance or quench due to the NPs has its origin on the phase of the image dipole projected onto the metal surface. Since there is a delay between the oscillation of the dye's TDM and the response of the image dipole, creating a phase shift, at some excitation energies the phase shift is such that the image dipole is oriented in the same direction of the dye's TDM, while at other transition energies they are in counterphase. When the intensity of the image dipole is much higher than the molecule's TDM, it results in the observed enhancements no matter the orientation (since they are summed and the dye's TDM, if much smaller, doesn't affect much the outcome). On the other side, when the intensity of the two are comparable, if their orientations have the same direction, they sum up creating an enhancement, while if they are in counterphase it quenches greatly the effects. In some cases, like in fig. 5.13, for a dye at 100 Bohr from the NP there is an interval of energies where the Γ_r is even lower than the one without any NP. In literature these are called *cold spots* [132].

In fig. 5.6 is presented the effect of the orientation of the dye over the quantum yield when on the tip at a distance of 100 Bohr from the surface. The orientation shows that only when completely perpendicular to the surface, and thus perpendicular to the LSPR orientation at this position, the effects of the coupling with the LSPR are not present.

Dye parallel to the surface

Similar general effects can be observed when the orientation of the TDM is put parallel to the surface (pointing upwards). In fig. 5.14 is shown the effect of the distance at tip position. Also in this case getting nearer to the surface means a strong quench of the emission. The main difference is the absence of a peak corresponding to the LSPR associated with the long axis of the Gold NP, since the orientation of the TDM is orthogonal and does not couple with it, within the limits of this approximation that does not account for higher order interactions. The coupling with the vertical LSPR (which is the strongest one) can be observed at the other positions, where the orientation parallel to the surface brings to a component of the TDM to be parallel to the vertical LSPR. In fig. 5.15 and fig. 5.16 this effect is evident, as it can be observed that no bump appears at the tip position while it arises at the other sites. The intensity of the effect is dependent on the position and the orientation, since at side position (which, for geometry, entails a orientation of the TDM parallel to the vertical LSPR), the coupling is maximized with respect to the orientation, while the strongest effect is seen at middle position, probably for the most effective balance between the distance with the NP's axis and the orientation.

The same principles can be observed in Γ_r and Γ_{nr} plots (Figs from 5.17 to 5.22) where the effects at tip position show no coupling with the vertical LSPR while the rest have the already explained increased effects. In fig. 5.17 it is evident that at tip position since no coupling with the LSPR is present there is only a quench from the presence of the metal NP, especially at energies slightly above the LSPR energy, where the image dipole is in counter-phase with the TDM of the dye. In fig. 5.18 it is shown that when near the NP the stronger effects are given by the vertical LSPR, with a small detachment from no effects at higher energies and a strong quench a lower energies, while in fig. 5.19 the effect of the LSPR is even stronger (since the pure surface effects are smaller for the much wider distance), detaching from the no-effect only at the LSPR energy. An interesting phenomenon can be observed in fig. 5.21 and fig. 5.22, where the Γ_{nr} clearly feel much more the effect of the longitudinal LSPR instead of the vertical one, with smaller bumps present, when far, only at middle, side_up and side positions due to the coupling given by the orientation.

5.3.2 Quantifying the enhancement performance

While decay constants and quantum yields are precious parameters to investigate the underlying causes of optical effects, when addressing the effective outcomes of the presence of the NP the other parameters listed in section 5.2.1. In particular, the most interesting parameter to take into account is the effective brightness M, that epitomizes the overall influence of the NP, since it addresses not only the internal effects that bring to the emission, but also the field enhancement over the emitted light. When the dye is located at a far distance and perpendicular to the surface, the relative brightness increases for wavelengths longer than the LSPR (fig. 5.23), in some cases strongly, more than two orders of magnitude, with a peak at around the LSPR itself (600 nm in this case), and lowered for $\lambda <$ LSPR. For other distances and orientations the general trend is a quench of the relative brightness, except for a few situations, where the orientation perpendicular to the LSPR summed with a position at (or near) the tip favours an increase around the LSPR wavelength figs. 5.24, 5.25, 5.26). In

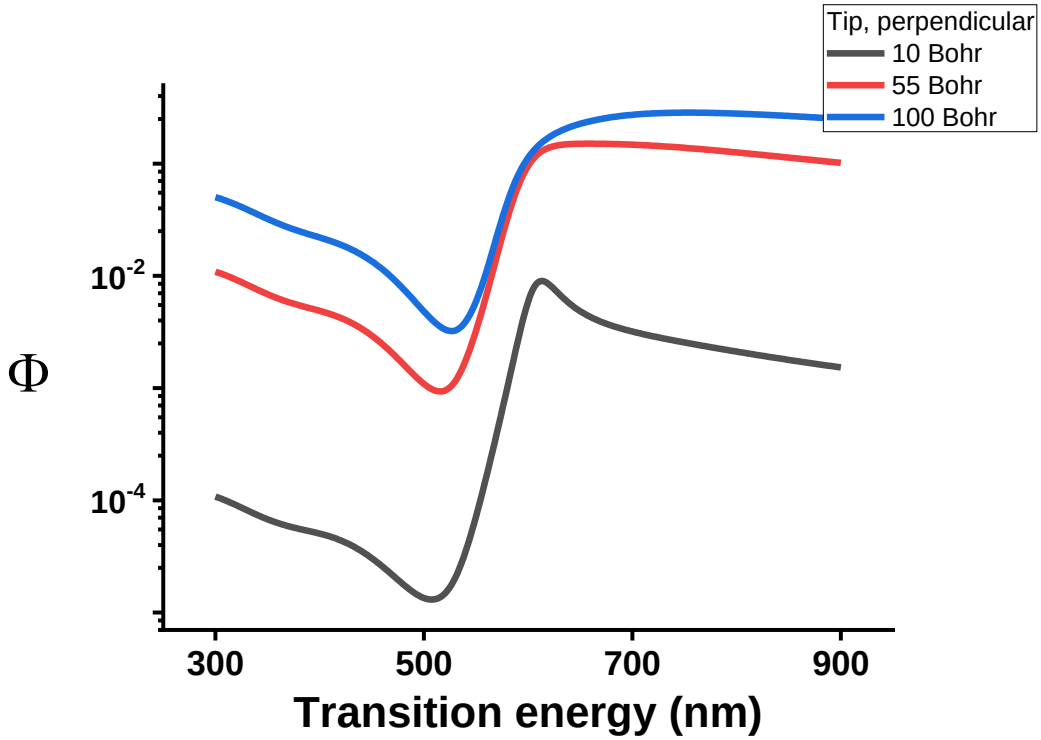

FIGURE 5.3: The effects of the tip of NP 623 over the quantum yield of a set of dyes with transitions from 300 nm to 900 nm, oriented perpendicular to the surface, at different distances from the metal.

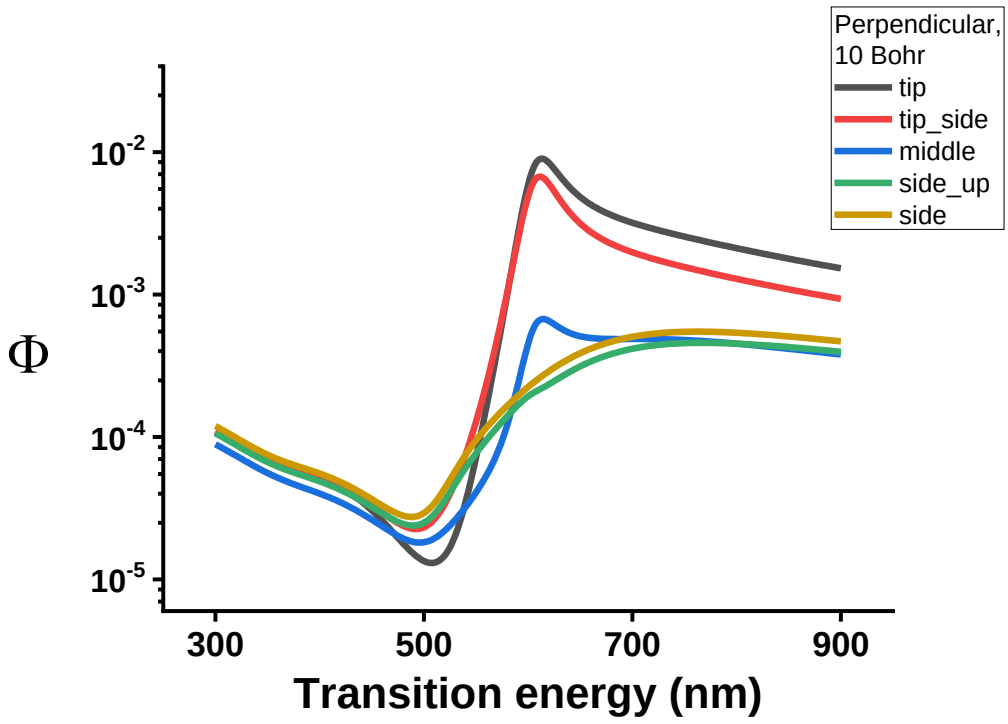

FIGURE 5.4: The effects of NP 623 over the quantum yield of a set of dyes with transitions from 300 nm to 900 nm, at different positions, oriented perpendicular to the surface, at 10 Bohr from the metal.

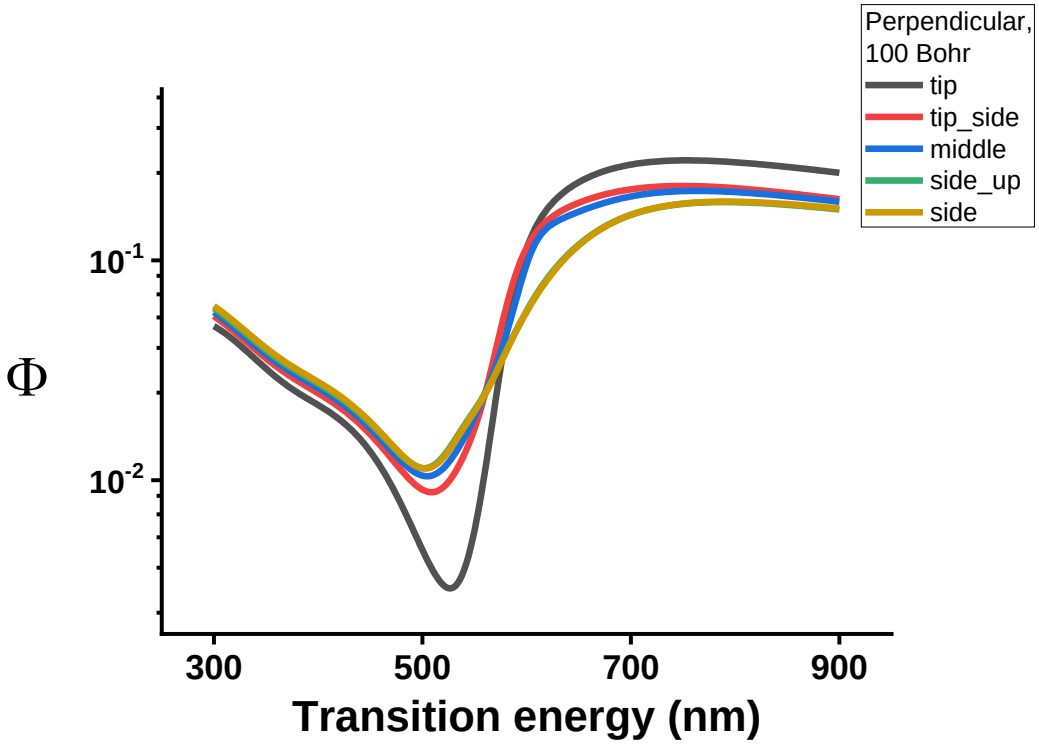

FIGURE 5.5: The effects of NP 623 over the quantum yield of a set of dyes with transitions from 300 nm to 900 nm, at different positions, oriented perpendicular to the surface, at 100 Bohr from the metal.

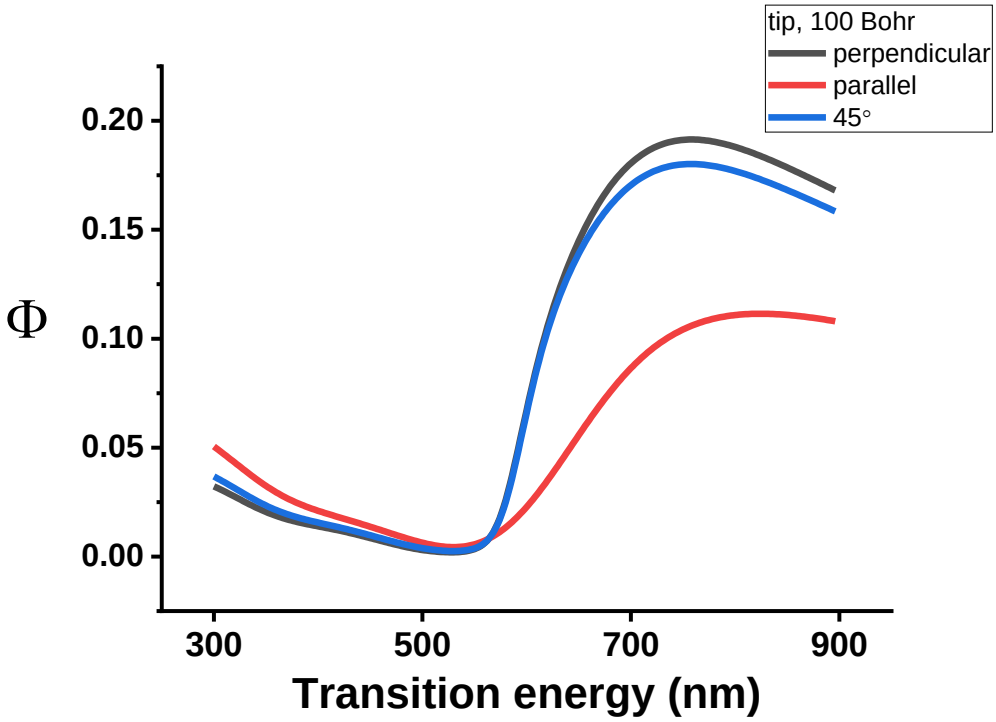

FIGURE 5.6: The effects of the tip of NP 623 over the quantum yield of a set of dyes with transitions from 300 nm to 900 nm, at 100 Bohr from the metal surface, with different orientations.

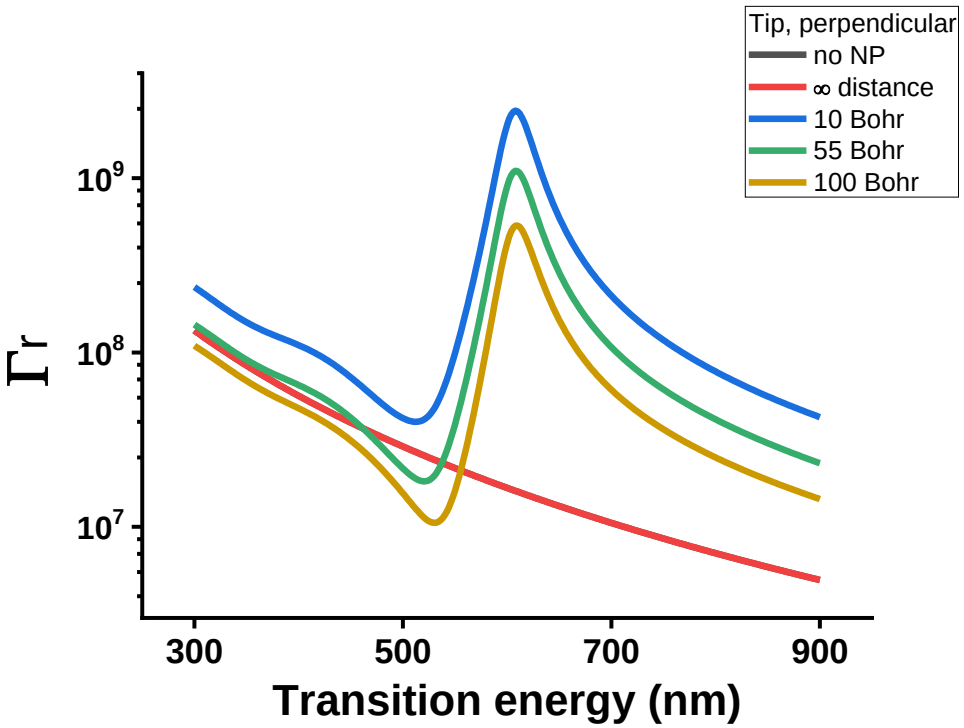

FIGURE 5.7: The effects of the tip of NP 623 over the radiative constant of a set of dyes with transitions from 300 nm to 900 nm, perpendicular to the surface, at different distances from the metal.

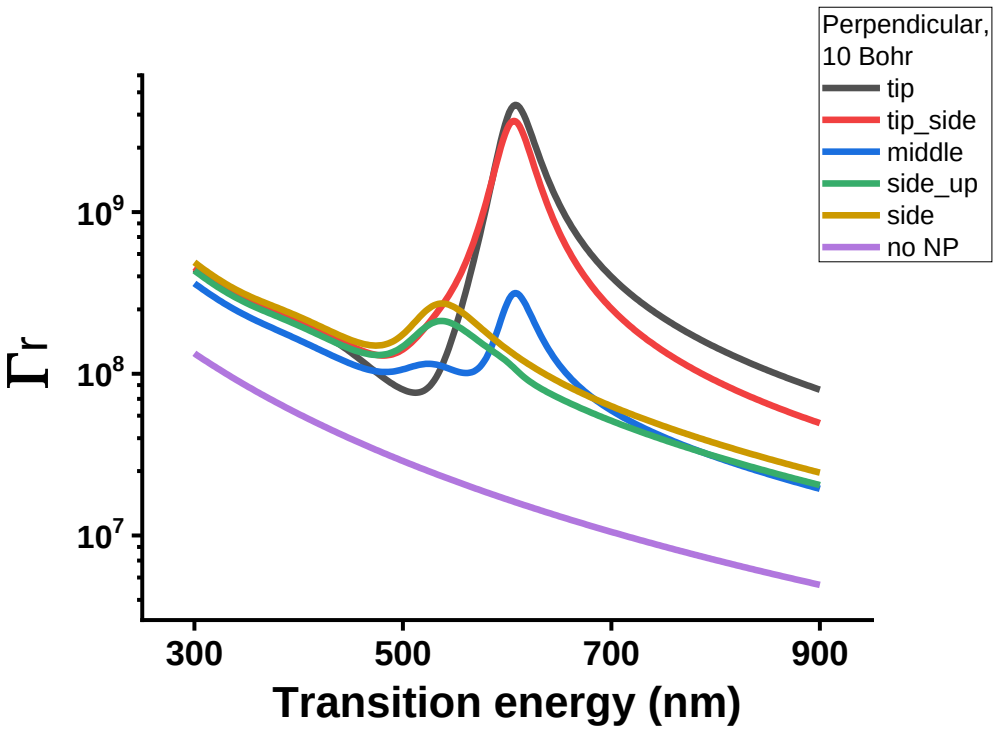

FIGURE 5.8: The effects of various positions on NP 623 over the radiative constant of a set of dyes with transitions from 300 nm to 900 nm, perpendicular to the surface, 10 Bohr from the metal.

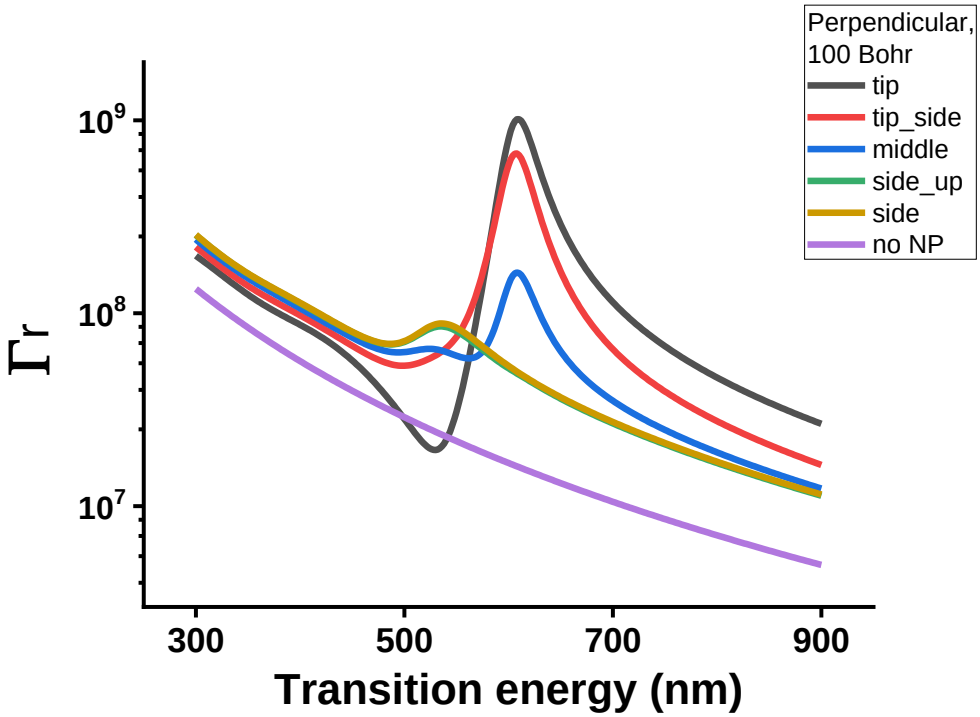

FIGURE 5.9: The effects of various positions on NP 623 over the radiative constant of a set of dyes with transitions from 300 nm to 900 nm, perpendicular to the surface, 100 Bohr from the metal.

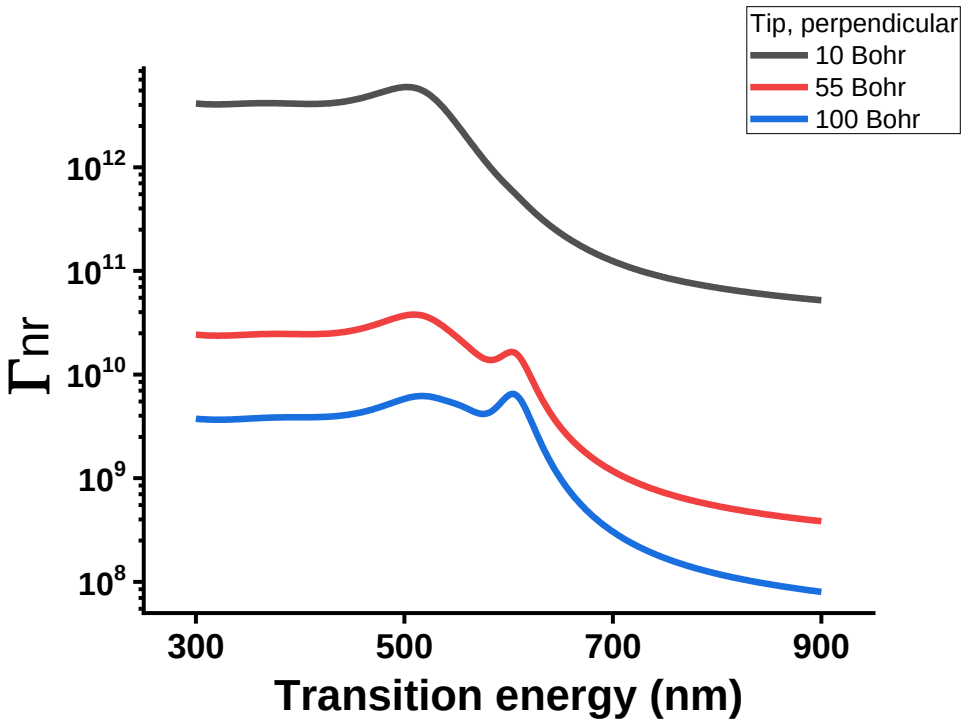

FIGURE 5.10: The effects of the tip of NP 623 over the nonradiative constant of a set of dyes with transitions from 300 nm to 900 nm, perpendicular to the surface, at different distances from the metal.

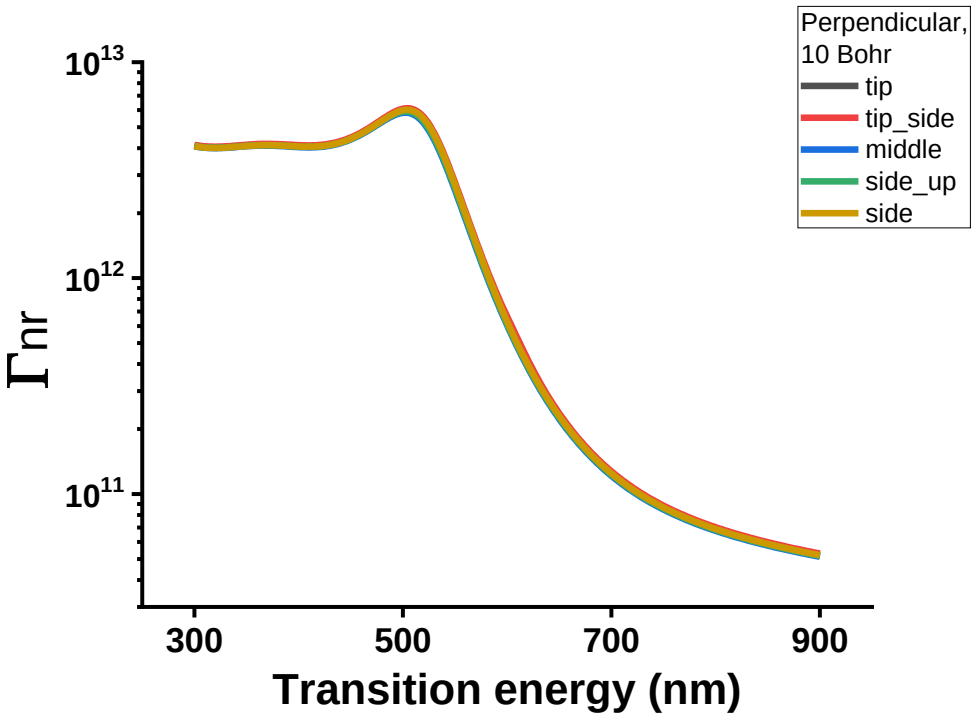

FIGURE 5.11: The effects of various positions on NP 623 over the nonradiative constant of a set of dyes with transitions from 300 nm to 900 nm, perpendicular to the surface, 10 Bohr from the metal.

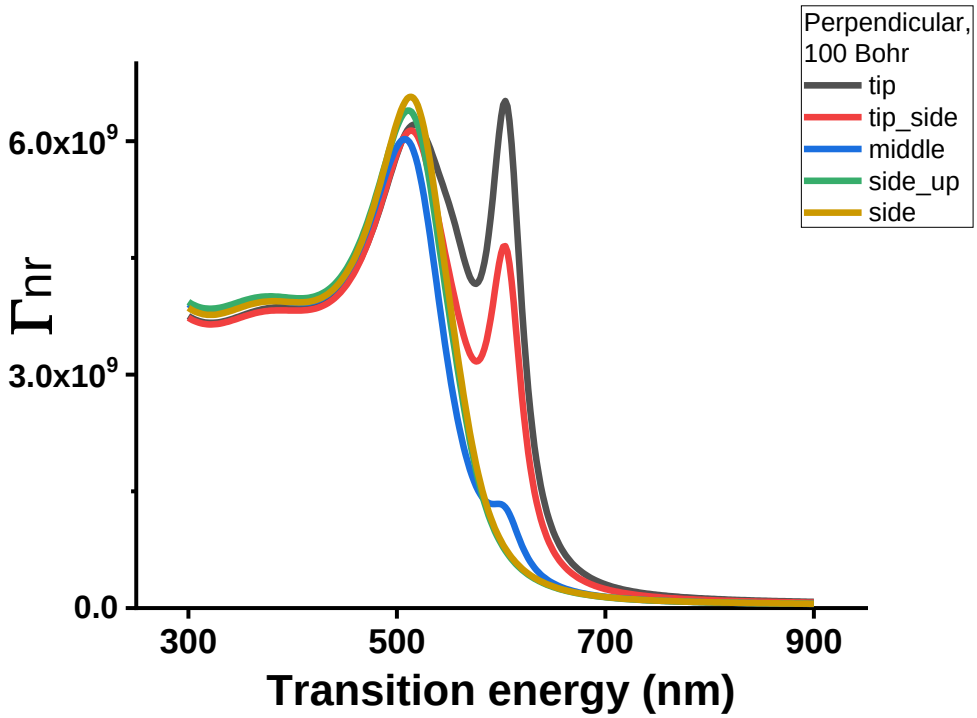

FIGURE 5.12: The effects of various positions on NP 623 over the nonradiative constant of a set of dyes with transitions from 300 nm to 900 nm, perpendicular to the surface, 100 Bohr from the metal.

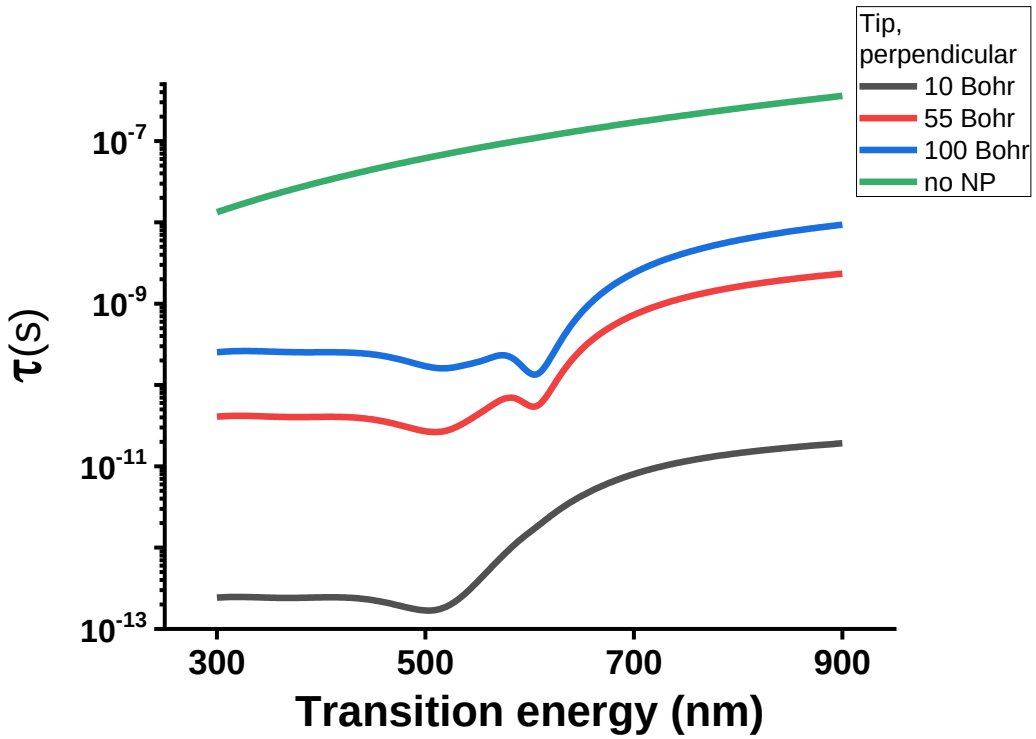

FIGURE 5.13: The effects of the tip of NP 623 over the lifetime of a set of dyes with transitions from 300 nm to 900 nm, perpendicular to the surface, at different distances from the metal.

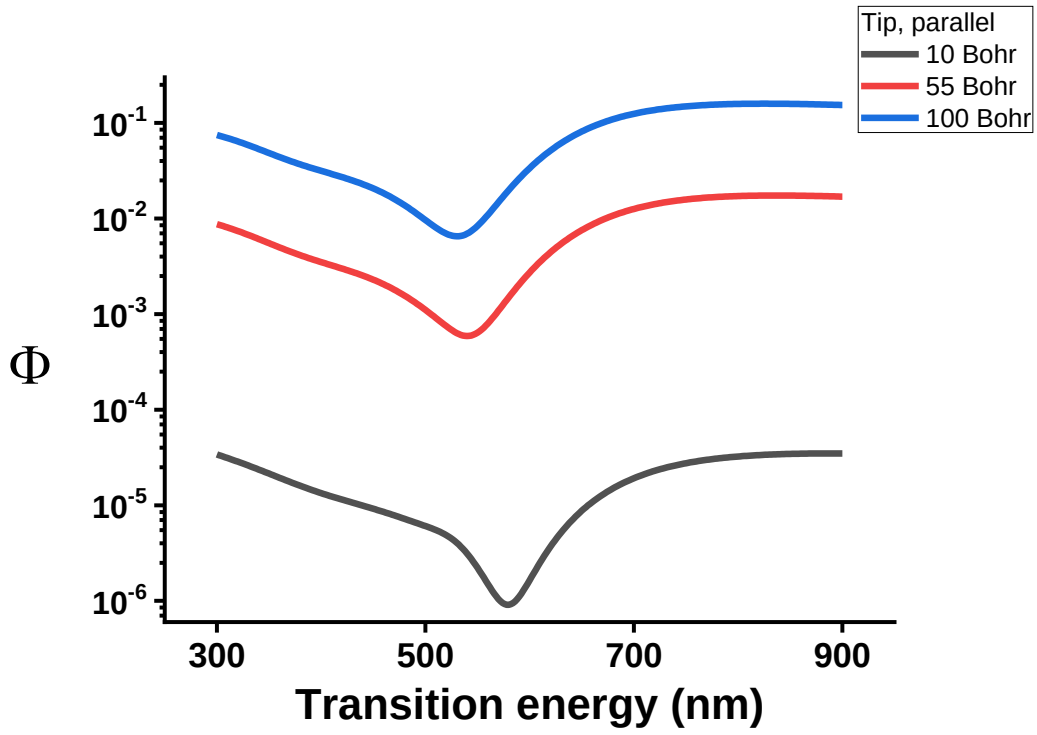

FIGURE 5.14: The effects of the tip of NP 623 over the quantum yield of a set of dyes with transitions from 300 nm to 900 nm, perpendicular to the surface, at different distances from the metal.

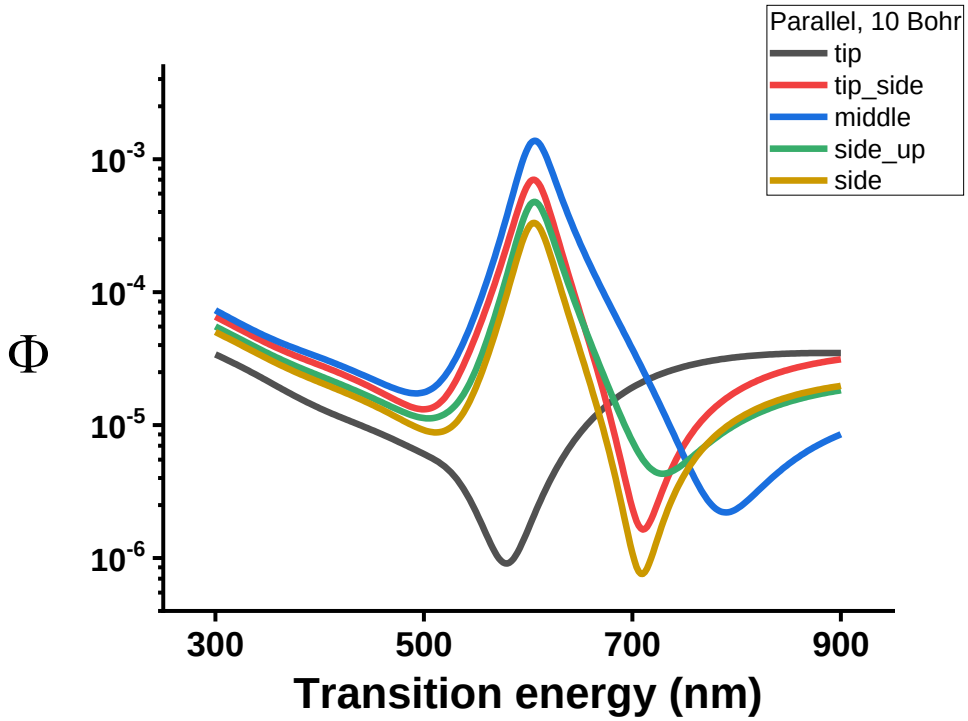

FIGURE 5.15: The effects of NP 623 over the quantum yield of a set of dyes with transitions from 300 nm to 900 nm, at different positions, oriented parallel to the surface, at 10 Bohr from the metal.

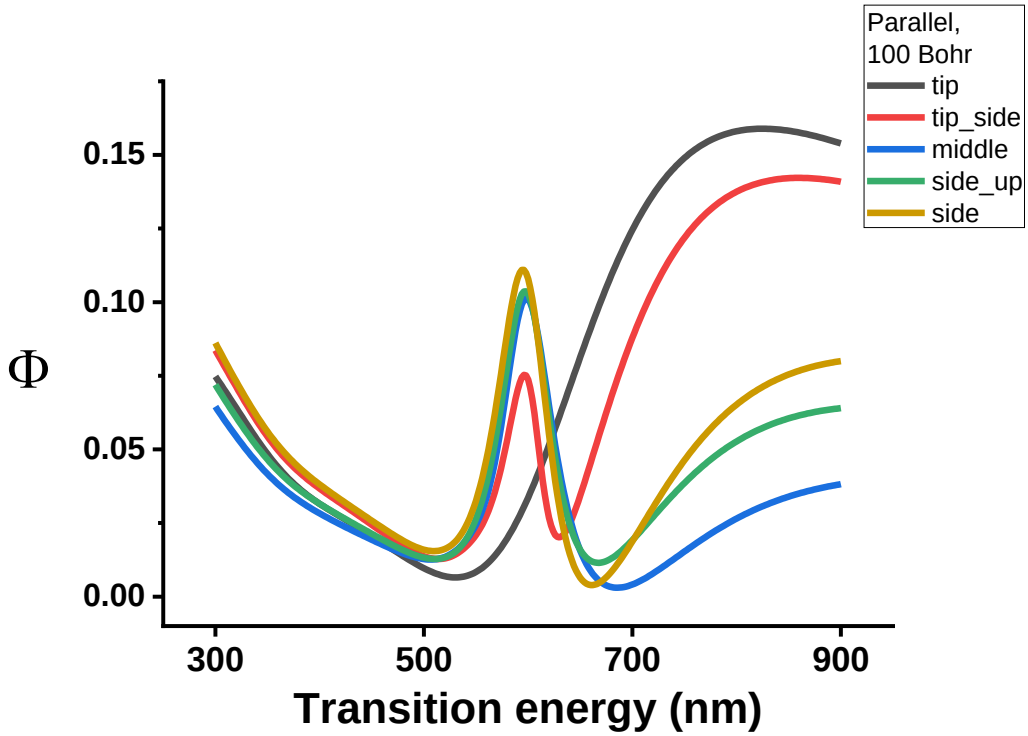

FIGURE 5.16: The effects of NP 623 over the quantum yield of a set of dyes with transitions from 300 nm to 900 nm, at different positions, oriented parallel to the surface, at 100 Bohr from the metal.

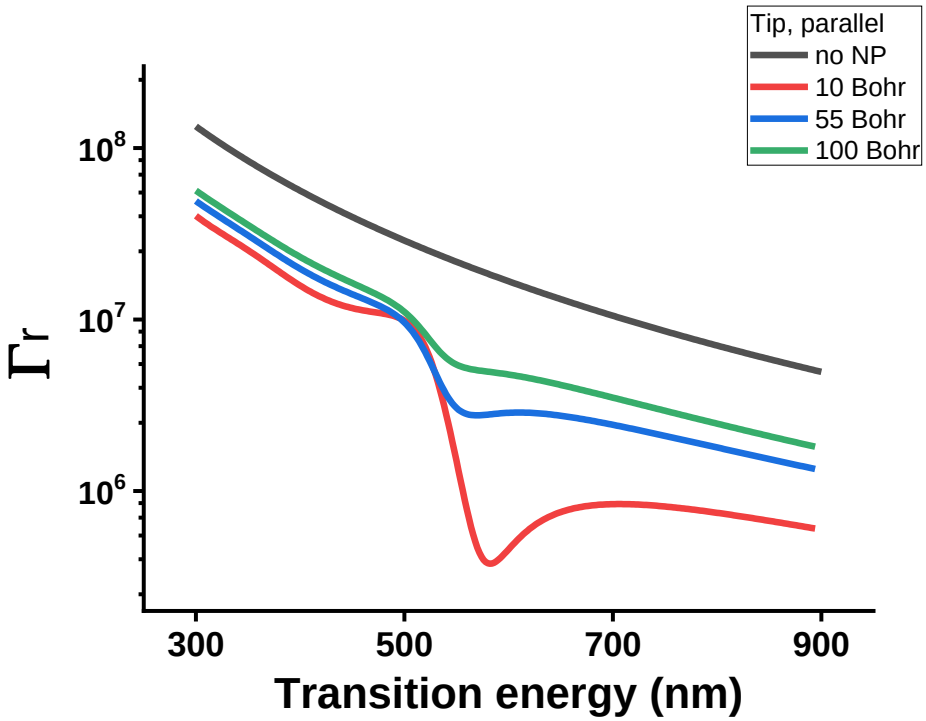

FIGURE 5.17: The effects of the tip of NP 623 over the radiative constant of a set of dyes with transitions from 300 nm to 900 nm, parallel to the surface, at different distances from the metal.

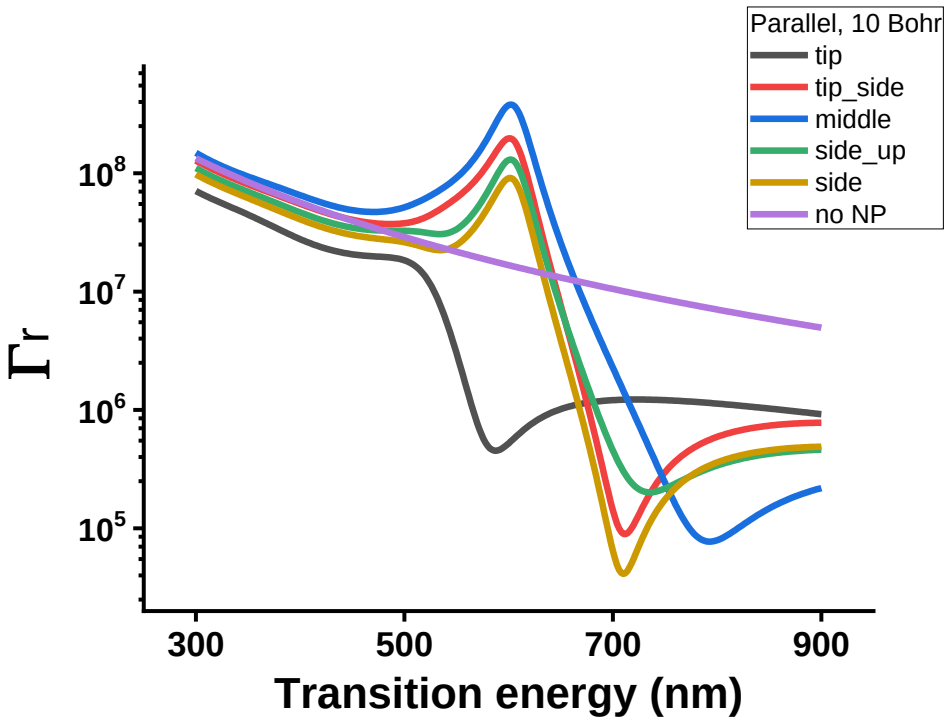

FIGURE 5.18: The effects of various positions on NP 623 over the radiative constant of a set of dyes with transitions from 300 nm to 900 nm, parallel to the surface, 10 Bohr from the metal.

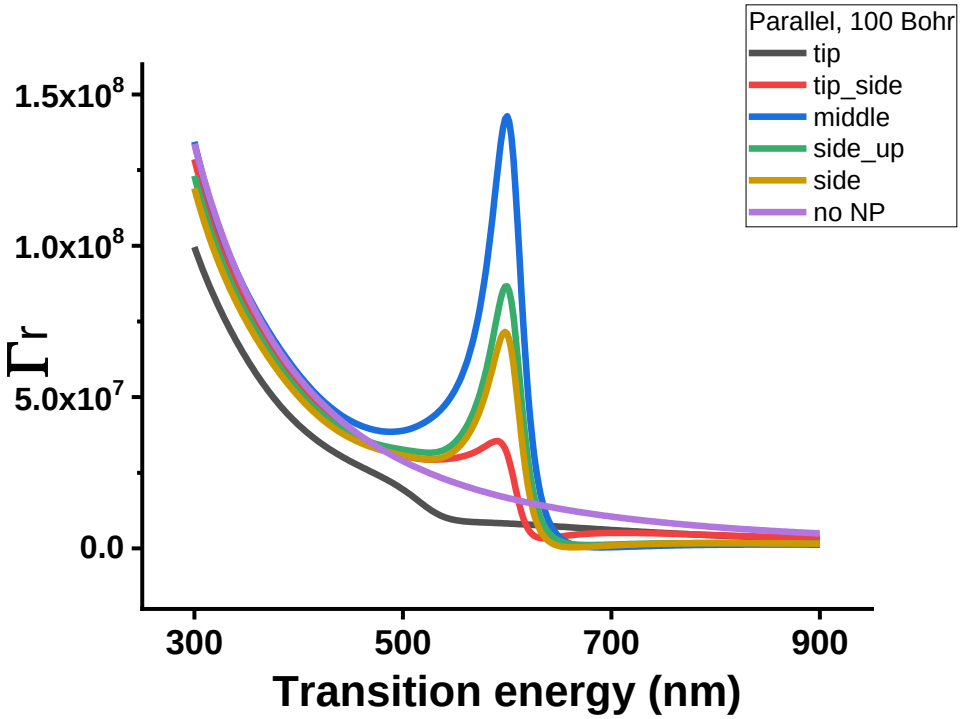

FIGURE 5.19: The effects of various positions on NP 623 over the radiative constant of a set of dyes with transitions from 300 nm to 900 nm, parallel to the surface, 100 Bohr from the metal.

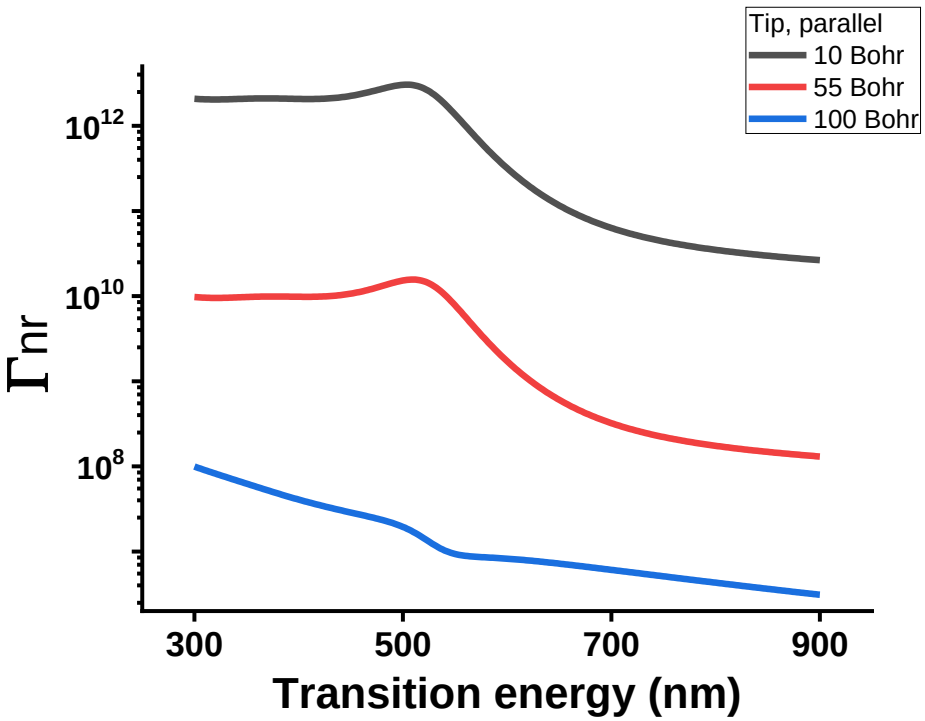

FIGURE 5.20: The effects of the tip of NP 623 over the nonradiative constant of a set of dyes with transitions from 300 nm to 900 nm, parallel to the surface, at different distances from the metal.

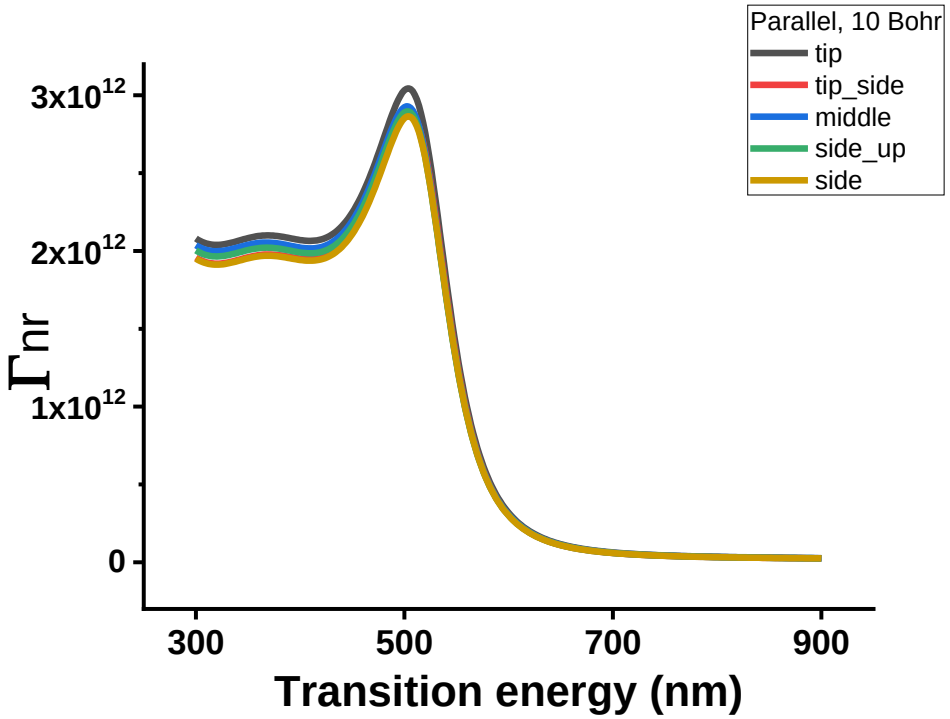

FIGURE 5.21: The effects of various positions on NP 623 over the nonradiative constant of a set of dyes with transitions from 300 nm to 900 nm, parallel to the surface, 10 Bohr from the metal.

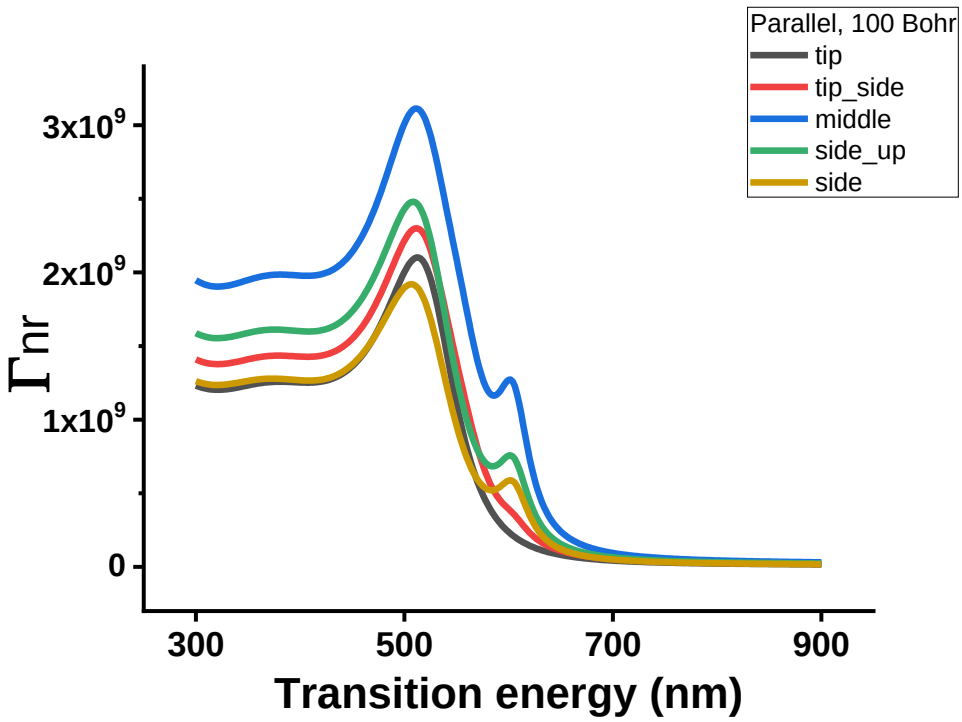

FIGURE 5.22: The effects of various positions on NP 623 over the nonradiative constant of a set of dyes with transitions from 300 nm to 900 nm, parallel to the surface, 100 Bohr from the metal.

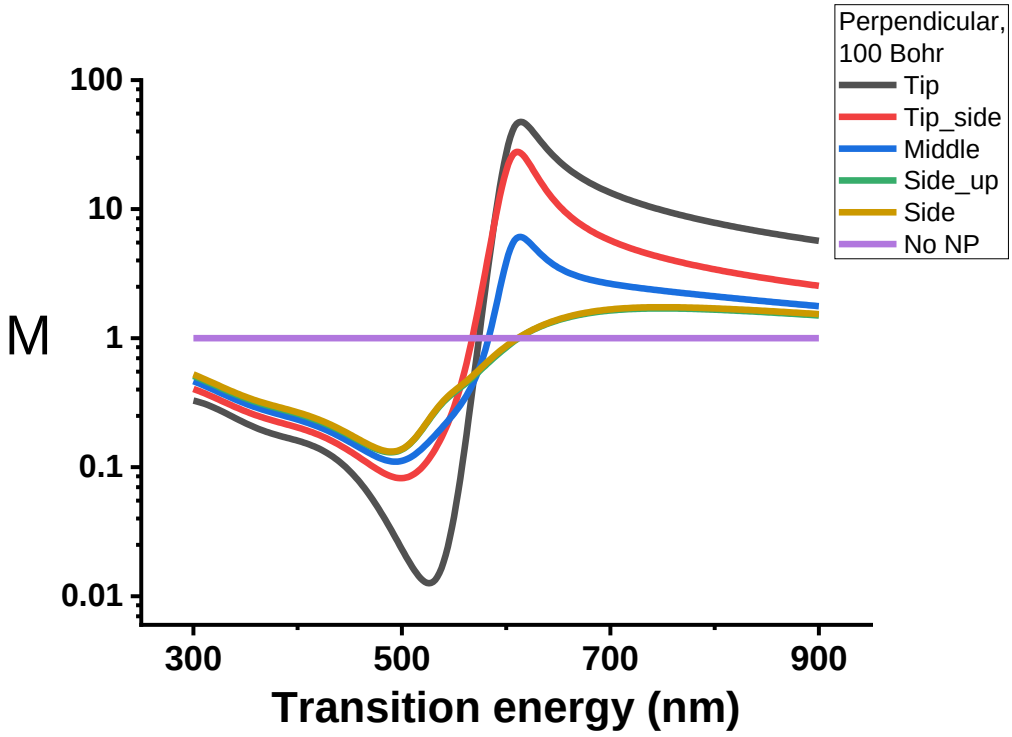

FIGURE 5.23: The effects of various positions on NP 623 over the relative brightness of a set of dyes with transitions from 300 nm to 900 nm, perpendicular to the surface, 100 Bohr from the metal.

this case Φ_{adj} is computed supposing a Φ_{int} of 0.2, which simulates a "not so good" dye, in order to show the strong effects of the presence of he NP. The results show a decrease of the quantum yield in every situation but on the tip at far distance for dyes that emit at wavelengths longer than the LSPR (fig. 5.27. For other positions or orientations the emission quantum yield is quenched with respect the isolated dye, even for a such low initial Φ_{int} (figs. 5.28, 5.29, 5.30). This is to be expected, since the presence of the NP opens a new, fast, decay path for the excited state. What is very curious and important is that for some orientations and positions actually it is possible to even increase the quantum yield of a poor performing dye, not only the effective brightness. As said in the introduction, the ξ with no Stokes shift shows the very same results as the Φ_{adj}.

5.3.3 Stokes shift effects

Real life dyes rarely present the emission at the same wavelength of the absorption, resulting in a Stokes shift that can be quite significant. For this reason we implemented this factor when accounting for the optically relevant parameters, using absorption and emission values at different wavelengths, being the transition energy the absorption wavelength, and summing the Stokes shift in order to have the emission wavelength. The data considering the Stokes shift show a very strong increase of relative brightness (M) for dyes that absorb at energies at the LSPR or lower (or higher wavelengths), when the orientation of the TDM is perpendicular to the surface (figs. 5.34, 5.35), with a quite strong increase of the effect for higher Stokes shifts.

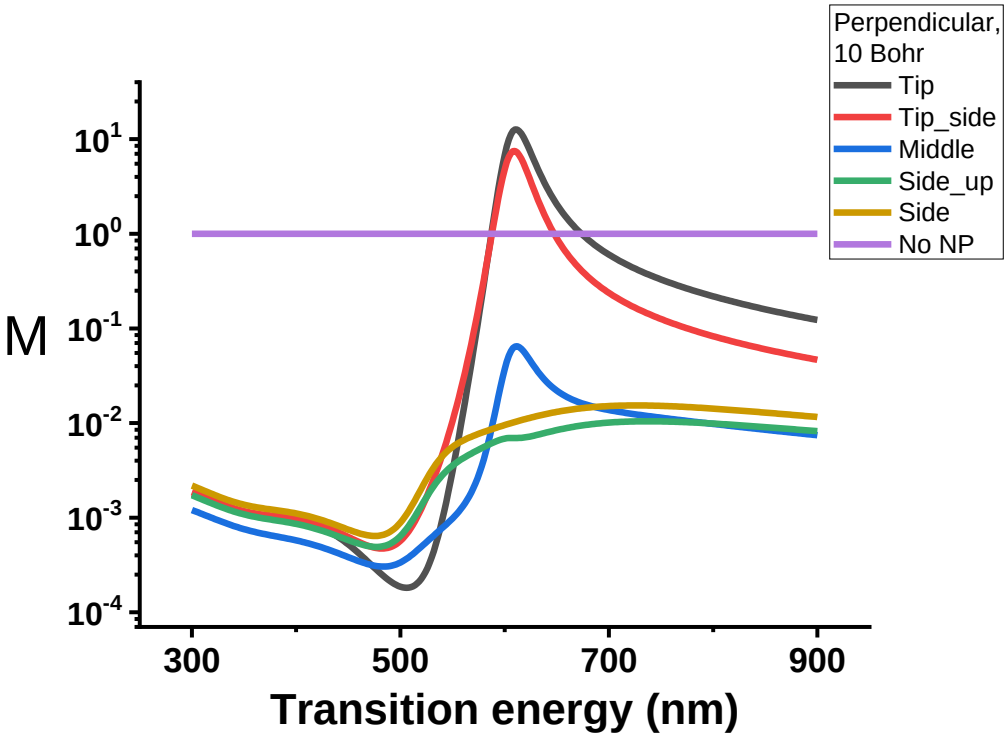

FIGURE 5.24: The effects of various positions on NP 623 over the relative brightness of a set of dyes with transitions from 300 nm to 900 nm, perpendicular to the surface, 10 Bohr from the metal.

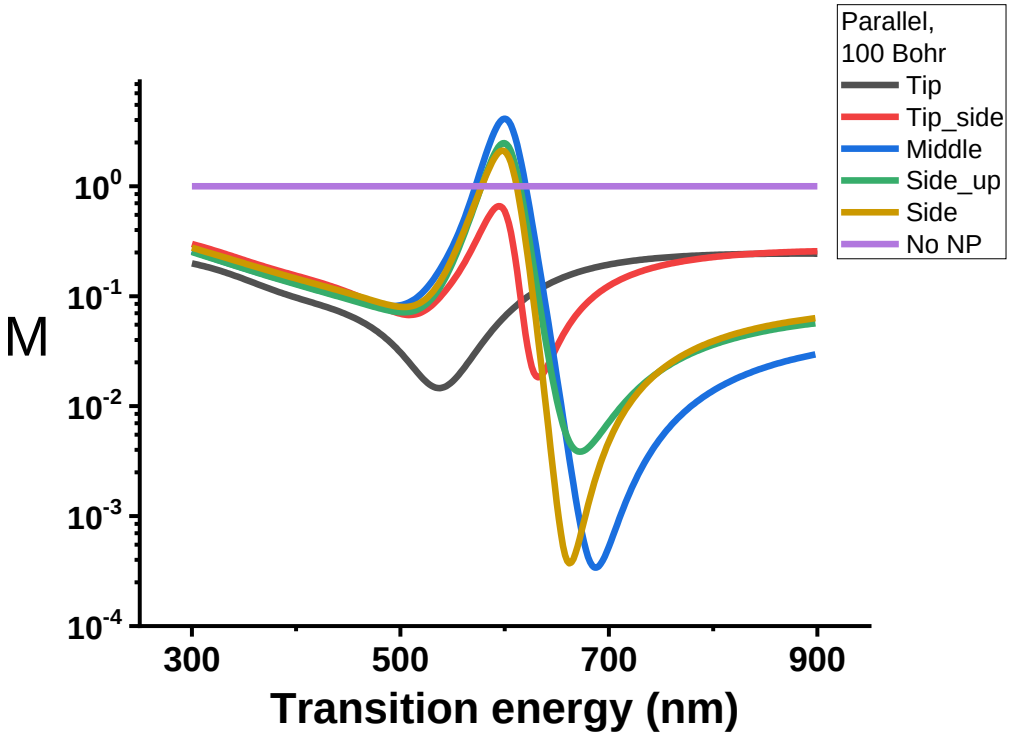

FIGURE 5.25: The effects of various positions on NP 623 over the relative brightness of a set of dyes with transitions from 300 nm to 900 nm, parallel to the surface, 100 Bohr from the metal.

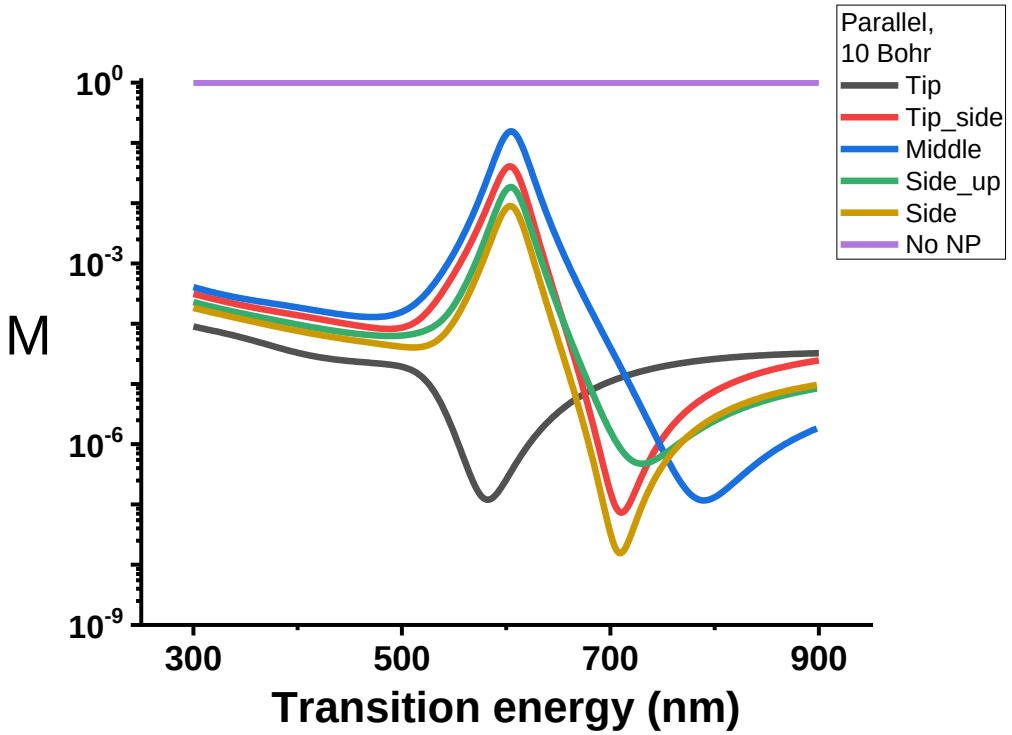

FIGURE 5.26: The effects of various positions on NP 623 over the relative brightness of a set of dyes with transitions from 300 nm to 900 nm, parallel to the surface, 10 Bohr from the metal.

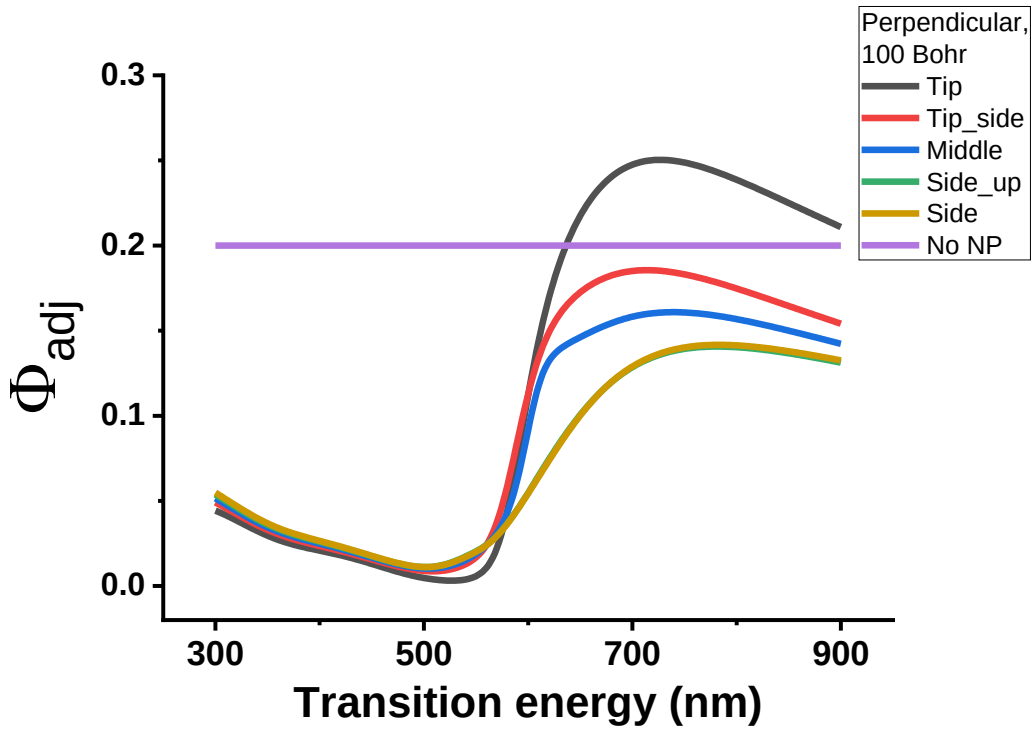

FIGURE 5.27: The effects of various positions on NP 623 over the adjusted quantum yield of a set of dyes with transitions from 300 nm to 900 nm, perpendicular to the surface, 100 Bohr from the metal.

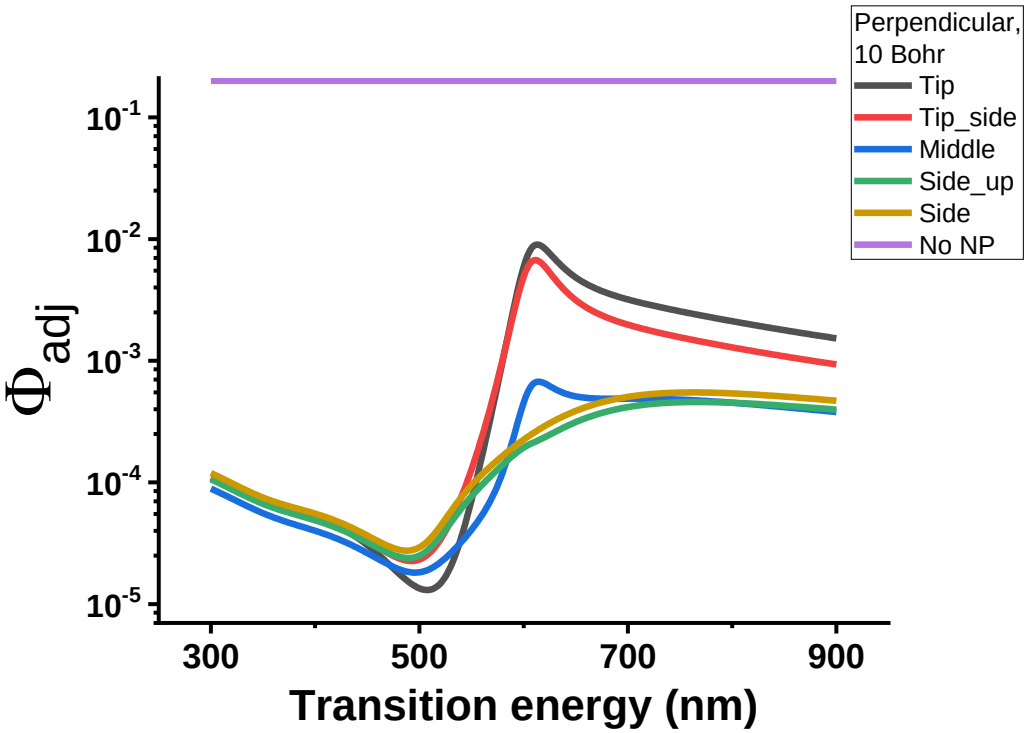

FIGURE 5.28: The effects of various positions on NP 623 over the adjusted quantum yield of a set of dyes with transitions from 300 nm to 900 nm, perpendicular to the surface, 10 Bohr from the metal.

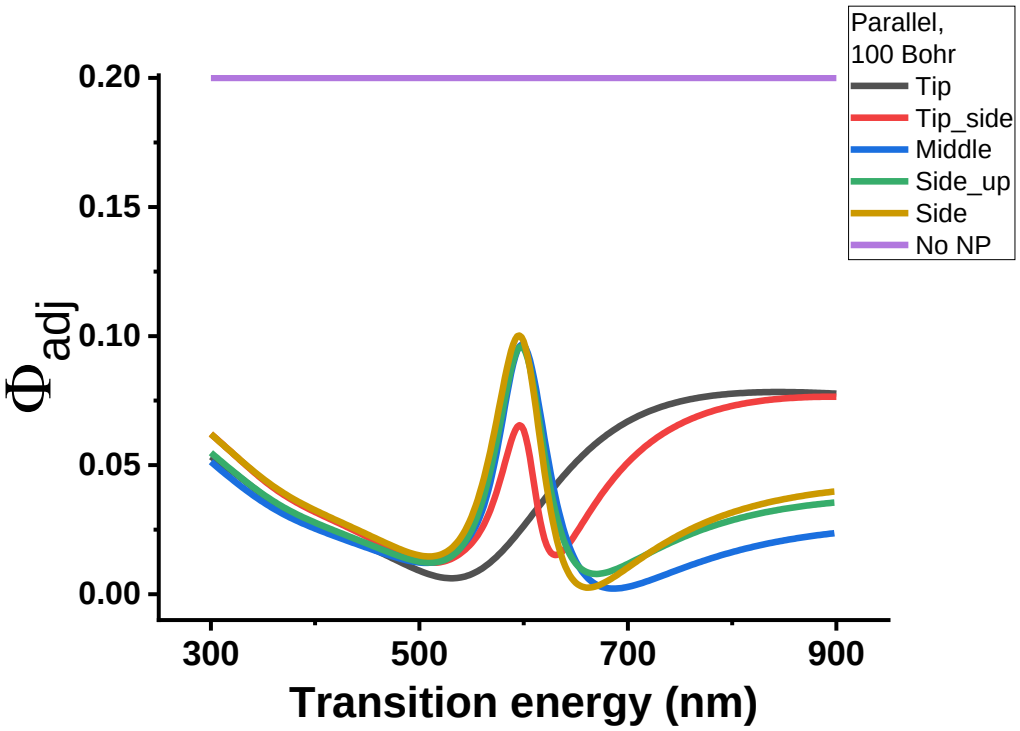

FIGURE 5.29: The effects of various positions on NP 623 over the adjusted quantum yield of a set of dyes with transitions from 300 nm to 900 nm, parallel to the surface, 100 Bohr from the metal.

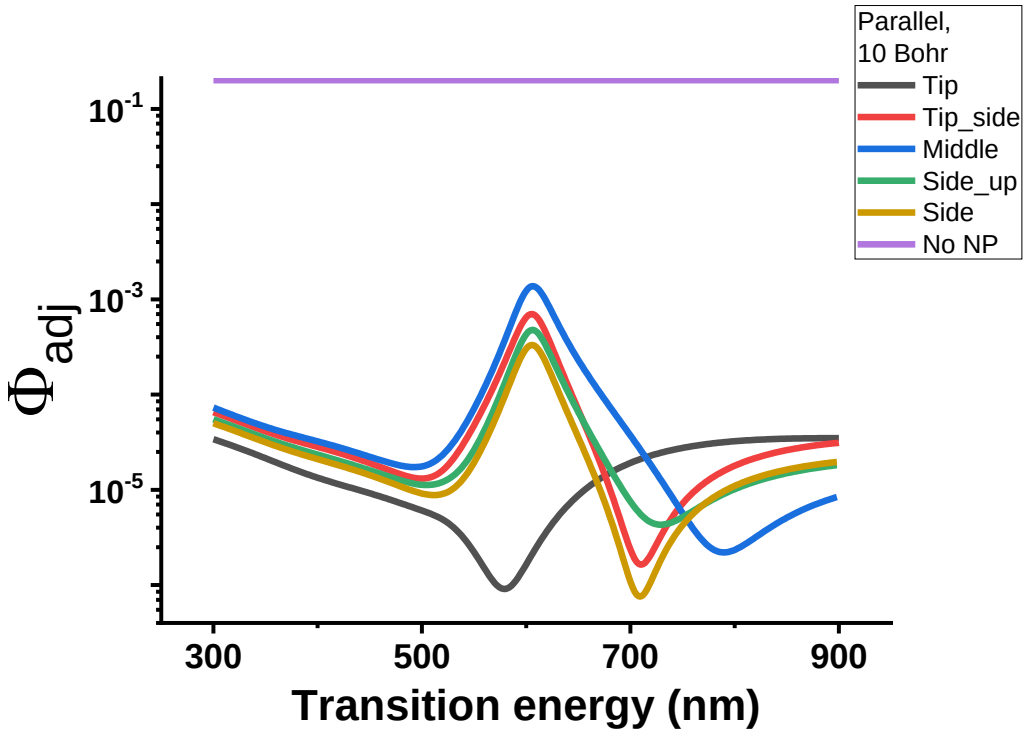

FIGURE 5.30: The effects of various positions on NP 623 over the adjusted quantum yield of a set of dyes with transitions from 300 nm to 900 nm, parallel to the surface, 10 Bohr from the metal.

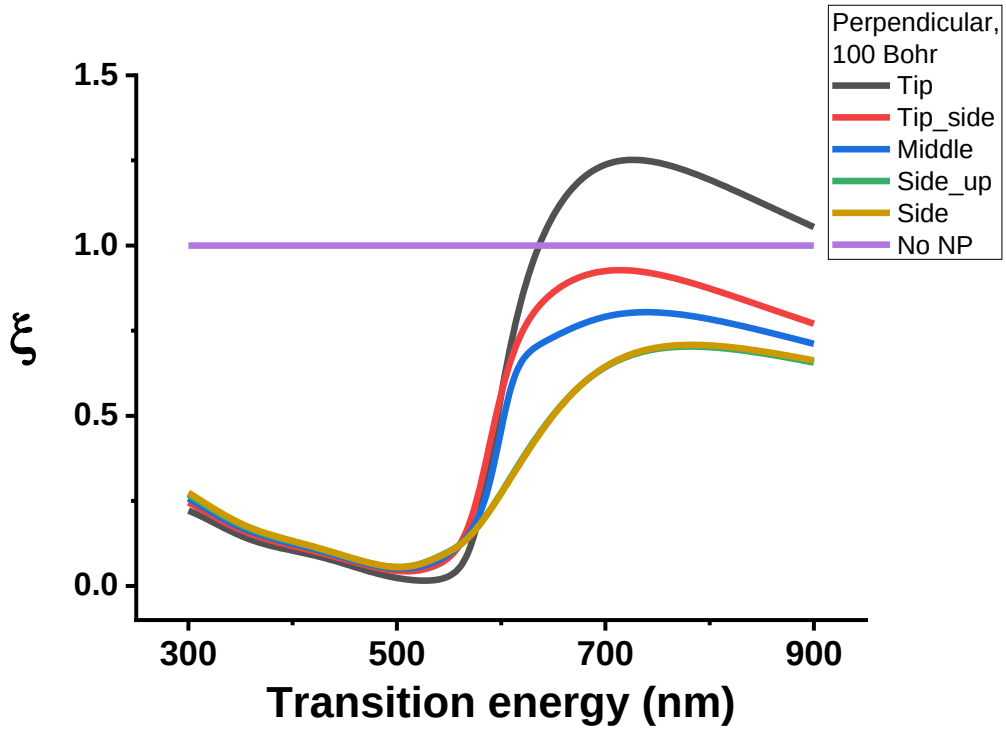

FIGURE 5.31: The effects of various positions on NP 623 over the relative excited states population of dyes with transitions from 300 nm to 900 nm, perpendicular to the surface, 100 Bohr from the metal.

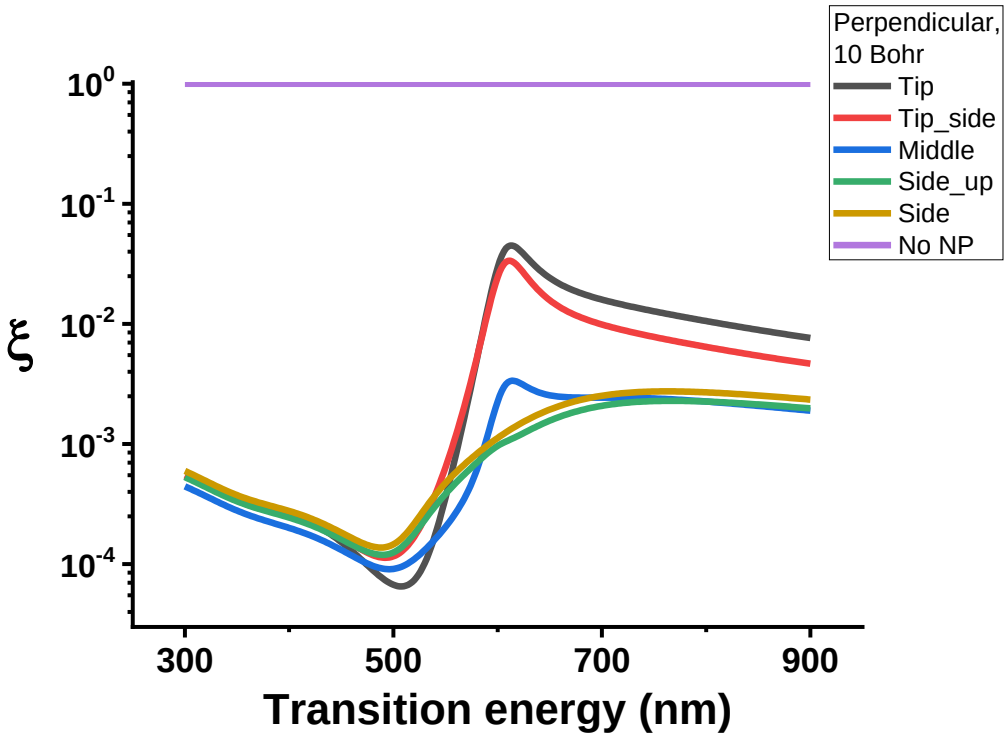

FIGURE 5.32: The effects of various positions on NP 623 over the relative excited states population of dyes with transitions from 300 nm to 900 nm, perpendicular to the surface, 100 Bohr from the metal.

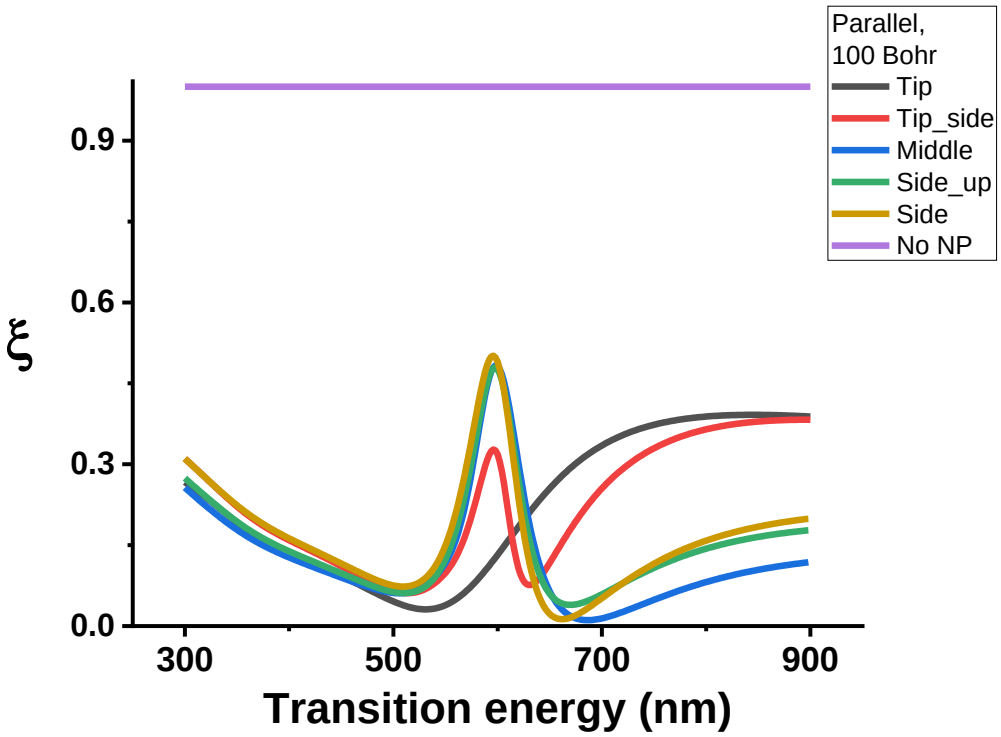

FIGURE 5.33: The effects of various positions on NP 623 over the relative excited states population of a set of dyes with transitions from 300 nm to 900 nm, parallel to the surface, 100 Bohr from the metal.

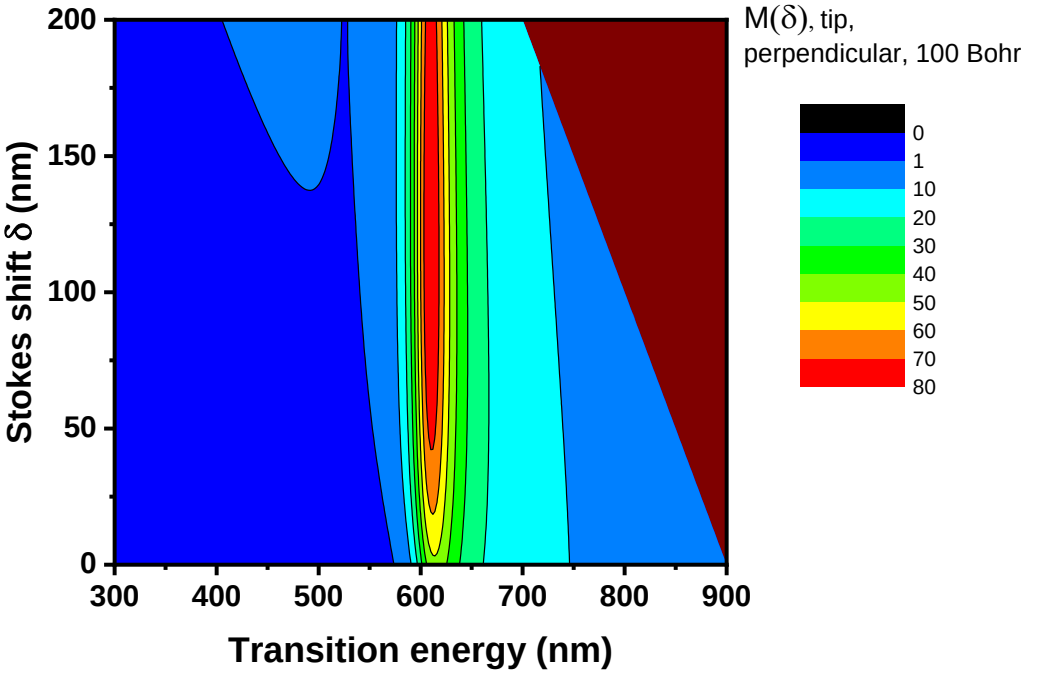

FIGURE 5.34: The effects of the tip of NP 623 over the relative brightness of dyes with transitions from 300 nm to 900 nm, Stoke shift up to 200 nm, perpendicular to the surface, at 100 Bohr from the metal.

Considering that a null effect from the NP results in $M(\delta) = 1$, the enhancement can be very strong, at tip position, reaching almost two orders of magnitude increase in luminance. On the side position albeit much smaller, the effect is still positive over the emitting electromagnetic field, when the dye emits at wavelengths higher than the LSPR value. Another interesting parameter, that accounts collectively for the effects of the NP over the quantum yield and the increase in available light due to field enhancement, is the excited states relative population Ξ. In fig. 5.36 it is shown the excited states relative population for dyes located at the tip for certain absorption peaks and various possible Stokes shifts. The result shows that the increase can be quite large (up to 12 times) for dyes that absorb at the LSPR and increasingly higher to stronger Stokes shifts. Figs. 5.37 and 5.38 show that for other orientations or positions this increase is not present. This means that at some positions, although presenting an overall quenched quantum yield, the emission process is not quenched indeed, thanks to the higher intensity of the exciting field due to the presence of the NP.

5.3.4 Absorption

Absorption data gives very similar results compared to emission. This is not surprising, considering that the main differences between the Γ_r and the absorption rate are a constant multiplicative factor and the dependence of the of the emission rate over the energy by ω^3, (from which the absorption is independent), while for the

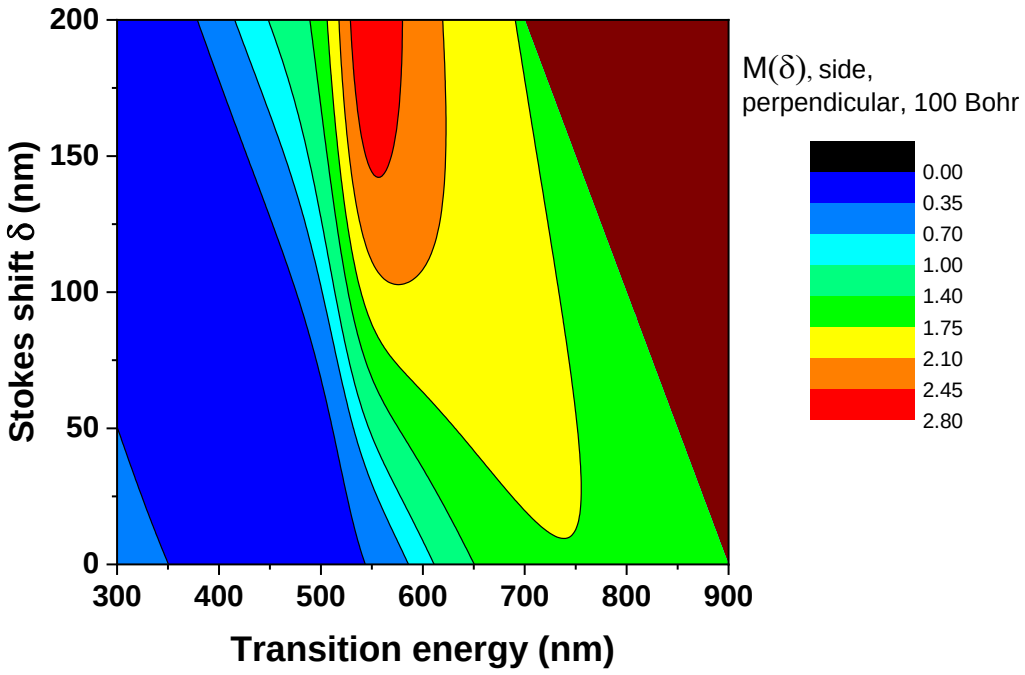

FIGURE 5.35: The effects of the side of NP 623 over the relative brightness of dyes with transitions from 300 nm to 900 nm, Stoke shift up to 200 nm, perpendicular to the surface.

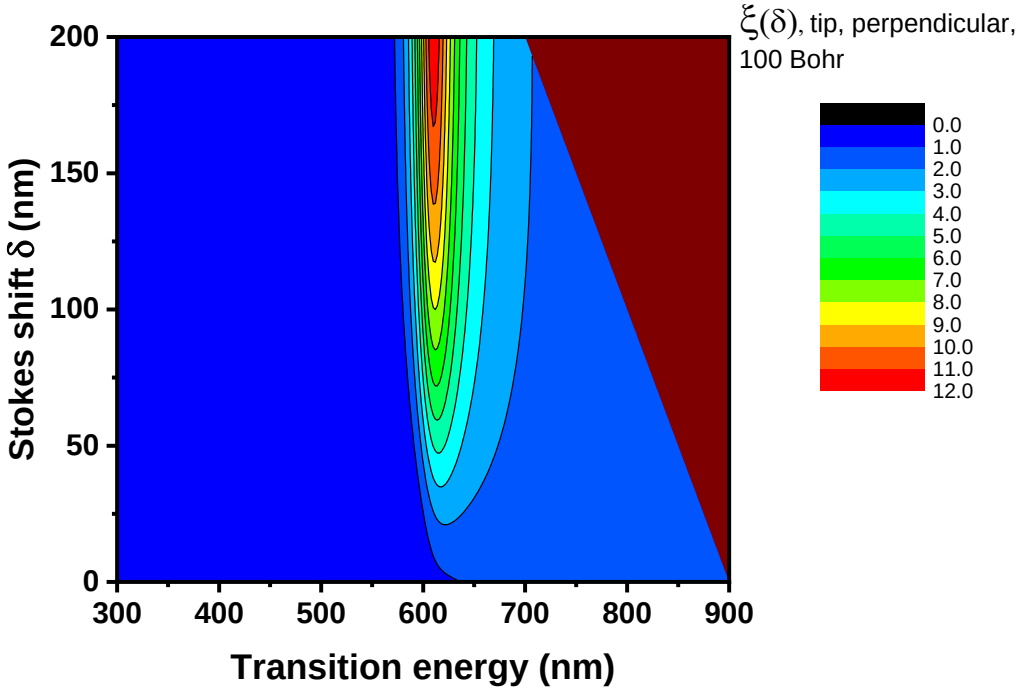

FIGURE 5.36: The effects of the tip of NP 623 over the relative excited states population of dyes with transitions from 300 nm to 900 nm, Stoke shift up to 200 nm.

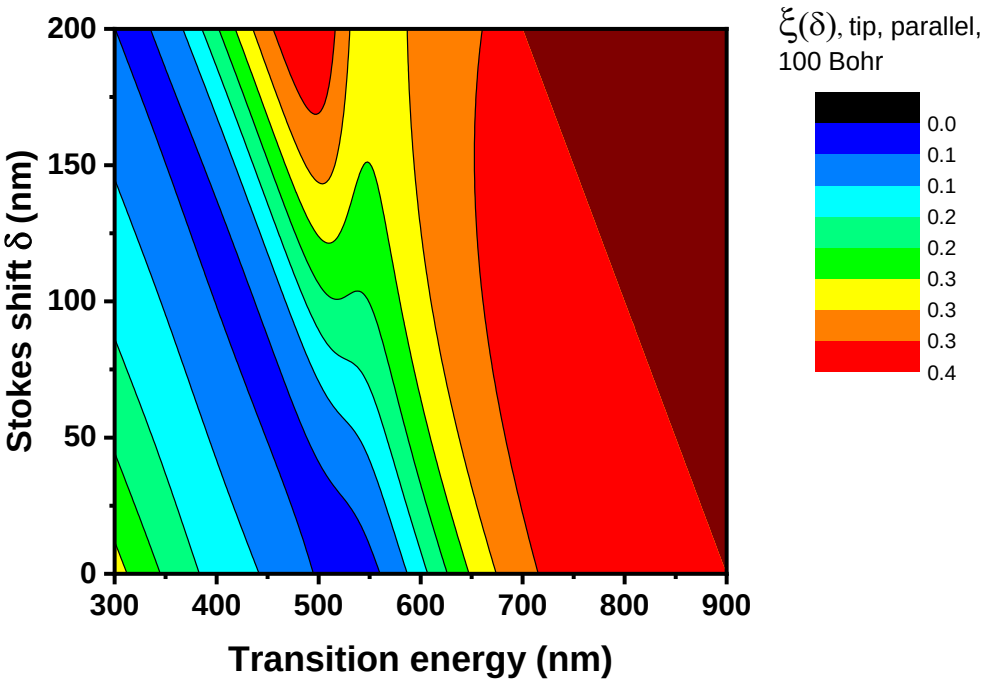

FIGURE 5.37: The effects of the tip of NP 623 over the relative excited states population of dyes with transitions from 300 nm to 900 nm, Stoke shift up to 200 nm.

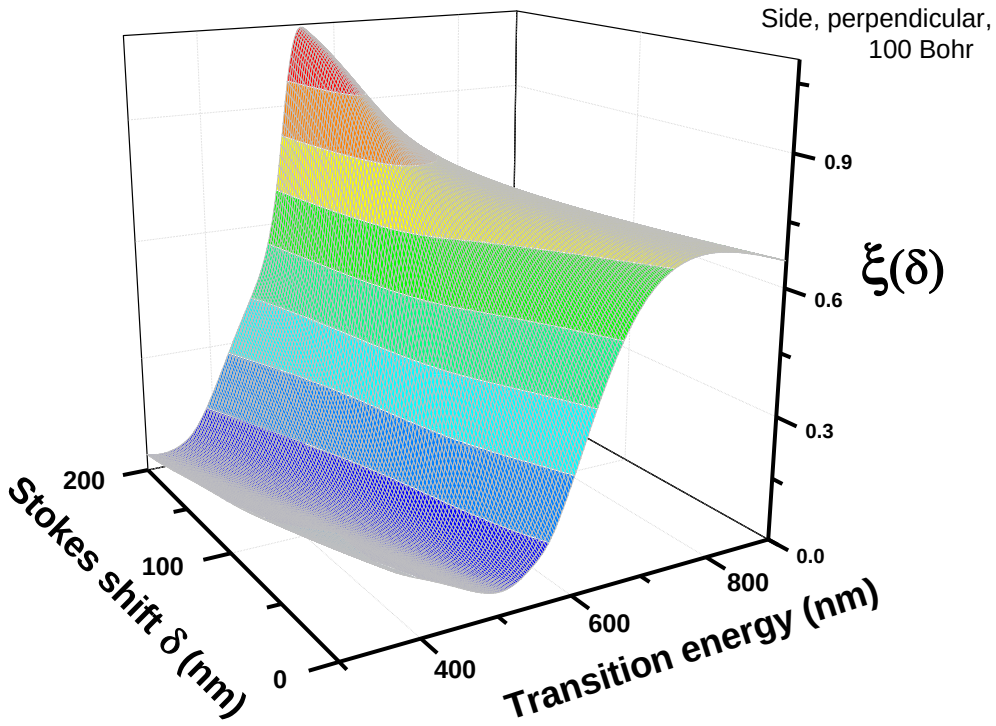

FIGURE 5.38: The effects of the side of NP 623 over the relative excited states population of dyes with transitions from 300 nm to 900 nm, Stoke shift up to 200 nm.

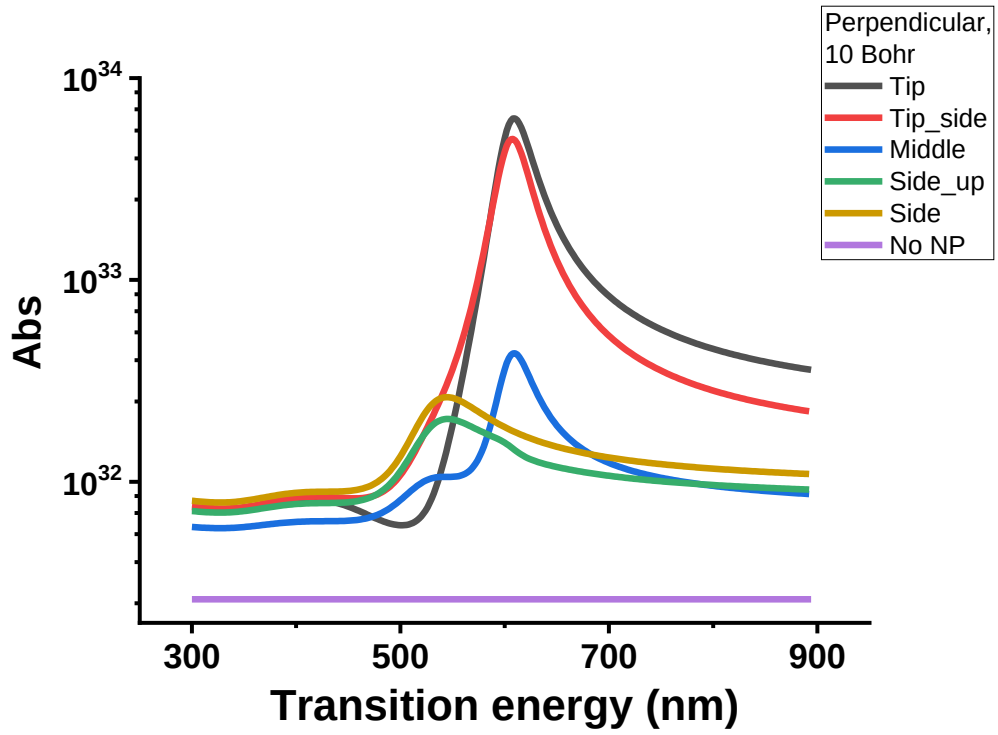

FIGURE 5.39: The effects of various positions on NP 623 over the absorption rates of a set of dyes with transitions from 300 nm to 900 nm, perpendicular to the surface, 10 Bohr from the metal.

rest the behaviour is given by the $\vec{\mu}^{tot}$, which, within the approximation adopted, defines the behaviour of the optical properties of the molecules. Absorption data show very similar behaviours compared to the emission: a general strong enhancement, in some cases up to two order of magnitude, arises when the dye absorbs at the LSPR frequency, resonating with the excitation of the plasmonic cloud. It is also evident the presence of some cold spots, due to a misalignment of the phases of the oscillating TDM of the molecule and the NP, especially when near the surface, where the enhancement effect is proved to be lower, and when the orientation of the dye is such that the coupling with the LSPR is minimized. While this parameter in principle addresses the effects of the presence of the nanoparticles over the absorption of the molecule, one could argue that the main part of the absorption is carried by the NP itself, which has a much greater oscillator strength than not only the single chromophores, but also the layer composed of dye and surfactant as a whole. So the absorption can be computed considering the organic layer as a perturbation of the NP's spectrum rather than as an actor itself, which is the approach adopted in Chapter 6. On the other side, it makes sense to compute emissions starting from the dyes, since the NP has no emission at all, but a strong influence over the chromophores' ones through its electric field.

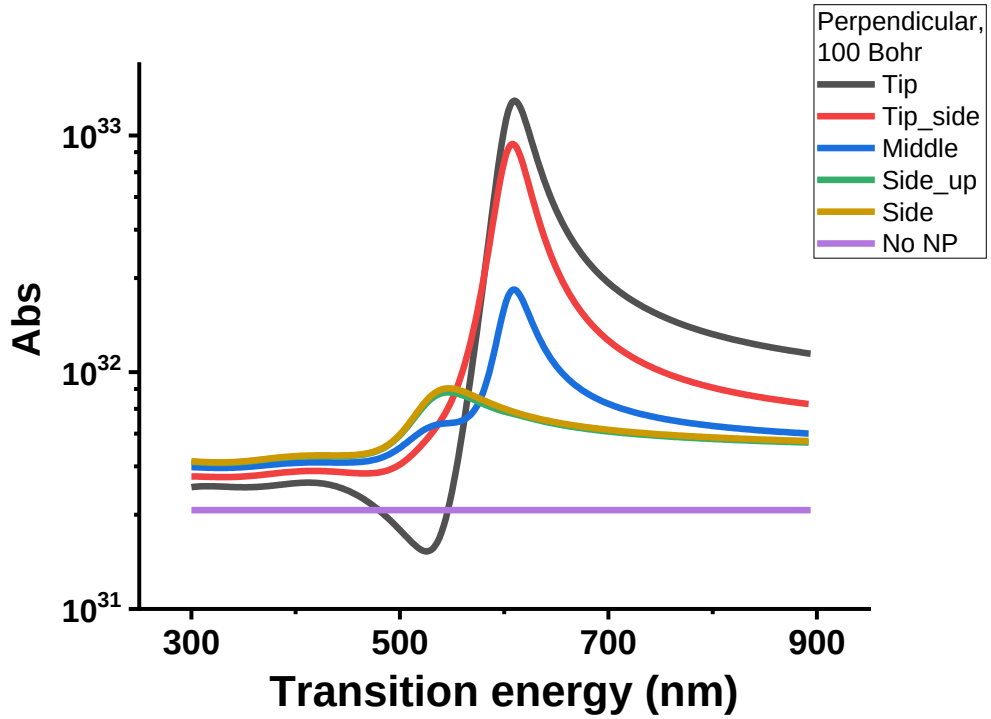

FIGURE 5.40: The effects of various positions on NP 623 over the absorption rates of a set of dyes with transitions from 300 nm to 900 nm, perpendicular to the surface, 100 Bohr from the metal.

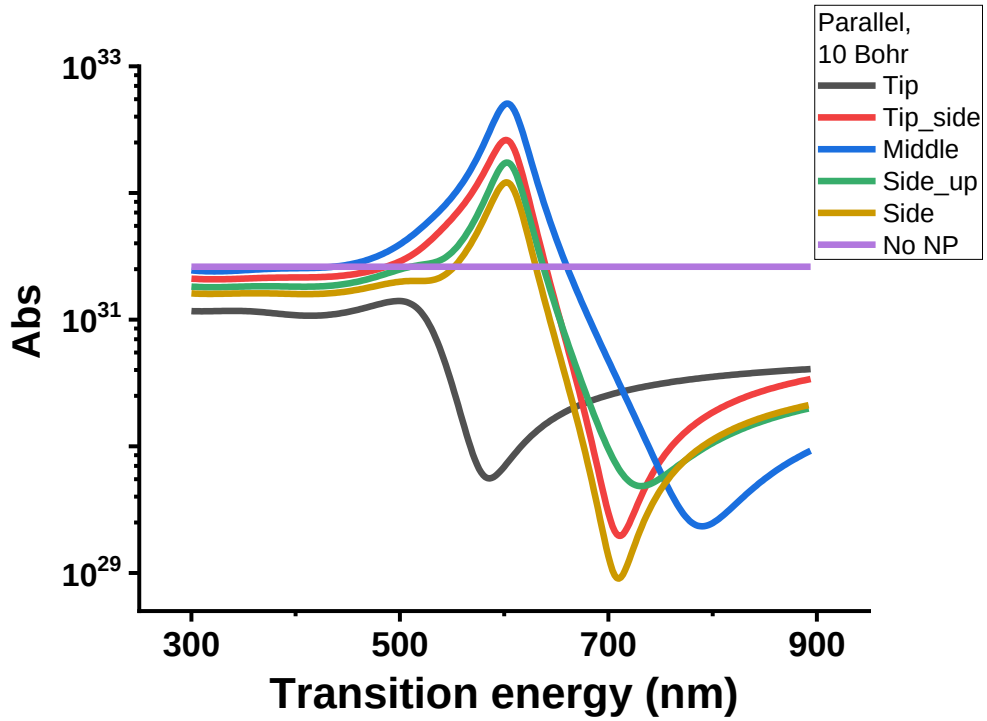

FIGURE 5.41: The effects of various positions on NP 623 over the absorption rates of a set of dyes with transitions from 300 nm to 900 nm, parallel to the surface, 10 Bohr from the metal.

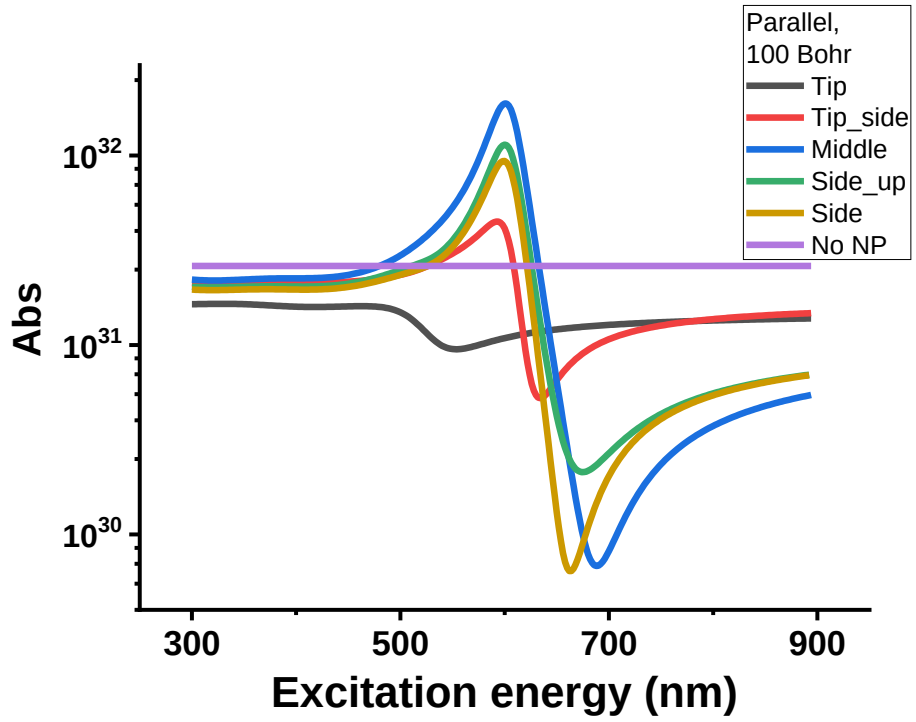

FIGURE 5.42: The effects of various positions on NP 623 over the absorption rates of a set of dyes with transitions from 300 nm to 900 nm, parallel to the surface, 100 Bohr from the metal.

5.4 Results for NP 775

5.4.1 Emission

The same simulations have been performed also for the NP with LSPR at 775 nm (though the peak is at 723 nm using quasi-static simulations). In figs. 5.43, 5.44, 5.45, 5.46 are presented the quantum yields for dyes at different transition energies at tip and side positions, at different distances from the metal. As expected, the further the dye is from the surface, the most efficient is the emission process. At tip position, if the TDM of the dye is oriented perpendicular to the surface, the maximum yield comes around the LSPR energy, with a narrow margin when very near, and a wider tolerance, combined with a red shift, when the dye is put farther away. If the dye's TDM is oriented parallel to the surface the quantum yield is much lower when near the surface, but surprisingly has a strong increase when the distance is 100 Bohr, a result much higher compared to the case of the previous NP. When the dye is situated on the side, the quantum yield is lower than at tip position if oriented parallel to the surface, and behaving very similarly, with an addition of a bump that comes from an increase in the radiative constant Γ_r at around 550 nm (see fig. 5.50). This is due to an additional plasmonic resonance, much weaker than the main one, that can be seen as a small contributor in the NP's absorption in fig. 5.2. This is most due to a higher order excitation of the electron plasma, most likely the quadrupole. If the dye is perpendicular to the surface, though, the maximum quantum yield is higher with respect to the tip, but for a smaller window of possible transition energies, and

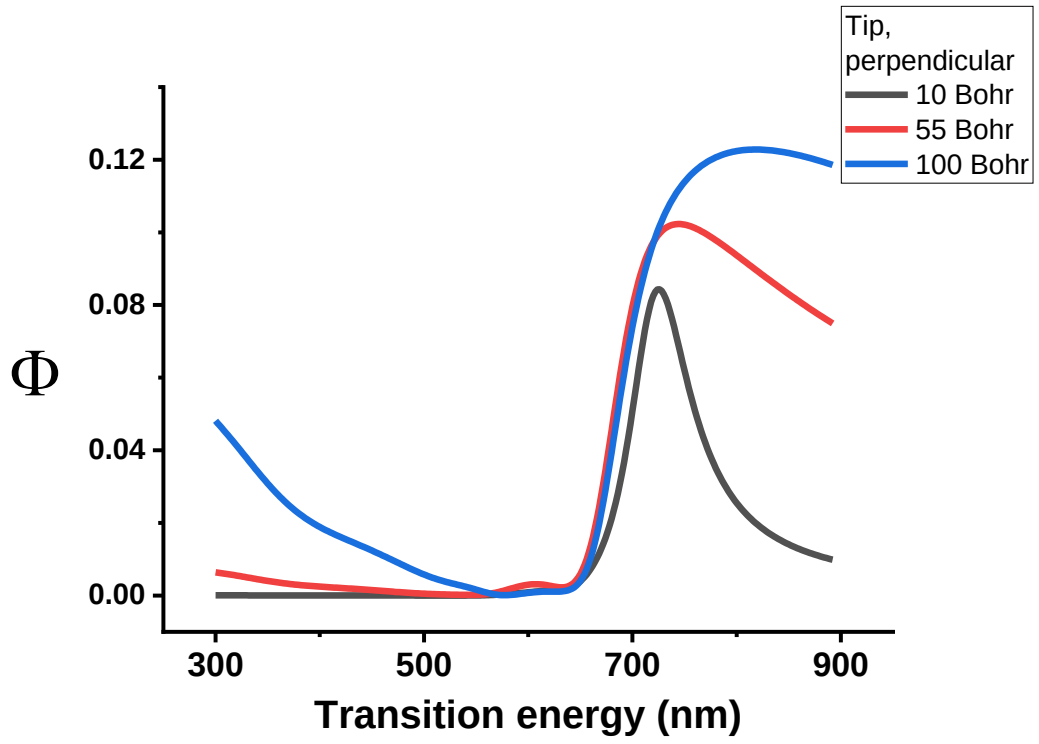

FIGURE 5.43: The effects of the tip of NP 775 over the quantum yield of a set of dyes with transitions from 300 nm to 900 nm, oriented perpendicular to the surface, at different distances from the metal.

quenches more substantially when getting nearer to the surface. These behaviours are caused by the competing processes given by Γ_r and Γ_{nr}. In fig. 5.47 is very clear the presence of a few cold spots for energies lower than LSPR, while the enhancement of the radiative decay process is very strong when the dyes emit at around the LSPR. On the contrary, in fig. 5.48 is evident that the decay process is always slowed down if the dye is orthogonal to the LSPR. Figs. 5.49 and 5.50 show that at side position the dye couple respectively with the primary and secondary resonance, with no strong effect due to the distance, when perpendicular to the surface. For the nonradiatve decay constants, the behaviour is quite straightforward: the nearer to the surface the faster is the decay process. A few bumps are observed, especially in fig. 5.52 where Γ_{nr} shows some peaks for values at around 723 nm (primary LSPR), 650 nm, and 550 nm. The first two peaks are present respectively in fig. 5.53 and 5.54 as well. Figs. 5.55 and 5.56 show the lifetimes of the excited states, which are always lower than the dyes in absence of the NP.

5.4.2 Quantifying the enhancement performance

Looking at fig. 5.57 it is immediately evident that, for the NP with LSPR at 775 nm, there is a strong presence of cold spots at energies higher than the LSPR. Either at tip and side positions the value of the relative brightness M is lower than 1 when the dye emits at wavelengths lower than 650 nm, while it is enhanced for lower energies, especially when the dye's TDM is perpendicular to the surface and it is positioned at the tip. In any case, a dye far from the tip and near the surface results to be

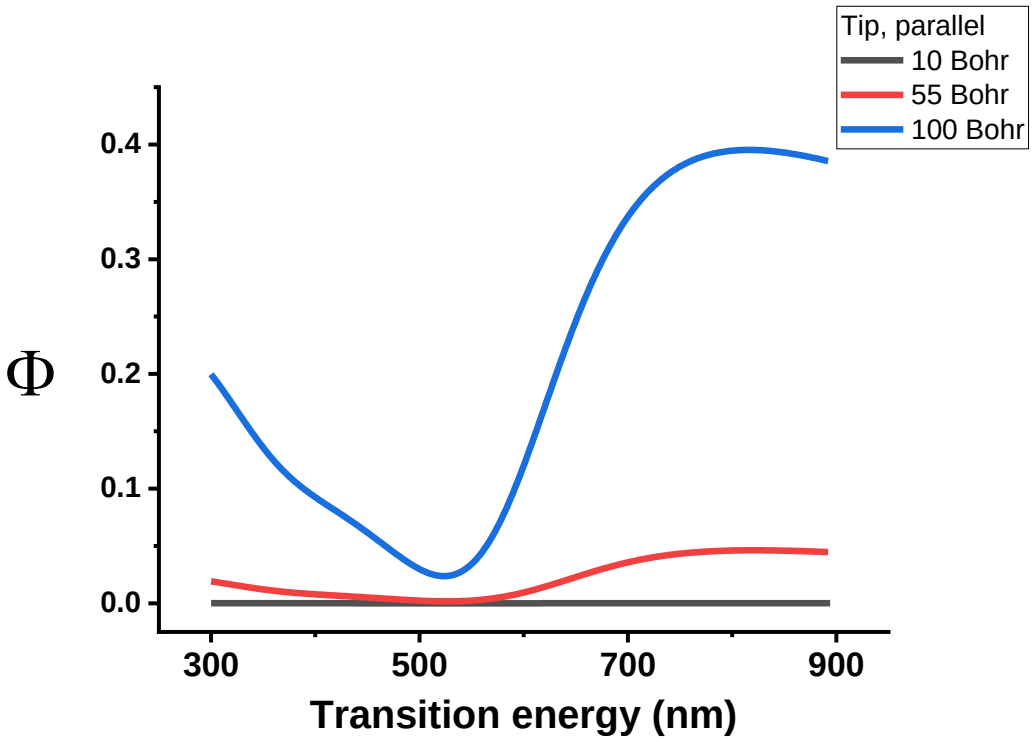

FIGURE 5.44: The effects of the tip of NP 775 over the quantum yield of a set of dyes with transitions from 300 nm to 900 nm, oriented parallel to the surface, at different distances from the metal.

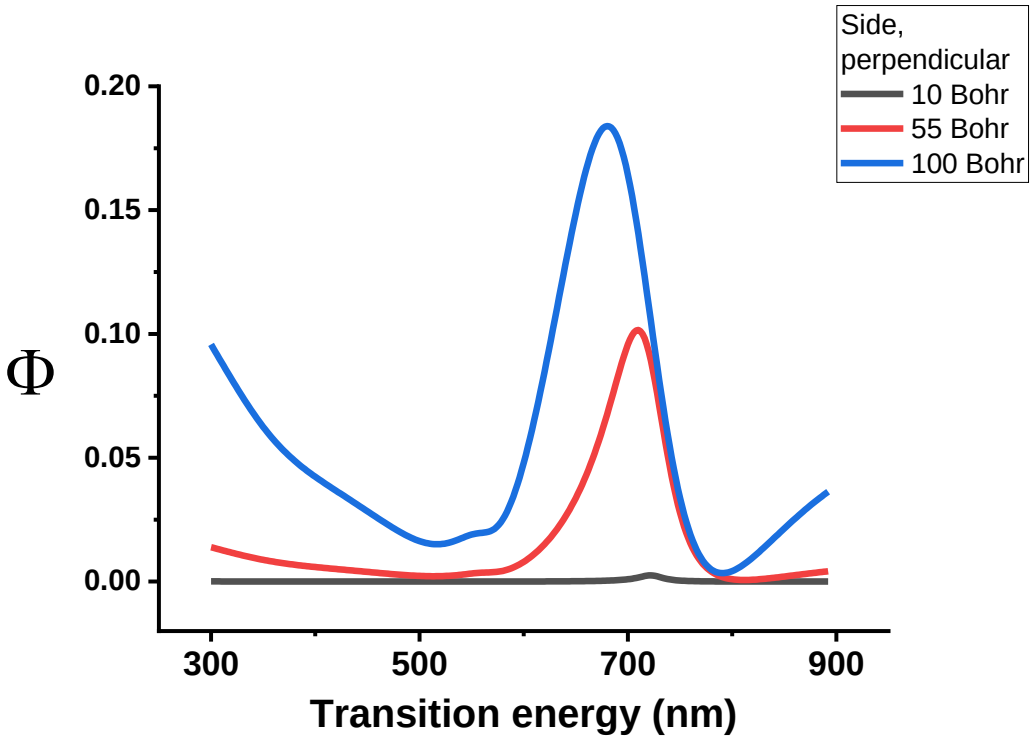

FIGURE 5.45: The effects of the side of NP 775 over the quantum yield of a set of dyes with transitions from 300 nm to 900 nm, oriented perpendicular to the surface, at different distances from the metal.

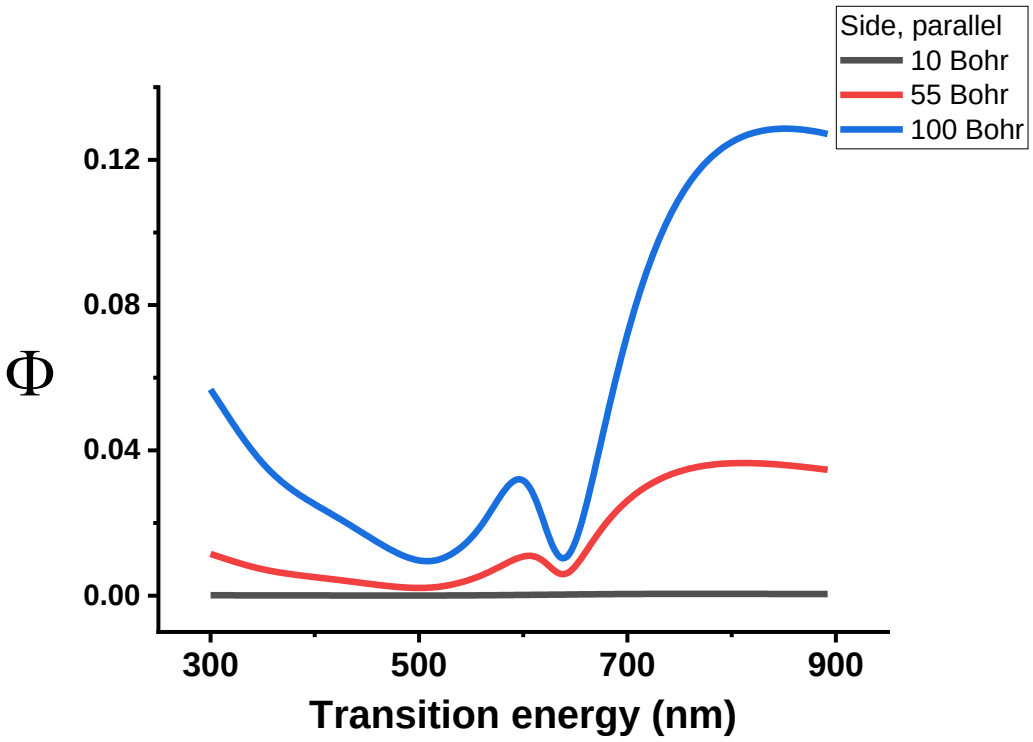

FIGURE 5.46: The effects of the tip of NP 775 over the quantum yield of a set of dyes with transitions from 300 nm to 900 nm, oriented parallel to the surface, at different distances from the metal.

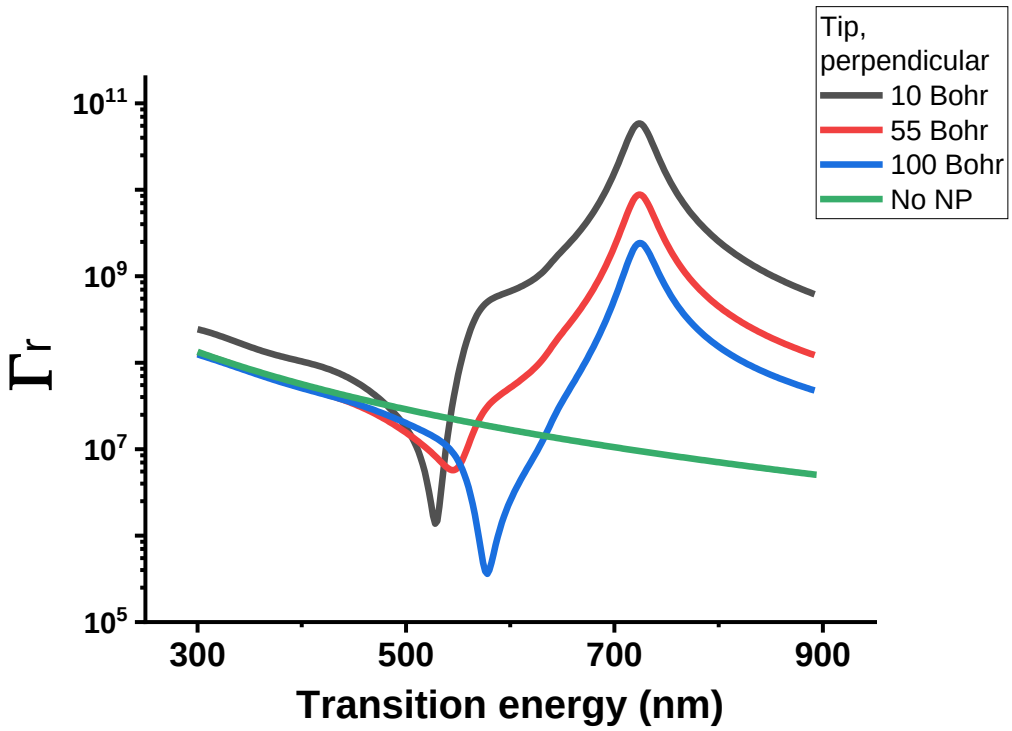

FIGURE 5.47: The effects of the tip of NP 775 over the radiative constant of a set of dyes with transitions from 300 nm to 900 nm, perpendicular to the surface, at different distances from the metal.

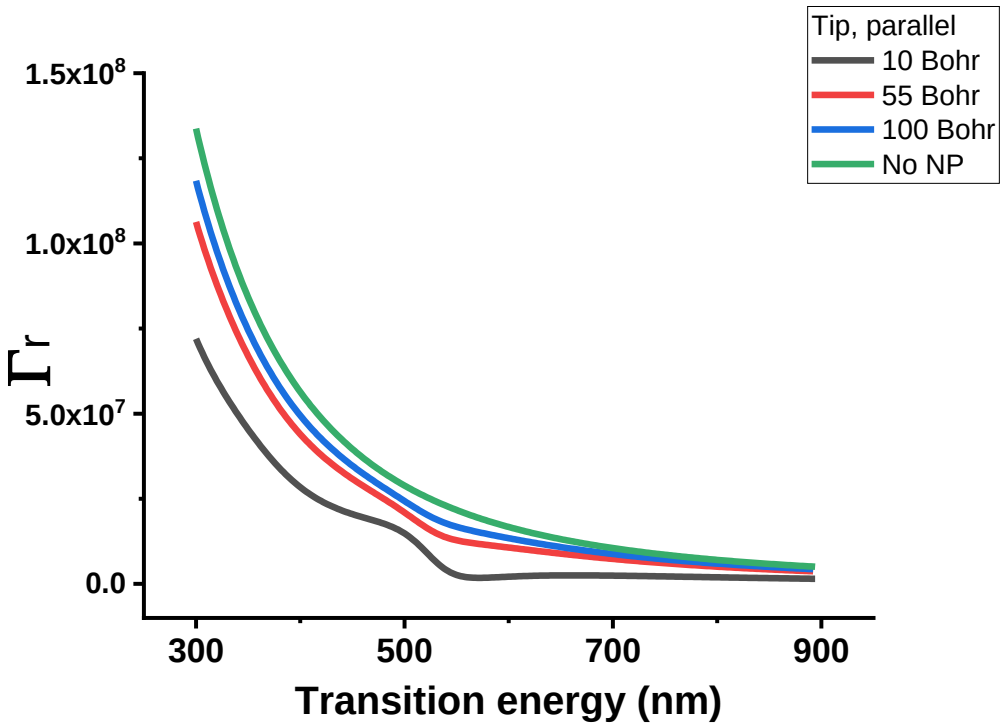

FIGURE 5.48: The effects of the tip of NP 775 over the radiative constant of a set of dyes with transitions from 300 nm to 900 nm, parallel to the surface, at different distances from the metal.

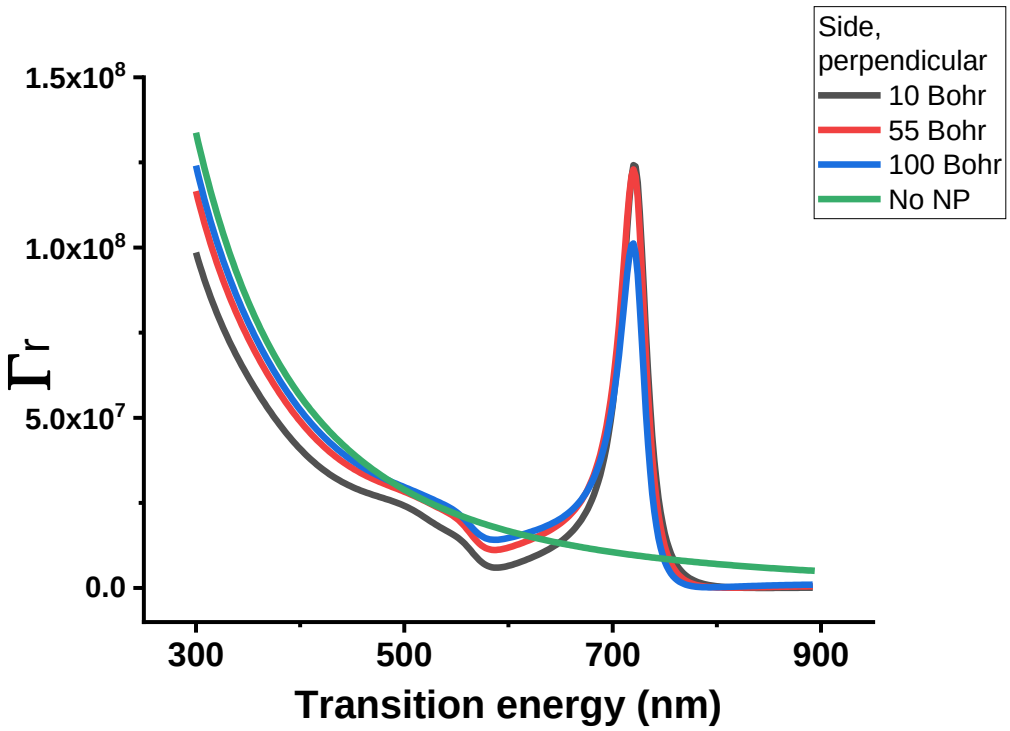

FIGURE 5.49: The effects of the side of NP 775 over the radiative constant of a set of dyes with transitions from 300 nm to 900 nm, perpendicular to the surface, at different distances from the metal.

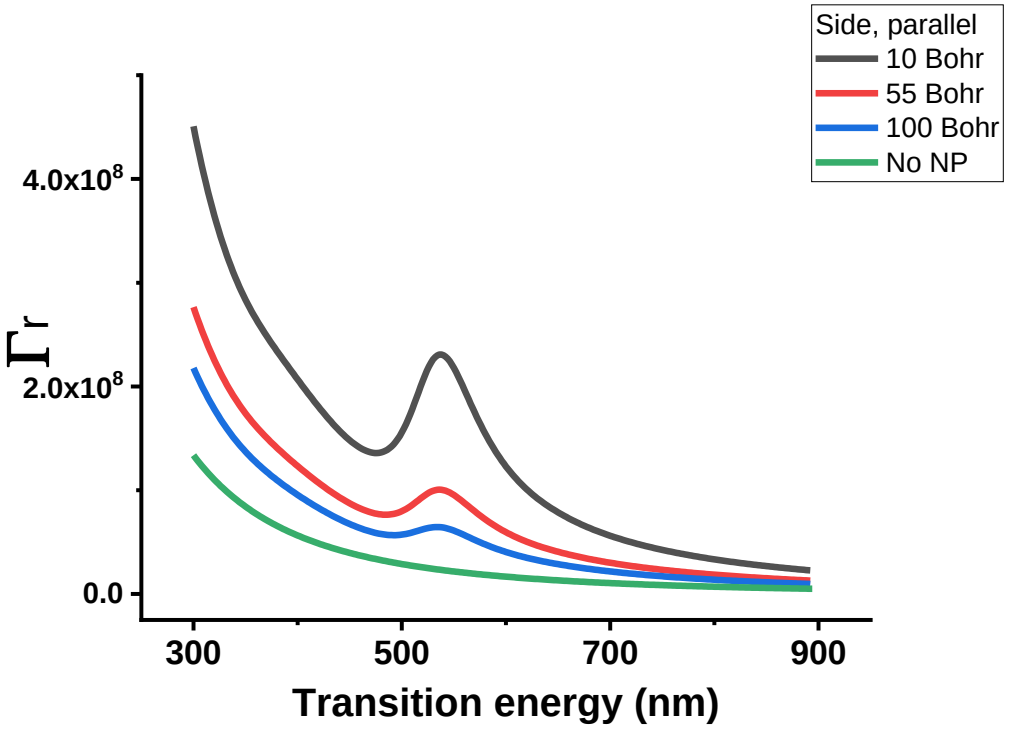

FIGURE 5.50: The effects of the side of NP 775 over the radiative constant of a set of dyes with transitions from 300 nm to 900 nm, parallel to the surface, at different distances from the metal.

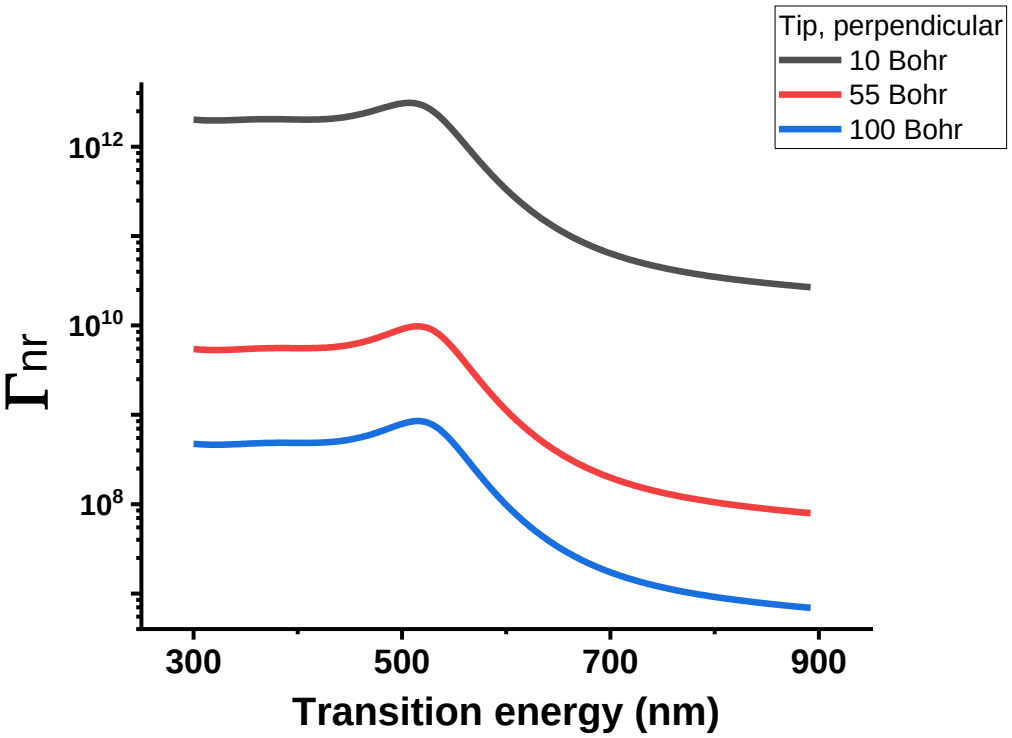

FIGURE 5.51: The effects of the tip of NP 775 over the nonradiative constant of a set of dyes with transitions from 300 nm to 900 nm, perpendicular to the surface, at different distances from the metal.

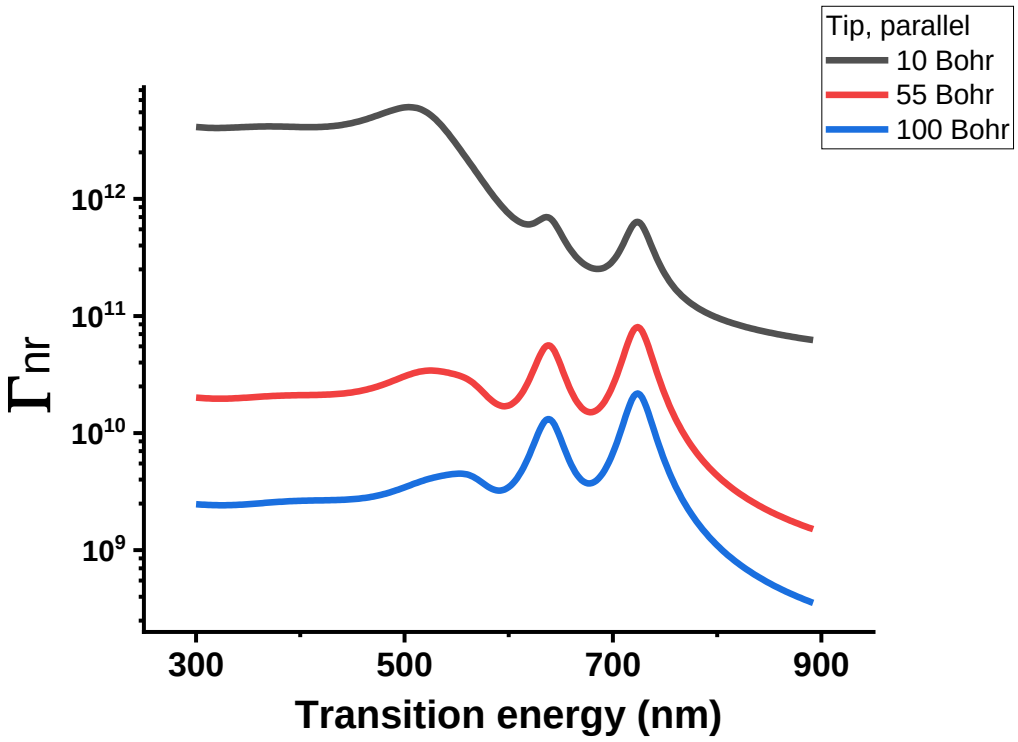

FIGURE 5.52: The effects of the tip of NP 775 over the nonradiative constant of a set of dyes with transitions from 300 nm to 900 nm, parallel to the surface, at different distances from the metal.

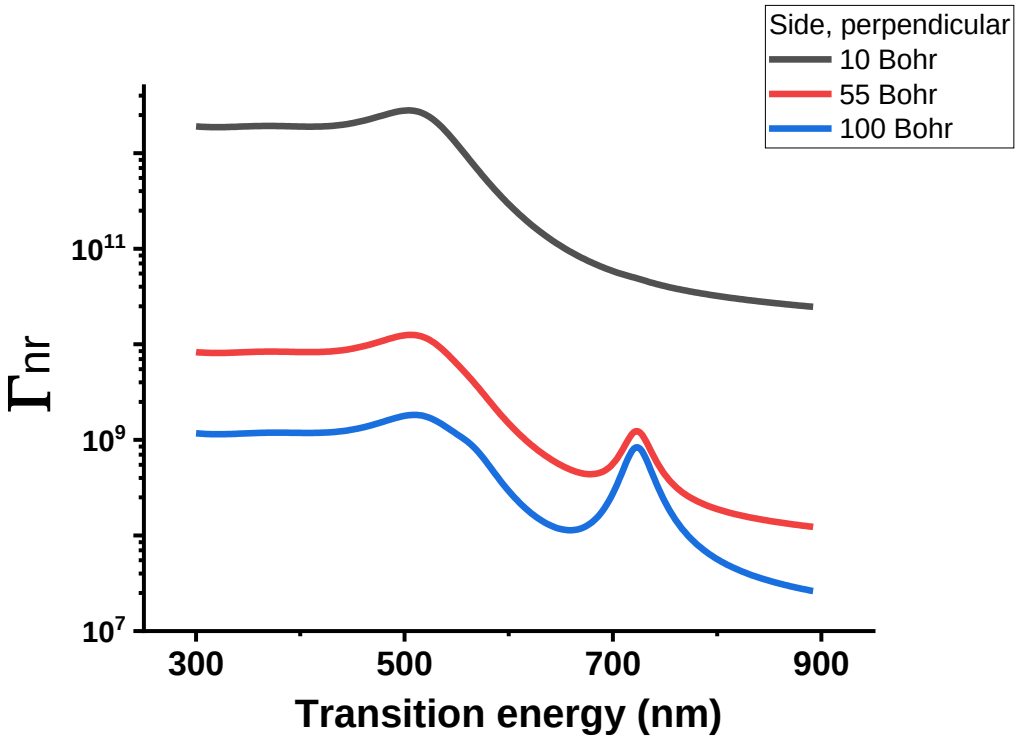

FIGURE 5.53: The effects of the side of NP 775 over the nonradiative constant of a set of dyes with transitions from 300 nm to 900 nm, perpendicular to the surface, at different distances from the metal.

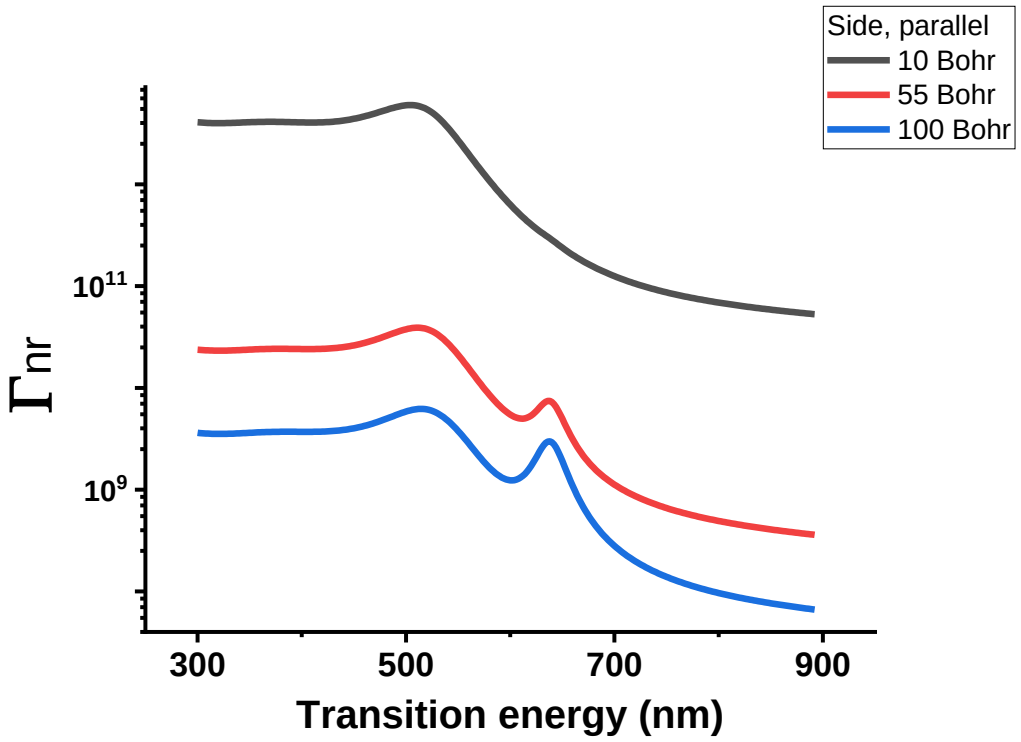

FIGURE 5.54: The effects of the side of NP 775 over the nonradiative constant of a set of dyes with transitions from 300 nm to 900 nm, parallel to the surface, at different distances from the metal.

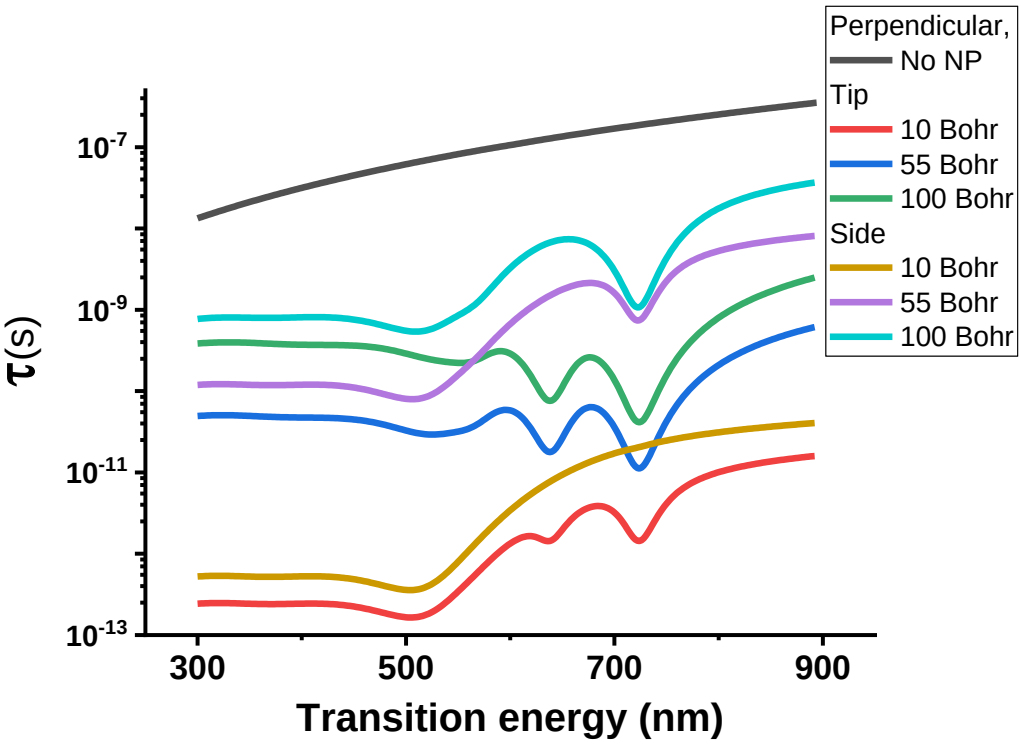

FIGURE 5.55: The effects of NP 775 over the lifetimes of a set of dyes with transitions from 300 nm to 900 nm, perpendicular to the surface, at different positions and distances from the metal.

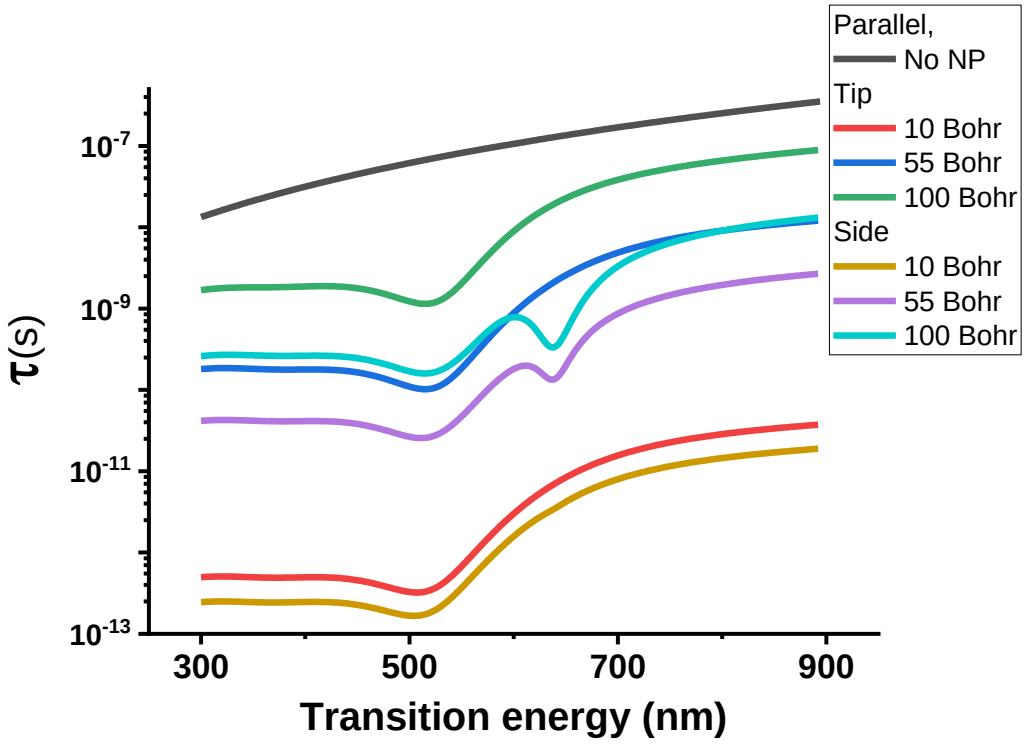

FIGURE 5.56: The effects of NP 775 over the lifetimes of a set of dyes with transitions from 300 nm to 900 nm, parallel to the surface, at different positions and distances from the metal.

quenched not only in emission efficiency but also in general luminance. When the dye is oriented parallel to the surface, though, the effect is always a quench, as can be seen in fig. 5.58. When Φ_{adj} is computed, considering a dye with a Φ_{int}=0.2, the presence of the nanoparticle results always in a quenching of the emission efficiency with respect to an already bad emitter, as shown in fig. 5.59 and 5.60, and the effect is even more pronounced when the emitter has a higher quantum yield originally. This results in a NP that strongly enhances, up to three orders of magnitude, the luminescence intensity of a dye that presents an emission at wavelengths longer than the LSPR at 723 nm, especially when the dye is grafted onto the tip of the NP, thanks to a very strong near-field enhancement that balances the reduction of the yield of the dye's emission.

5.4.3 Stokes shift effects

Same as for the previous, smaller, NP, introducing a Stokes shift between dye's absorption and emission shows a very interesting and strong enhancement either of the relative brightness, that increases up to 150 times in a very narrow region around the LSPR energy, starting from a Stokes shift of less than 25 nm, as presented in fig. 5.61. This means that also dyes with a relatively small Stokes shift can benefit by the extreme sensitivity over the transition wavelengths. The relative number of excited states, in fig. 5.62, shows an increase when increasing the Stokes shift, if the dye absorbs a the same wavelength as the NP, while is quenched in any other case.

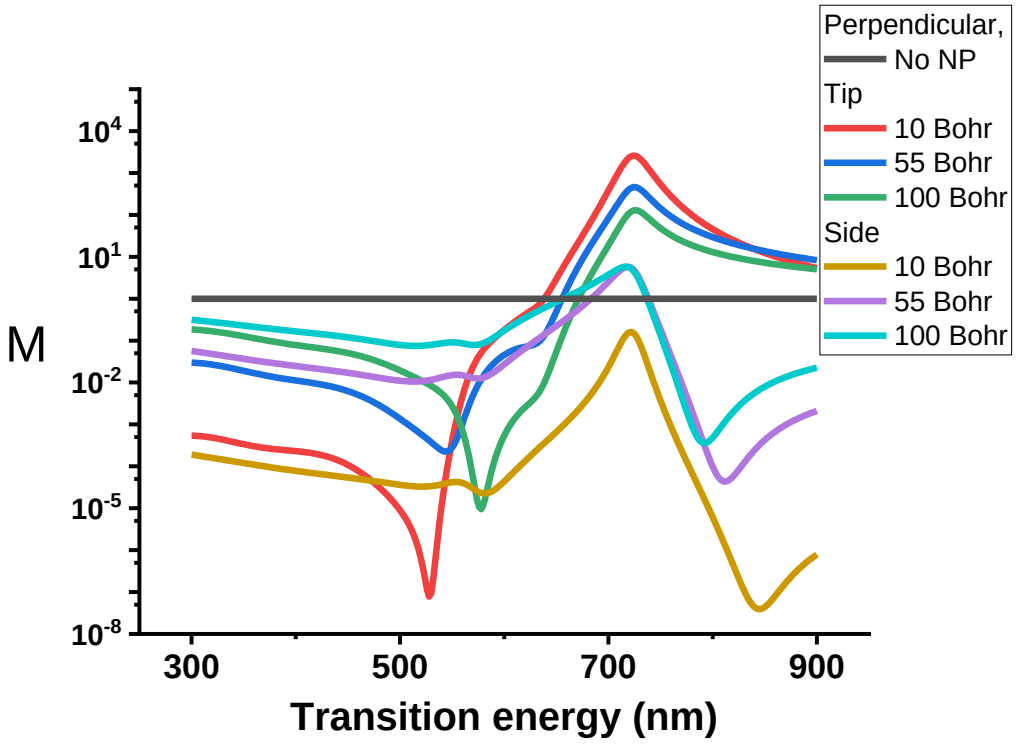

FIGURE 5.57: The effects of NP 775 over the relative brightness of a set of dyes with transitions from 300 nm to 900 nm, perpendicular to the surface, at different positions and distances from the metal.

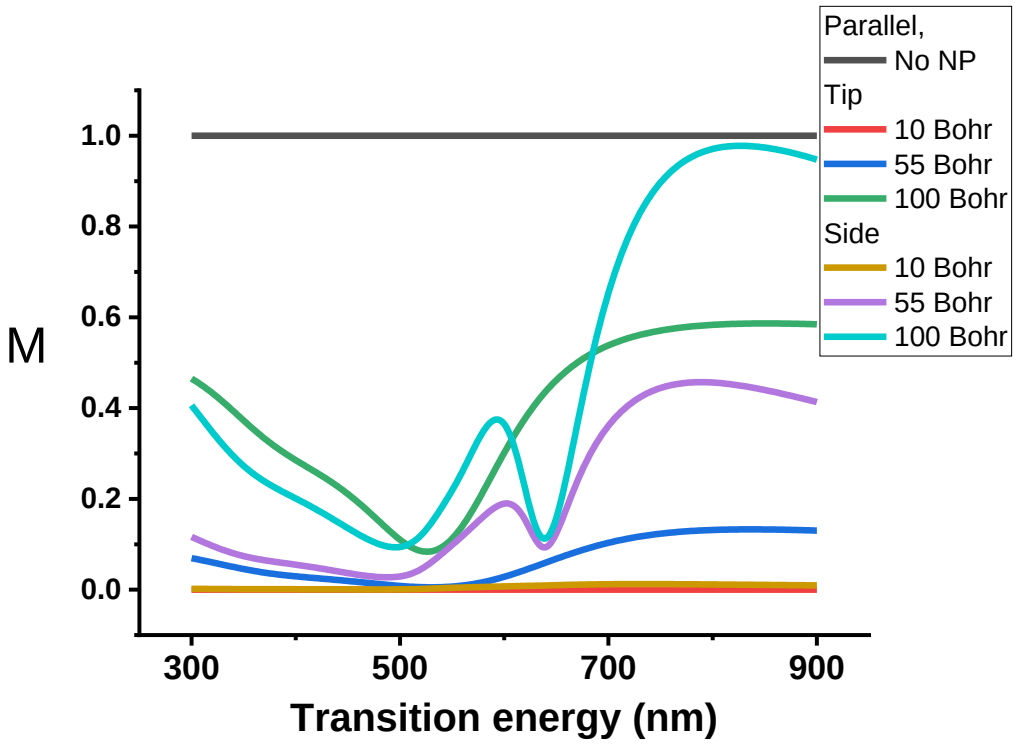

FIGURE 5.58: The effects of NP 775 over the relative brightness of a set of dyes with transitions from 300 nm to 900 nm, parallel to the surface, at different positions and distances from the metal.

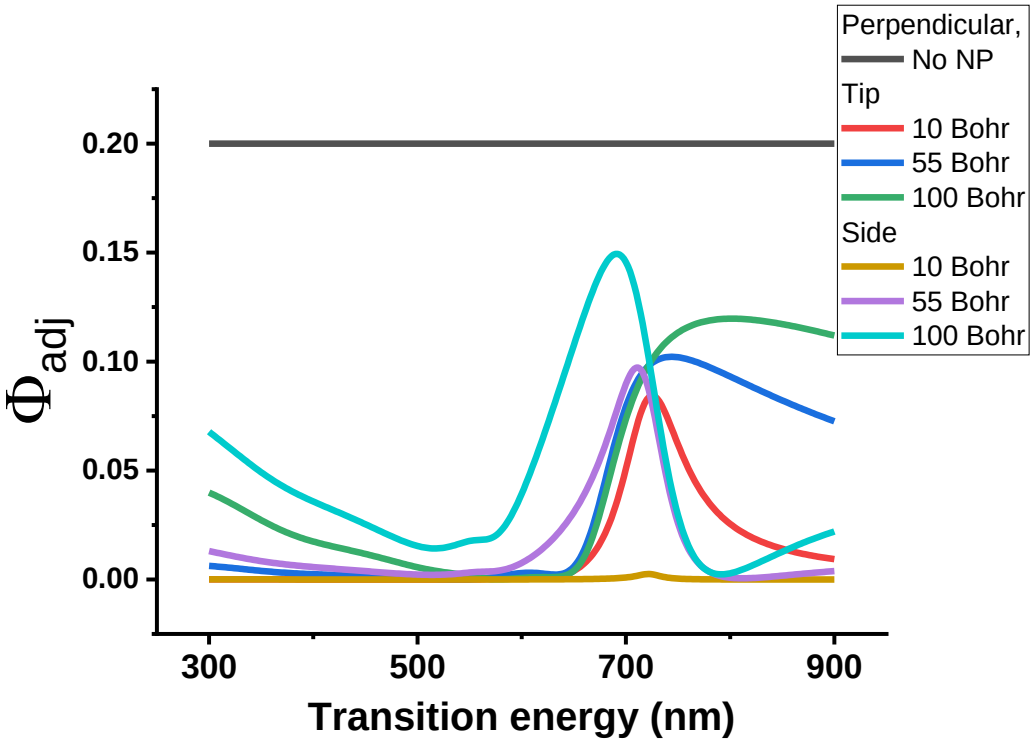

FIGURE 5.59: The effects of NP 775 over the adjusted quantum yield of a set of dyes with transitions from 300 nm to 900 nm, perpendicular to the surface, at different positions and distances from the metal.

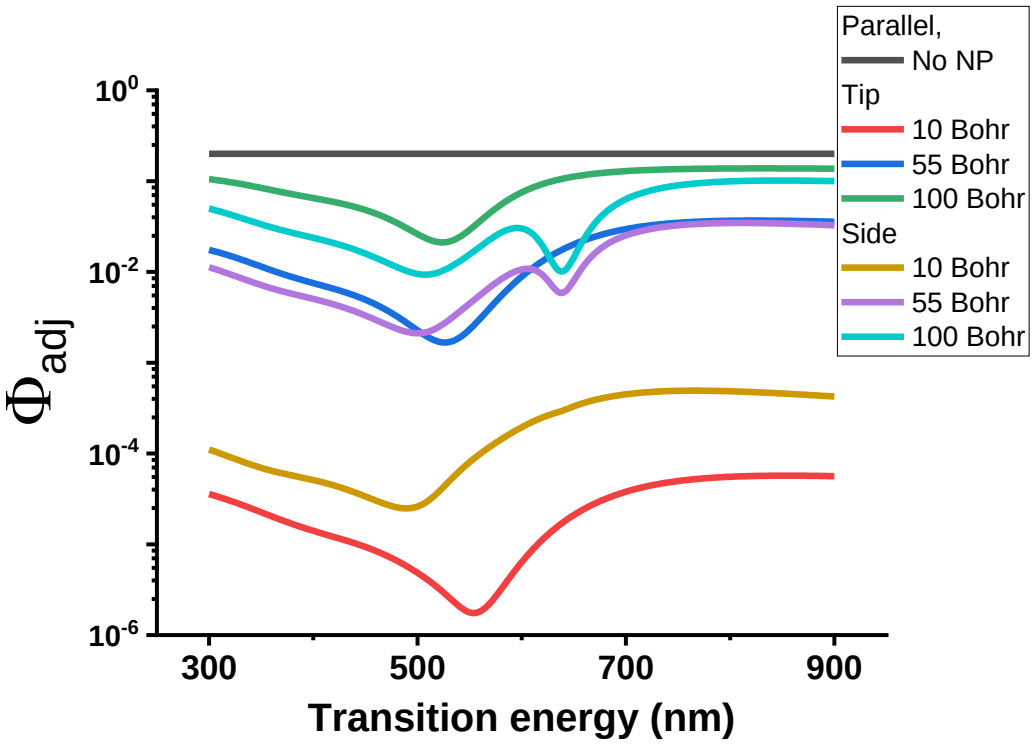

FIGURE 5.60: The effects of NP 775 over the adjusted quantum yield of a set of dyes with transitions from 300 nm to 900 nm, parallel to the surface, at different positions and distances from the metal.

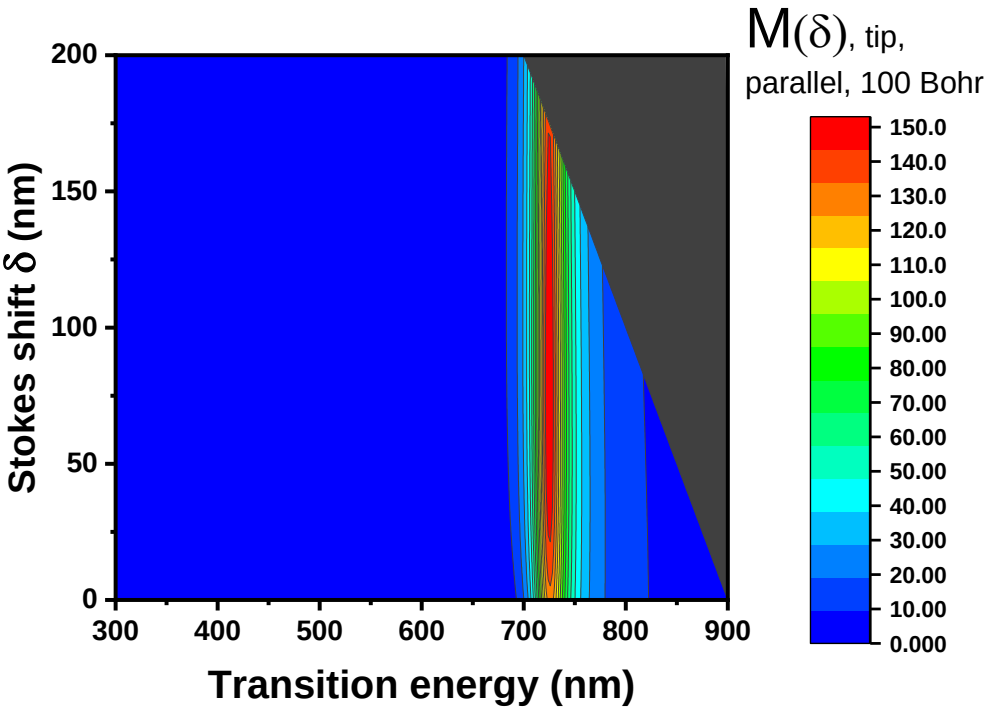

FIGURE 5.61: The effects of NP 775 over the relative brightness of a set of dyes with transitions from 300 nm to 900 nm, Stoke shift up to 200 nm, perpendicular to the surface.

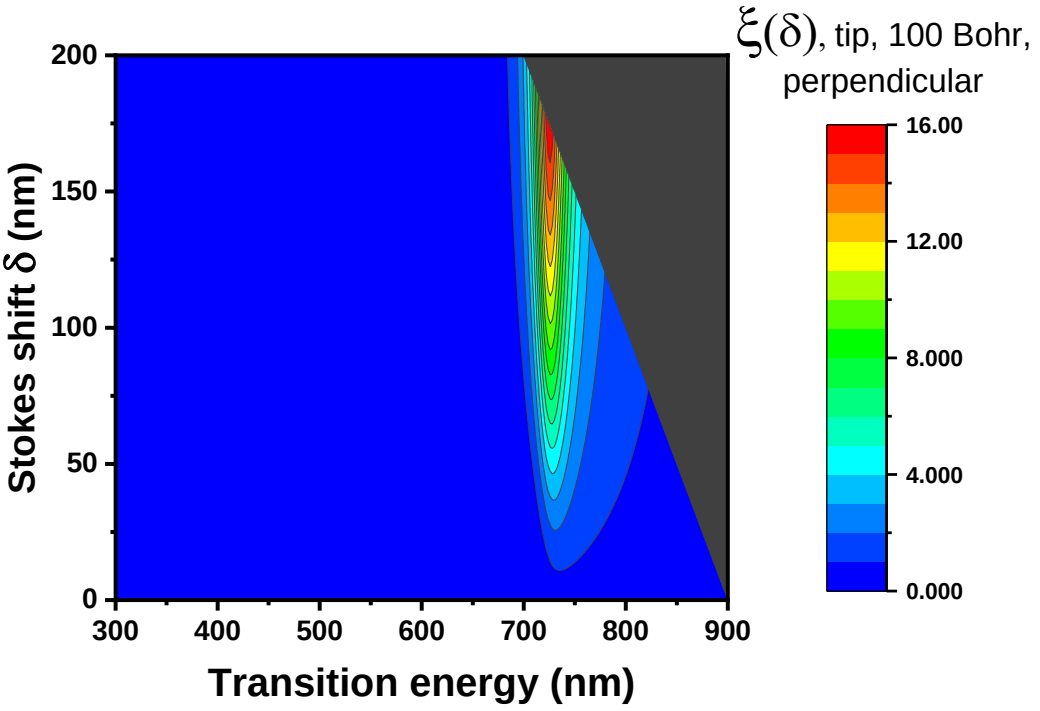

FIGURE 5.62: The effects of NP 775 over the relative brightness of a set of dyes with transitions from 300 nm to 900 nm, Stoke shift up to 200 nm, parallel to the surface.

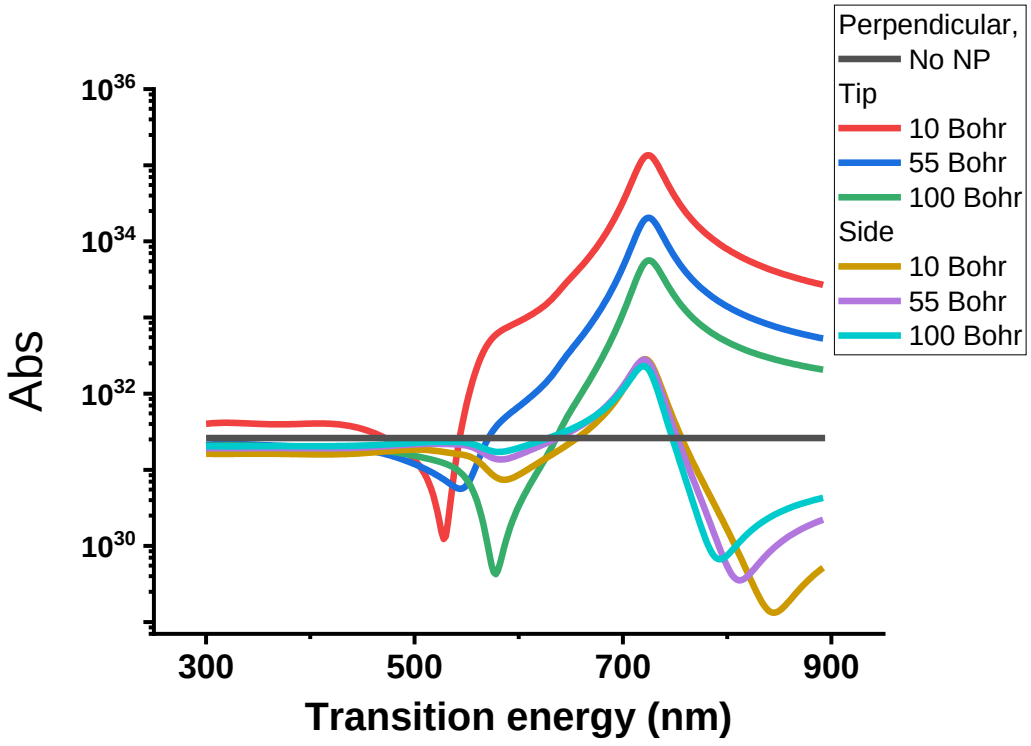

FIGURE 5.63: The effects of NP 775 over the absorption rate of a set of dyes with transitions from 300 nm to 900 nm, perpendicular to the surface, at different positions and distances from the metal.

5.4.4 Absorption

Absorption data, listed in figs. 5.63 and 5.64, show a behaviour very consistent with the emission properties: thanks to the near field enhancement the optical properties are maximized at the tip, especially when the dye is in resonance with the LSPR of the NP. Some cold spots can be observed also in this case, in particular for wavelengths higher than 750 nm for the side position and orientation perpendicular to the surface, and for any given possible dye at the tip, if the TDM is parallel to the surface, with a strong dip when near the surface and at energies around 550 nm.

5.5 Comparison of the nanoparticle effect

The results shown in section 5.3 and 5.4 show some similar trends and some differences between the effects that the two nanoparticles have over the optical properties of the same chromophores. In first place, the general trend is that the enhancement of any property is maximised at the tip, which is not surprising, considering that the tip is the region where the electric field, thus the near field amplification, is maximum. This is due to the presence of the tip itself, that concentrate the electric field in a smaller portion of the space, being the surface charge density much larger at the tip. This results, for example, in larger decay constants at tip position, either for radiative and nonradiative processes, which can be exploited in many ways. If the desired effect is an amplification of the emission, the tip is the best position to obtain it, with

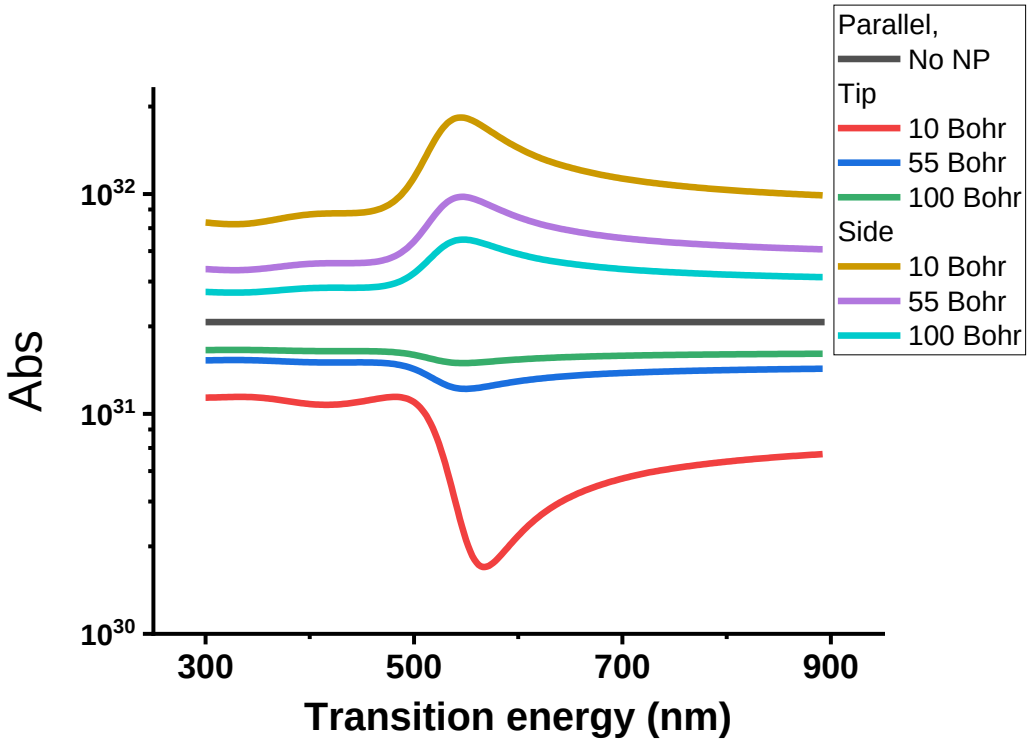

FIGURE 5.64: The effects of NP 775 over the absorption rate of a set of dyes with transitions from 300 nm to 900 nm, parallel to the surface, at different positions and distances from the metal.

this class of bipyramidal nanoparticles. This holds true as well if the coveted effect is an increase in the speed of nonradiative deactivation, which is typical, *e.g.*, for photothermal therapies, since the nonradiative dielectric constant Γ_{nr} is usually maximised at the tip, nearby the surface of the nanoparticle. For this kind of applications, plasmon resonance enhancement can be very effective, acting both as an antenna and amplifier for the desired effect: considering that on one side the absorption is raised by up to three orders of magnitude, and, concurrently, Γ_{nr} can be very high, going over $10^{12}s^{-1}$, the total result can be extremely resourceful in overcoming many of the issues usually related to photothermal based therapies. The other common trait is the effect of LSPR. As expected, when the dye absorbs or emits in the vicinity of the plasmon resonance, the optical properties are greatly enhanced. On the other side, when the dye has energies slightly higher than the plasmon, the retarded response of the electron density with the projected dipole destroys the optical enhancement, leading to a strong quench. The last common trend is the extreme sensitivity of the effect to any minor detail: very small differences in decay rates, or the presence of very dim secondary plasmon resonances, can affect deeply the overall properties of the combined system, as can be seen in fig. 5.52, where very weak plasmon resonances modify the rate of nonradiative decay of orders of magnitude, while being almost untraceable in the absorption spectrum of the NP alone (see fig. 5.2).

Even if some common trends were present, many evident differences arose between the two NPs considered. To better assess them, a particular case has been considered, where the dyes are placed perpendicularly to the surface at 100 Bohr from the metal surface, at tip and side position, for both the NPs. A Stokes shift of

50 nm has been introduced too, in order to better simulate a real life scenario, and to gain some knowledge from the relative number of excited states ξ. The relative brightness, in fig. 5.65, shows that for the NP with smaller aspect ratio the luminance is always enhanced if the dye absorbs with a wavelength above 550 nm, while this does not hold true for the NP with the higher aspect ratio, where the enhancement is stronger at the tip, around the LSPR, but for the rest is more quenched than the counterpart. Another important difference is seen in fig. 5.66, where is presented the quantum yield of the dyes in the vicinity of the NP if they had a ϕ_{int} of 0.2. The very interesting effect of an increased quantum efficiency of the emission can be observed only in the case of the smaller NP, while the other quenches the efficiency in any case. It was not possible to find a region in space where the emission would be enhanced also in the case of the bigger NP, within the limits of the database created, but a similar effect could also be present. Thus the importance of having an extended database, since the sensitivity is so high. It is not unlikely that the hot spot observed in the case of the smaller NP exists for the bigger NP, but simply at other distances not simulated. The relative number of excited states exhibit a similar trend: in fig. 5.67 the strong effects around the LSPR peaks are counterbalanced by strong quenches in the higher energy regions. Two very different behaviours can be seen between the two NPs in the case of the side position, where the smaller NP has a broader and milder curve that always lies below 1, and the larger NP shows a predominant peak at around the LSPR, more similar to the behaviour of other orientations, or to dyes placed nearer to the surface. Another very different behaviour between the two NPs is how the excited states' lifetimes react to the presence of the NPs. In fig. 5.68, for the higher aspect ratio NP the number of sinks and bumps is much higher, following secondary plasmon resonances, while for the smaller NP, where these secondary resonance are non traceable in the absorption spectrum, only the transversal plasmon resonance effect is seen, and the main, longitudinal one does not show any effect as a proper peak.

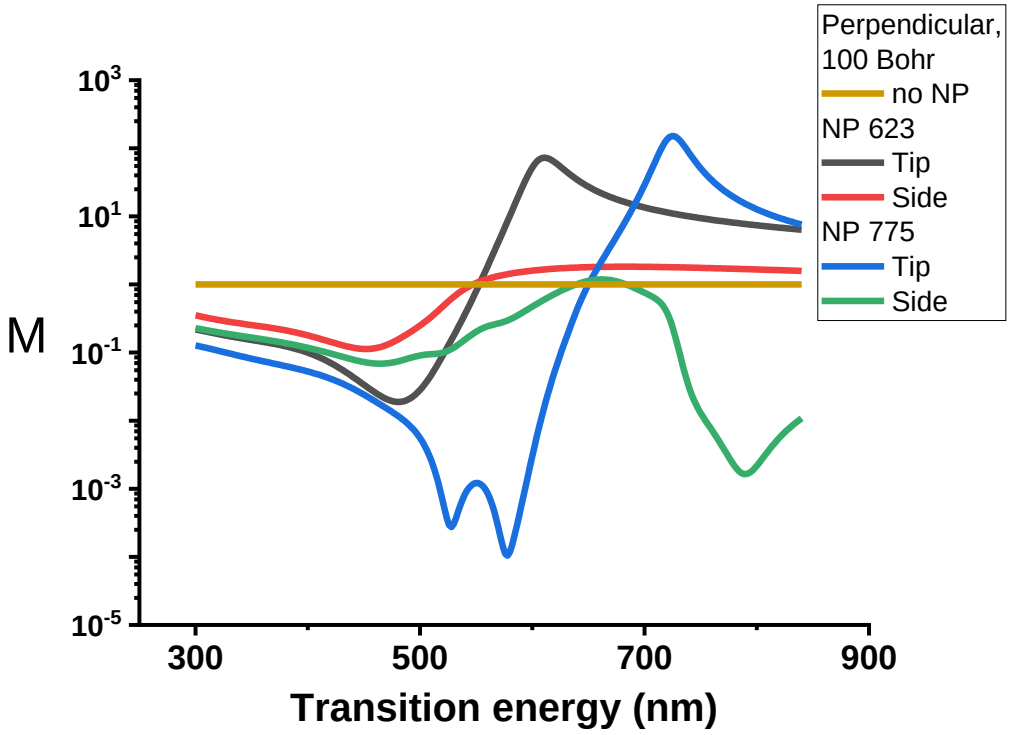

FIGURE 5.65: A comparison of the relative brightness between NP639 and NP775, for a set of dyes with absorption from 300 nm to 900 nm, Stokes shift of 50 nm, at 100 Bohr from the metal.

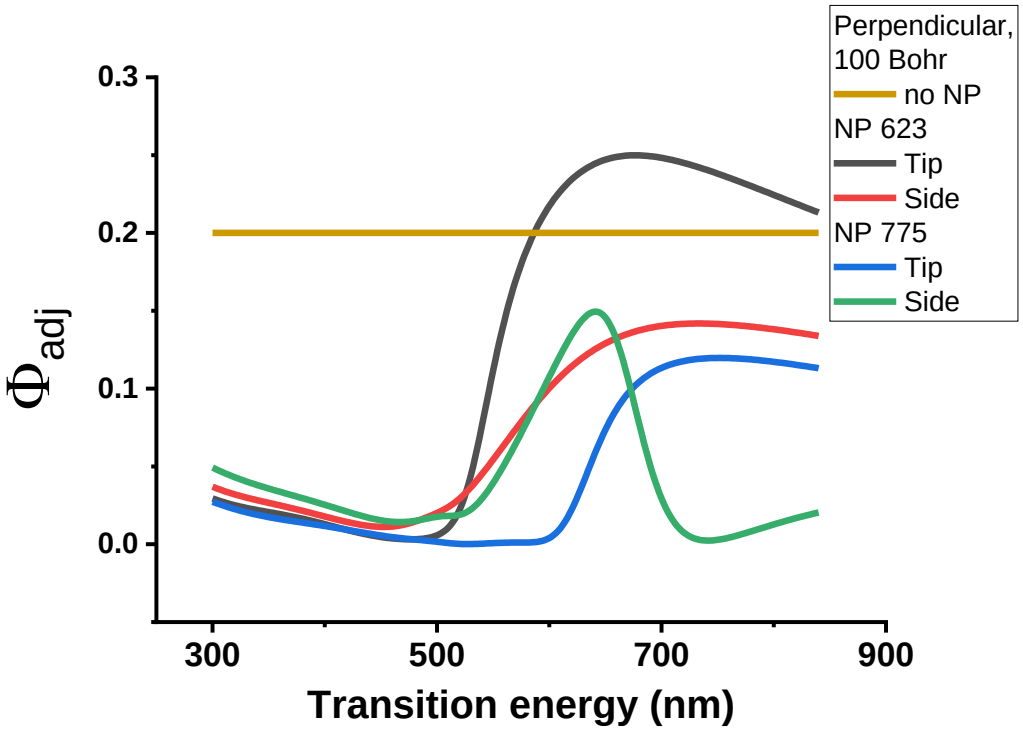

FIGURE 5.66: A comparison of the adjusted quantum yield between NP639 and NP775, for a set of dyes with absorption from 300 nm to 900 nm, Stokes shift of 50 nm, at 100 Bohr from the metal.

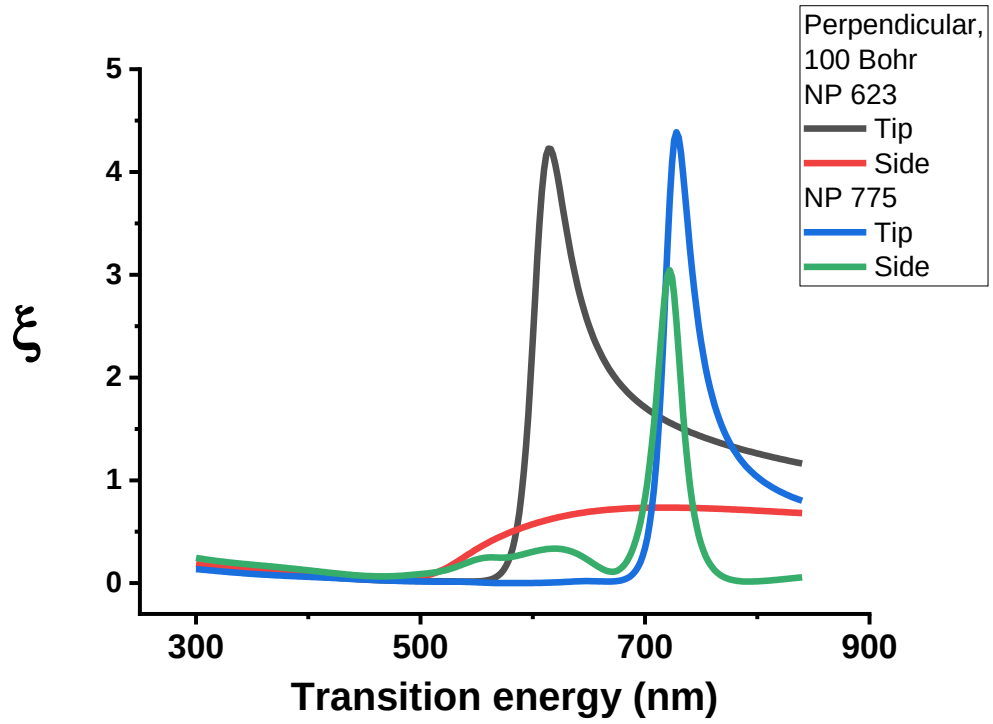

FIGURE 5.67: A comparison of the relative excited states population between NP639 and NP775, for a set of dyes with absorption from 300 nm to 900 nm, Stokes shift of 50 nm, at 100 Bohr from the metal.

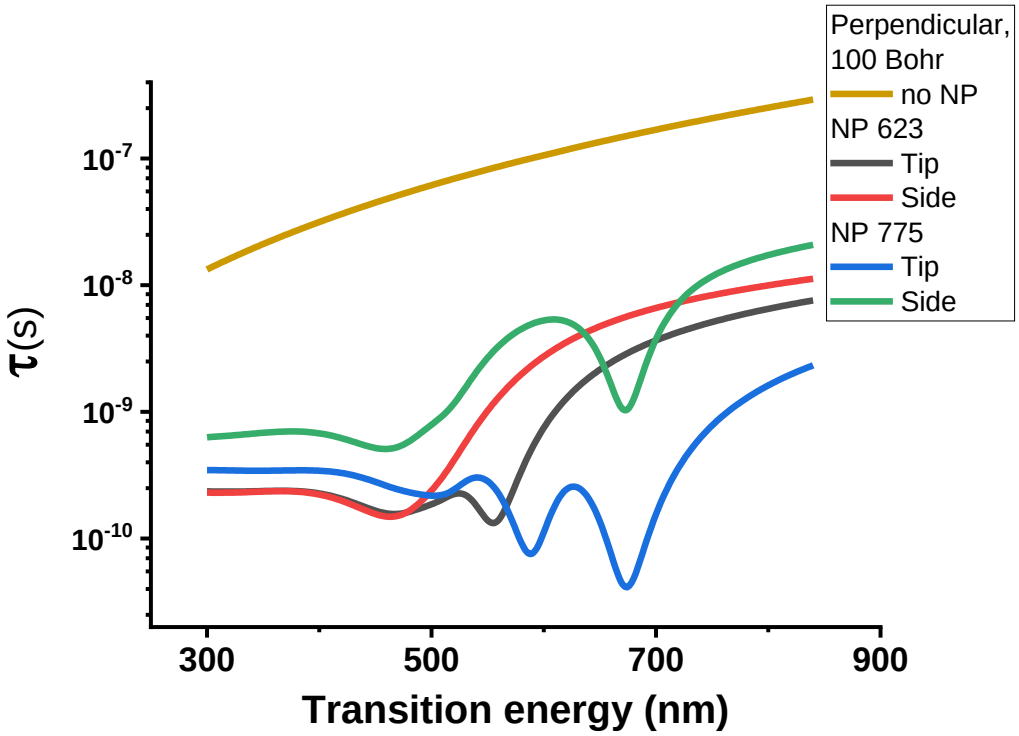

FIGURE 5.68: A comparison of the lifetimes between NP639 and NP775, for a set of dyes with absorption from 300 nm to 900 nm, Stokes shift of 50 nm, at 100 Bohr from the metal.

5.6 Conclusions

The main chemical insight is a design qualitative indication: the optical effects are maximized at the LSPR frequency while they undergo the highest quench at frequencies slightly higher. This is due to the counter-phase effect of the dipole produced in the metal as a response of the oscillating transition dipole moment. Such a recurring effect in calculations should not change if better approximations are included (such as a size dependent dielectric function that corrects the electrostatic approximation), since the approximation improvement would only change the energy at which the interaction happens but not the nature of the coupling with the LSPR. Another interesting effect is to see that the orientation of the dye affects strongly the quantum yield: when perpendicular to the surface the emission quantum yield does not change significantly at energies lower than the LSPR, which is a very important effect: since absorption is maximized at the LSPR, the Stoke shift of the emission would not be quenched by the metal. On the other side, when parallel to the surface, the quenching is observed not only at energies higher than LSPR but also at lower energies, making the Stoke shift a much bigger problem (or desirable effect if needed). In short: LSPR enhances optical properties of coupled dyes, while it quenches the emissions that happen at slightly higher energies. This might be a quite important effect in cases as molecules used in photothermal therapies, where the emission needs to be minimized while the absorption is carried by the metal nanoparticle. Another interesting, but foreseeable, effect is that at the tip position, where the electric field is most intense, optical properties have the strongest perturbations, in either direction of enhancement or quench. This might be interesting on a synthetic point of view because, when synthesising these hybrids, the target should be to concentrate as much as possible the chromophores on the surface around the tip, or try to avoid it, according to the desired effect. One important remark that needs to be stressed is that this method does not give any information over the behaviour of the excited states' energy difference between the molecule *in vacuo* with respect when near the NP. The meaning of the "Transition energy" in the plots is that it's the energy of the emission of a dye when already near the NP, with no information on any shift given by the presence of the metal from the behaviour *in vacuo*. This information should be given by quantum mechanical based simulations, where the shifts given by the distortion of the molecule and of the electron cloud can be properly assessed. One example is given by the implementation of a reversed PCM inside the code GAMESS, where the electrostatic effects of the NP are taken into account *via* the polarization charges that define the metal surface in the PCM framework. However, when the simulations have been performed, the intensities of those shifts happen to be far below any interesting values, since they settle around the order of 10 to 100 μeV.

The more complex parameters (Φ_{adj}, M, and ξ), introduced at the beginning, give a deeper glance into the conclusions before. As expected, ξ and Φ_{adj} give the very same results when compared, in a case where no Stokes shift is considered. The only difference is that one is commensurate with respect to a Φ_{int} of 0.2 and the other is normalized to 1, since it's a parameter relative to itself in the absence of the NP. When considering Φ_{adj} over a Φ_{int} of 0.2 we notice that there is a region of transition energies where not only the relative brightness (or magnitude M) is increased, but also the quantum yield increases with respect to the initial Φ_{int}. This is an important

design indication: it is possible to reach a regime where not only the luminescence is increased due to the enhanced electromagnetic field, but it also affects the proper quantum yield of the emission process. While this happens for the smaller NP, the behaviour could not be reproduced for the bigger NP. This either is a consequence of the different sizes and shapes that concentrate the enhancement effects in different region of the surrounding space, and simply we were not able to spot the region for limits in the range of the database, or, on the contrary, a tangible physical difference between the two NPs. In the latter case, the difference in sharpness of the tips might be the main actor behind the effect, but we were not able to discern between the two hypotheses.

When introducing Stokes shift onto the matter, the results are quite interesting too: the very same ranges of excitation energies give a strong enhancement in the luminescence magnitude (M), but also affect the number of excited states that we are able to create from the very same exciting light intensity. The main reason for this is a strongly increased absorption rate, and, in some special cases, also to an increased quantum yield. The main takeaway message from the computation of ξ is that, while the dye is placed onto the tip of the NP at a distance such that the nonradiative process is slow enough to keep the excited states alive, and if the transition dipole moment is orientated parallel to the main LSPR, the enhancement is very strong, otherwise, in other positions and orientations, the fluorescence process ends up being strongly quenched. This can lead to some experimental indications for the synthesis, especially which are the regions to focus the grafting of the dyes, in order to obtain the highest emission enhancement possible, or, conversely, the fastest nonradiative decay.

In this regard, the assembly of a finely detailed database of the near field enhancement that NPs have over the optical properties of molecules might prove to be a valuable tool for directing the synthetic efforts. The computational cost of these simulations is very light, allowing for a very detailed and fine survey of the surface enhancement effects, with interesting potential benefits, at least on a qualitative point of view. The amount of approximations implemented, unfortunately, do not give the confidence to expect quantitative results. These could be achieved instead by deeper and more refined simulations. For example, the representation of the molecules with their transition densities, extracted from TDDFT calculations, instead of pointlike transition dipole moments, and the extension from the quasi-static approximation to a full electromagnetic approach, should give much more realistic and reliable results. However, these are much more demanding tasks, computationally, and do not allow for a systematic scanning of the many parameters that are involved, such as distance, orientation, transition energy, transition intensity, Stokes shift, and others considered in this work. Therefore, the finely detailed database should serve as a guidance for these simulations, allowing for a selection of the most promising parameters instead of a trial and error approach.

Chapter 6

Future perspectives: the hybrid system as a whole

After showing that the quantum mechanical approach is not truly feasible for the class of materials (chapter 3), proving that the classical electrodynamics approach works very well in describing the plasmonic properties of Gold nanoparticles (chapter 4), and building up the tools for creating a usable database for the near field enhancement of the metal nanoparticle over the emission properties of organic dyes (chapter 5), the last step to complete the description of hybrid nanoparticles systems is to describe the properties of the system as a whole. Since Gold NPs are not spontaneous emitters, and the plasmonic excitation decays only *via* nonradiative paths, it is safe to exclude the metallic portion of the hybrid system from the study of fluorescence properties, other than accounting for the perturbation effects it shows as a dielectric, thus making the general approach presented in chapter 5 the go-to method to tackle this kind of problem. In section 5.6 we referred to possible extensions of the very brutal approximation adopted, in order to provide more accurate data once the main parameters involved have been narrowed down to the most suitable for a certain application, to validate and confirm them with a more solid, but much more expensive, approach. What is left out is a way to compute and predict the optical absorption properties of the hybrid system as a whole. While, as stated, the emission comes solely from the chromophores, the NPs possess a very strong absorption, with oscillator strengths that are abundantly larger than the single molecule, and in many cases also than the whole collection of the dyes bound, or physisorbed, to the metal surface. This makes the computation of the single dye absorption, within the hybrid system, a parameter describing internal properties, but not a truly physical observable of the combined system, since it's impossible to excite the molecules without irradiating the NP.

Therefore, an approach to compute the cross section of the hybrid system is still missing. The main target, in this regard, is exploiting the properties of generalized Mie scattering theory, within the enclosure of classical electrodynamics, using effective frequency dependent dielectric permittivities, and dividing in different volumes the main components. The metal NP would be one volume, with the same approach of chapter 4, then an outer layer with its own frequency dependent dielectric function, would act as the combined system of chromophore and surfactant, and then the solvent would lie outside. A representation of this model can be found in fig. 6.1. Geometrically there are two main attributes of the system to take into account: the size and shape of the metal nanoparticle, and the thickness of the surfactant layer.

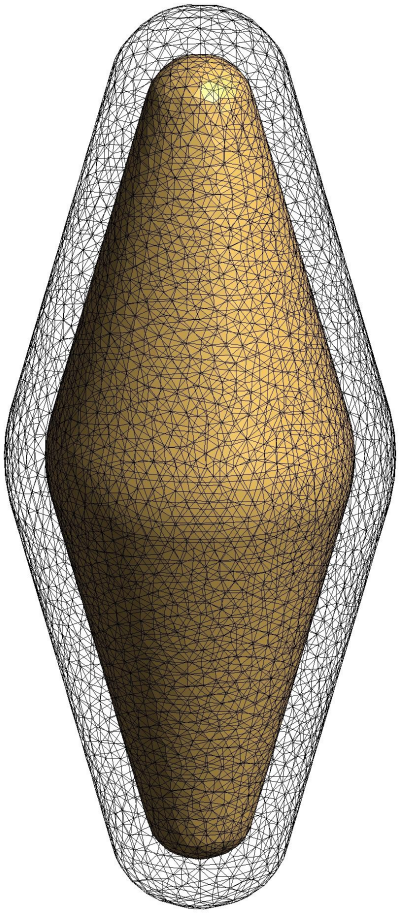

FIGURE 6.1: A picture of the meshes used in the model, with the Gold nanoparticle in Gold, and the surfactant layer wrapping it

While the dielectric permittivity of Gold is already modelled and validated from fitting Drude-Lorentz based functions to the experimental data, there are many possible recipes to compute the dielectric function of the surfactant layer.

The simplest one is considering the surfactant layer to be a simple organic solvent and setting it to a single dielectric constant. This approach is brutal, and while for the surfactant itself, being a non-optically active molecule, is not a bad approximation, for the chromophore clearly loses all the frequency dependent information.

Still, the effect would be far from negligible in computing the absorption spectra. We performed a test simulation using as a base one of the NP simulated in chapter 4, in particular the one with LSPR at 639 nm, adding a surfactant layer with 5Å of thickness, with water outside the system. The simulations were then performed ranging the surfactant layer relative permittivity from 1.00 (complete vacuum) to 4.00, obtaining the results showed in fig. 6.2. The peaks of the absorption maxima shift from 585 nm with the vacuum layer, to 620 nm at and ε of 1.78 (the value for water), corresponding to the results presented in chapter 4, to a value of 630 nm for an ε of 2.00, typical of most organic materials, up to a maximum at 676 nm for an ε of 4.00, which corresponds, as an example, roughly to the relative permittivity of Silicon dioxide (quartz). The thickness of 5Å is taken as a general realistic value for the surfactant layer, as shown in various literature works [104, 133]. The apparent

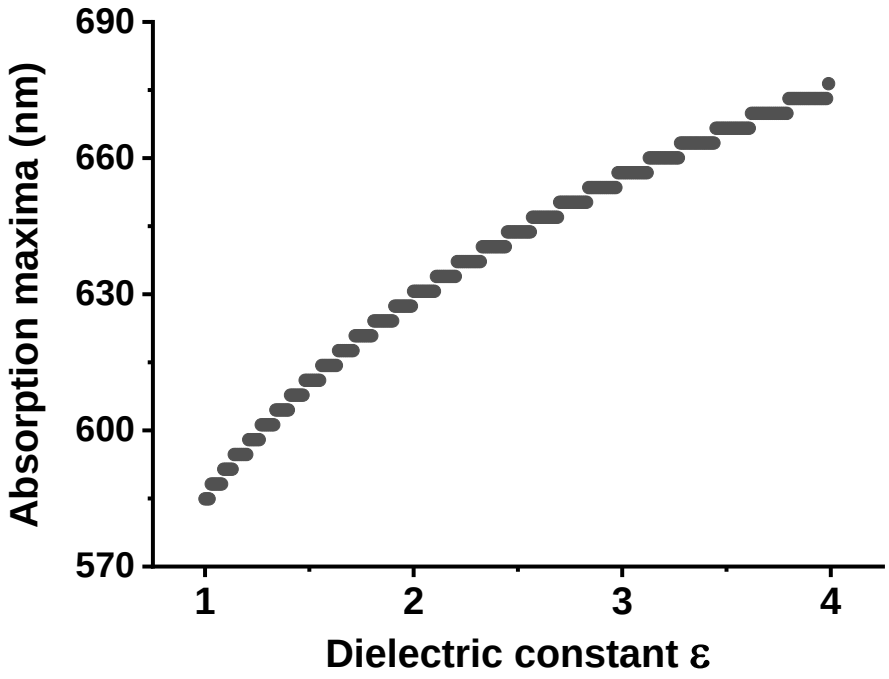

FIGURE 6.2: The effects of changing the dielectric constant in the surfactant layer over the absorption maxima of the hybrid system.

steps observed in the plot are due to the distance in frequency between subsequent simulated points in the spectrum, that has a resolution around 3 nm for these computations.

The obvious improvement over this approach is to employ a frequency dependent dielectric function for the surfactant layer that allows to better describe its optical properties. This can be built in many ways [134, 135]. One is to fit a Lorentzian curve, using some realistic broadening, around the absorption maximum of the considered dye, overlapping it with the surfactant's relative permittivity. This would bring to fast and quite reliable calculations, that would allow, in principle, to build a whole database of possible interactions between a very wide variety of NPs and possible chromophores. A more polished, and physically sound approach would be building the frequency dependent dielectric function from an effective medium approximation, like the Maxwell-Garnett model. In this model, all the inhomogeneities are levelled into a single, effective, parameter that is computed from the characteristics of the composite material. In particular, the chromophores are considered as spherical inclusions that occupy a fixed volume fraction within a continuous matrix, that represents the surfactant. A more detailed description is presented in section 2.4.

There are many ways to acquire the physical quantities to insert in the effective model presented. As stated, hypothetical values, used to build a database, or experimental data can be used to find the necessary parameters. Another way to gather the desired quantities is exploiting *ab initio* methods such as TDDFT. This approach, although much more computationally heavy, grants a fine control on what the system is actually made of, allowing to change up to the smallest detail in the system at hand. The density, distance, orientation and nature of the dye can be factored in and

modified to check the effects over the overall hybrid system behaviour. Any code could be used to compute the desired quantities, but most need the estimation of the sum-over-states to compute the polarizability, and thus the relative dielectric permittivity. On the other hand, the Quantum-Espresso package allows to compute directly the polarizabilities using the Liouville-Lanczos approach [74–76]. This would be a novel approach with no previous examples in the literature, since the capabilities of Liouville-Lanczos approach have not yet been explored in this matter. The presented concept allows to compute not only the dielectric function of single chromophores, but of much more complex systems. The periodic boundary conditions, intrinsic in the plane-waves bases used in the DFT calculations in Quantum-Espresso, allow, for example, to compute the interaction of chromophores not far enough to be considered non-interacting, just exploiting the self-interaction of nearby replicas instead of actually computing two separate molecules. It allows also to insert the surfactant inside the box, forming a building block that represents the whole layer, eliminating the need to compute an effective dielectric constant with Maxwell-Garnett model, since the overall polarizability already takes into account the dye, the surfactant and the respective volume ratios, but at a much more controlled, and physically sound, level.

The last step would be to include in the TDDFT calculation, along to the chromophore and the surfactant, also a slab of the metal, in order to better simulate the effect of the presence of the metallic surface, especially when the dye is very near to the surface, but, most importantly, allows to have an estimate of the charge transfer character effects, since the classical electrodynamics approach with polarizable dielectrics cannot, by its own architecture, account for exchange of electrons, since no electrons are involved, but only polarizable continuums. This approach is not new in the literature, and has already been used to model this type of interaction [136]. The final model would then be the classical full electromagnetic model presented at the beginning, with the metal described by its own, experimentally measured, frequency dependent relative dielectric permittivity, the solvent described by its own dielectric constant, and the surfactant layer described with a dielectric constant that comes from *ab initio* calculations that account for the chromophores, the organic environment around the chromophores, and small metallic slab to detail the interaction between the dye and the metal surface.

References

[1] Oliviero Andreussi et al. “Radiative and nonradiative decay rates of a molecule close to a metal particle of complex shape”. In: *The Journal of Chemical Physics* 121.20 (Nov. 2004), pp. 10190–10202.

[2] D. Chateau et al. “From gold nanobipyramids to nanojavelins for a precise tuning of the plasmon resonance to the infrared wavelengths: experimental and theoretical aspects”. en. In: *Nanoscale* 7.5 (Jan. 2015), pp. 1934–1943.

[3] Ana Sánchez-Iglesias et al. “High-Yield Seeded Growth of Monodisperse Pentatwinned Gold Nanoparticles through Thermally Induced Seed Twinning”. en. In: *Journal of the American Chemical Society* 139.1 (Jan. 2017), pp. 107–110.

[4] Denis Chateau et al. “Beyond the Concentration Limitation in the Synthesis of Nanobipyramids and Other Pentatwinned Gold Nanostructures”. In: *Applied Materials & Interfaces* 11.42 (2019), pp. 39068–39076.

[5] Uri Banin, Yuval Ben-Shahar, and Kathy Vinokurov. “Hybrid Semiconductor–Metal Nanoparticles: From Architecture to Function”. en. In: *Chemistry of Materials* 26.1 (Jan. 2014), pp. 97–110.

[6] Anne Kotiaho et al. “Photoinduced Charge and Energy Transfer in Phthalocyanine-Functionalized Gold Nanoparticles”. en. In: *The Journal of Physical Chemistry C* 114.1 (Jan. 2010), pp. 162–168.

[7] Ruibin Jiang et al. “Metal/Semiconductor Hybrid Nanostructures for Plasmon-Enhanced Applications”. en. In: *Advanced Materials* 26.31 (2014), pp. 5274–5309.

[8] Suljo Linic et al. “Photochemical transformations on plasmonic metal nanoparticles”. en. In: *Nature Materials* 14.6 (June 2015), pp. 567–576.

[9] Clemens Burda et al. “Chemistry and Properties of Nanocrystals of Different Shapes”. en. In: *Chemical Reviews* 105.4 (Apr. 2005), pp. 1025–1102.

[10] Kathryn M. Mayer and Jason H. Hafner. “Localized Surface Plasmon Resonance Sensors”. In: *Chemical Reviews* 111.6 (June 2011), pp. 3828–3857.

[11] Jinxin Gao, Christopher M. Bender, and Catherine J. Murphy. “Dependence of the Gold Nanorod Aspect Ratio on the Nature of the Directing Surfactant in Aqueous Solution”. en. In: *Langmuir* 19.21 (Oct. 2003), pp. 9065–9070.

[12] Prashant K. Jain et al. “Calculated Absorption and Scattering Properties of Gold Nanoparticles of Different Size, Shape, and Composition: Applications in Biological Imaging and Biomedicine”. In: *The Journal of Physical Chemistry B* 110.14 (Apr. 1, 2006), pp. 7238–7248.

[13] Jung-Hoon Lee et al. “Bipyramid-templated synthesis of monodisperse anisotropic gold nanocrystals”. en. In: *Nature Communications* 6.1 (Dec. 2015).

[14] Julien R G Navarro et al. “Synthesis of PEGylated gold nanostars and bipyramids for intracellular uptake”. en. In: *Nanotechnology* 23.46 (Nov. 2012), p. 465602.

[15] Julien R.G. Navarro et al. “Tuning Dye-to-Particle Interactions toward Luminescent Gold Nanostars”. en. In: *Langmuir* 29.34 (Aug. 2013), pp. 10915–10921.

[16] J. R. G. Navarro et al. “Plasmonic bipyramids for fluorescence enhancement and protection against photobleaching”. en. In: *Nanoscale* 6.10 (2014), p. 5138.

[17] Sean Murphy, Libai Huang, and Prashant V. Kamat. “Charge-Transfer Complexation and Excited-State Interactions in Porphyrin-Silver Nanoparticle Hybrid Structures”. en. In: *The Journal of Physical Chemistry C* 115.46 (Nov. 2011), pp. 22761–22769.

[18] Denis Mongin et al. “Ultrafast Photoinduced Charge Separation in Metal–Semiconductor Nanohybrids”. en. In: *ACS Nano* 6.8 (Aug. 2012), pp. 7034–7043.

[19] Peng Wang et al. “Plasmonic photocatalysts: harvesting visible light with noble metal nanoparticles”. In: *Physical Chemistry Chemical Physics* 14.28 (June 27, 2012), pp. 9813–9825.

[20] Manda Xiao et al. “Plasmon-enhanced chemical reactions”. In: *Journal of Materials Chemistry A* 1.19 (Apr. 23, 2013), pp. 5790–5805.

[21] Ewa Kowalska et al. “Visible-light-induced photocatalysis through surface plasmon excitation of gold on titania surfaces”. In: *Physical Chemistry Chemical Physics* 12.10 (Feb. 24, 2010), pp. 2344–2355.

[22] Andiappan Marimuthu, Jianwen Zhang, and Suljo Linic. “Tuning Selectivity in Propylene Epoxidation by Plasmon Mediated Photo-Switching of Cu Oxidation State”. In: *Science* 339.6127 (Mar. 29, 2013), pp. 1590–1593.

[23] Suljo Linic, Phillip Christopher, and David B. Ingram. “Plasmonic-metal nanostructures for efficient conversion of solar to chemical energy”. In: *Nature Materials* 10.12 (Dec. 2011), pp. 911–921.

[24] Yasuhiro Tachibana, Lionel Vayssieres, and James R. Durrant. “Artificial photosynthesis for solar water-splitting”. In: *Nature Photonics* 6.8 (Aug. 2012), pp. 511–518.

[25] Bijith D. Mankidy, Babu Joseph, and Vinay K. Gupta. “Photo-conversion of CO2using titanium dioxide: enhancements by plasmonic and co-catalytic nanoparticles”. In: *Nanotechnology* 24.40 (Sept. 2013), p. 405402.

[26] Jun-Cao Bian et al. “Mechanisms in photoluminescence enhancement of ZnO nanorod arrays by the localized surface plasmons of Ag nanoparticles”. en. In: *Applied Surface Science* 258.22 (Sept. 2012), pp. 8548–8551.

[27] H. Y. Lin et al. “Carrier transfer induced photoluminescence change in metal-semiconductor core-shell nanostructures”. In: *Applied Physics Letters* 88.16 (Apr. 17, 2006), p. 161911.

[28] Wenjie Dong et al. “Facile Synthesis of Monodisperse Superparamagnetic Fe3O4 Core@hybrid@Au Shell Nanocomposite for Bimodal Imaging and Photothermal Therapy”. In: *Advanced Materials* 23.45 (2011), pp. 5392–5397.

[29] Xuandong Wang et al. “Multifunctional Fe3O4@P(St/MAA)@Chitosan@Au Core/Shell Nanoparticles for Dual Imaging and Photothermal Therapy”. In: *ACS Applied Materials & Interfaces* 5.11 (June 12, 2013), pp. 4966–4971.

[30] Zhongbiao Tian et al. “A novel biomass coated Ag–TiO2 composite as a photoanode for enhanced photocurrent in dye-sensitized solar cells”. In: *RSC Advances* 3.18 (Apr. 16, 2013), pp. 6369–6376.

[31] Jifa Qi et al. “Highly Efficient Plasmon-Enhanced Dye-Sensitized Solar Cells through Metal@Oxide Core–Shell Nanostructure”. In: *ACS Nano* 5.9 (Sept. 27, 2011), pp. 7108–7116.

[32] Shuai Chang et al. “Enhancement of low energy sunlight harvesting in dye-sensitized solar cells using plasmonic gold nanorods”. In: *Energy & Environmental Science* 5.11 (Oct. 18, 2012), pp. 9444–9448.

[33] Peter Atkins, Julio de Paula, and James Keeler. *Atkins' Physical Chemistry*. Eleventh Edition. Oxford, New York: Oxford University Press, Dec. 28, 2017. 944 pp.

[34] Jerzy Leszczynski et al., eds. *Handbook of Computational Chemistry*. 2nd ed. Springer International Publishing, 2017.

[35] Miguel A. L. Marques et al., eds. *Fundamentals of Time-Dependent Density Functional Theory*. Lecture Notes in Physics. Berlin Heidelberg: Springer-Verlag, 2012.

[36] Jacopo Tomasi and Maurizio Persico. “Molecular Interactions in Solution: An Overview of Methods Based on Continuous Distributions of the Solvent”. In: *Chemical Reviews* 94.7 (Nov. 1, 1994), pp. 2027–2094.

[37] R. Cammi and J. Tomasi. “Remarks on the use of the apparent surface charges (ASC) methods in solvation problems: Iterative versus matrix-inversion procedures and the renormalization of the apparent charges”. In: *Journal of Computational Chemistry* 16.12 (1995), pp. 1449–1458.

[38] B. Mennucci, E. Cancès, and J. Tomasi. “Evaluation of Solvent Effects in Isotropic and Anisotropic Dielectrics and in Ionic Solutions with a Unified Integral Equation Method: Theoretical Bases, Computational Implementation, and Numerical Applications”. In: *The Journal of Physical Chemistry B* 101.49 (Dec. 1, 1997), pp. 10506–10517.

[39] B. Mennucci et al. “Polarizable Continuum Model (PCM) Calculations of Solvent Effects on Optical Rotations of Chiral Molecules”. In: *The Journal of Physical Chemistry A* 106.25 (June 1, 2002), pp. 6102–6113.

[40] Jacopo Tomasi, Benedetta Mennucci, and Roberto Cammi. “Quantum Mechanical Continuum Solvation Models”. In: *Chemical Reviews* 105.8 (2005), pp. 2999–3094.

[41] Christopher J. Cramer and Donald G. Truhlar. “A Universal Approach to Solvation Modeling”. In: *Accounts of Chemical Research* 41.6 (June 1, 2008), pp. 760–768.

[42] Mennucci Benedetta. “Polarizable continuum model”. In: *Wiley Interdisciplinary Reviews: Computational Molecular Science* 2.3 (Jan. 2012), pp. 386–404.

[43] Stefano Baroni. “Electronic structure and quantum simulation of materials”. 2016.

[44] S. Miertuš, E. Scrocco, and J. Tomasi. “Electrostatic interaction of a solute with a continuum. A direct utilizaion of AB initio molecular potentials for the prevision of solvent effects”. In: *Chemical Physics* 55.1 (Feb. 1, 1981), pp. 117–129.

[45] M. A. Ordal et al. “Optical properties of the metals Al, Co, Cu, Au, Fe, Pb, Ni, Pd, Pt, Ag, Ti, and W in the infrared and far infrared”. en. In: *Applied Optics* 22.7 (Apr. 1983), p. 1099.

[46] Bruce T. Draine and Piotr J. Flatau. “Discrete-Dipole Approximation For Scattering Calculations”. en. In: *Journal of the Optical Society of America A* 11.4 (Apr. 1994), p. 1491.

[47] J. Sinzig and M. Quinten. “Scattering and absorption by spherical multilayer particles”. en. In: *Applied Physics A Solids and Surfaces* 58.2 (Feb. 1994), pp. 157–162.

[48] Uwe Kreibig and Michael Vollmer. *Optical Properties of Metal Clusters*. en. Springer Series in Materials Science. Berlin Heidelberg: Springer-Verlag, 1995.

[49] Stefan Alexander Maier. *Plasmonics: Fundamentals and Applications*. en. Springer US, 2007.

[50] Michael Quinten. *Optical Properties of Nanoparticle Systems: Mie and beyond*. en. Weinheim, Germany: Wiley-VCH Verlag GmbH & Co. KGaA, Jan. 2011.

[51] P. G. Etchegoin, E. C. Le Ru, and M. Meyer. “An analytic model for the optical properties of gold”. In: *The Journal of Chemical Physics* 125.16 (Oct. 2006), p. 164705.

[52] P. G. Etchegoin, E. C. Le Ru, and M. Meyer. ““Erratum: An analytic model for the optical properties of gold” [J. Chem. Phys. 125, 164705 (2006)]”. In: *The Journal of Chemical Physics* 127.18 (Nov. 2007), p. 189901.

[53] Arunima Coomar et al. “Near-field: A finite-difference time-dependent method for simulation of electrodynamics on small scales”. In: *The Journal of Chemical Physics* 135.8 (Aug. 2011), p. 084121.

[54] H. C. van de Hulst. “Light scattering by small particles”. In: *Quarterly Journal of the Royal Meteorological Society* 84.360 (1981), pp. 198–199.

[55] C. Bohren and D. Huffman. *Absorption and Scattering of Light by Small Particles*. Wiley.com. 1998.

[56] Michael I. Mishchenko, L. Travis, and Andrew Lacis. *Scattering, Absorption, and Emission of Light by Small Particles*. Vol. 4. Jan. 1, 2002.

[57] Tuck C. Choy. *Effective Medium Theory: Principles and Applications*. Oxford University Press, Dec. 1, 2015.

[58] Eric Cancès and Benedetta Mennucci. "New applications of integral equations methods for solvation continuum models: ionic solutions and liquid crystals". In: *Journal of Mathematical Chemistry* 23.3 (1998), pp. 309–326.

[59] Claudio Amovilli et al. "Recent Advances in the Description of Solvent Effects with the Polarizable Continuum Model". In: ed. by Per-Olov Löwdin. Vol. 32. Advances in Quantum Chemistry. ISSN: 0065-3276. Academic Press, 1998, pp. 227–261.

[60] Walt A. de Heer. "The physics of simple metal clusters: experimental aspects and simple models". In: *Reviews of Modern Physics* 65.3 (July 1993), pp. 611–676.

[61] Oliver D. Häberlen et al. "From clusters to bulk: A relativistic density functional investigation on a series of gold clusters Aun, n=6,...,147". In: *The Journal of Chemical Physics* 106.12 (Mar. 1997), pp. 5189–5201.

[62] J. P. Wilcoxon et al. "Photoluminescence from nanosize gold clusters". In: *The Journal of Chemical Physics* 108.21 (May 1998), pp. 9137–9143.

[63] Hannu Häkkinen, Michael Moseler, and Uzi Landman. "Bonding in Cu, Ag, and Au Clusters: Relativistic Effects, Trends, and Surprises". In: *Physical Review Letters* 89.3 (June 2002), p. 033401.

[64] Hannu Häkkinen et al. "On the Electronic and Atomic Structures of Small Au $_N$ $^-$ (N = 414) Clusters: A Photoelectron Spectroscopy and Density-Functional Study". en. In: *The Journal of Physical Chemistry A* 107.32 (Aug. 2003), pp. 6168–6175.

[65] Fernández E. M. et al. "Trends in the structure and bonding of neutral and charged noble metal clusters". In: *International Journal of Quantum Chemistry* 101.6 (Oct. 2004), pp. 740–745.

[66] Wei Fa, Chuanfu Luo, and Jinming Dong. "Bulk fragment and tubelike structures of ${\mathrm{Au}}_{N}$ $(N=2\text{\ensuremath{-}}26)$". In: *Physical Review B* 72.20 (Nov. 2005), p. 205428.

[67] A. V. Walker. "Structure and energetics of small gold nanoclusters and their positive ions". In: *The Journal of Chemical Physics* 122.9 (Mar. 2005), p. 094310.

[68] Ajanta Deka and Ramesh C. Deka. "Structural and electronic properties of stable Aun (n=2–13) clusters: A density functional study". In: *Journal of Molecular Structure: THEOCHEM* 870.1 (Dec. 2008), pp. 83–93.

[69] Robertson W. Burgess and Vicki J. Keast. "TDDFT Study of the Optical Absorption Spectra of Bare Gold Clusters". In: *The Journal of Physical Chemistry C* 118.6 (Feb. 2014), pp. 3194–3201.

[70] Luiz F. L. Oliveira et al. "Benchmarking Density Functional Based Tight-Binding for Silver and Gold Materials: From Small Clusters to Bulk". In: *The Journal of Physical Chemistry A* 120.42 (Oct. 2016), pp. 8469–8483.

[71] Xi-Bo Li et al. “Size dependence of the structures and energetic and electronic properties of gold clusters”. In: *The Journal of Chemical Physics* 126.8 (Feb. 2007), p. 084505.

[72] P. Giannozzi et al. “Advanced capabilities for materials modelling with Quantum ESPRESSO”. In: *Journal of Physics: Condensed Matter* 29.46 (Oct. 2017), p. 465901.

[73] Nicola Marzari et al. “Thermal Contraction and Disordering of the Al(110) Surface”. In: *Physical Review Letters* 82.16 (Apr. 19, 1999), pp. 3296–3299.

[74] Dario Rocca et al. “Turbo charging time-dependent density-functional theory with Lanczos chains”. In: *The Journal of Chemical Physics* 128.15 (Apr. 16, 2008). Publisher: American Institute of Physics, p. 154105.

[75] Osman Barış Malcıoğlu et al. “turboTDDFT – A code for the simulation of molecular spectra using the Liouville–Lanczos approach to time-dependent density-functional perturbation theory”. In: *Computer Physics Communications* 182.8 (Aug. 1, 2011), pp. 1744–1754.

[76] Stefano Baroni and Ralph Gebauer. “The Liouville-Lanczos Approach to Time-Dependent Density-Functional (Perturbation) Theory”. In: *Fundamentals of Time-Dependent Density Functional Theory*. Ed. by Miguel A.L. Marques et al. Lecture Notes in Physics. Berlin, Heidelberg: Springer, 2012, pp. 375–390.

[77] Julien R.G. Navarro et al. “Nanocarriers with ultrahigh chromophore loading for fluorescence bio-imaging and photodynamic therapy”. en. In: *Biomaterials* 34.33 (Nov. 2013), pp. 8344–8351.

[78] P. Törmä and W. L. Barnes. “Strong coupling between surface plasmon polaritons and emitters: a review”. en. In: *Reports on Progress in Physics* 78.1 (Dec. 2014), p. 013901.

[79] Joseph R. Lakowicz. “Radiative decay engineering 5: metal-enhanced fluorescence and plasmon emission”. en. In: *Analytical Biochemistry* 337.2 (Feb. 2005), pp. 171–194.

[80] Chris D. Geddes and Joseph R. Lakowicz. “Editorial: Metal-Enhanced Fluorescence”. en. In: *Journal of Fluorescence* 12.2 (June 2002), pp. 121–129.

[81] P. P. Pompa et al. “Metal-enhanced fluorescence of colloidal nanocrystals with nanoscale control”. en. In: *Nature Nanotechnology* 1.2 (Nov. 2006), pp. 126–130.

[82] Tapan K. Sau et al. “Properties and Applications of Colloidal Nonspherical Noble Metal Nanoparticles”. en. In: *Advanced Materials* 22.16 (Apr. 2010), pp. 1805–1825.

[83] Mingzhao Liu and Philippe Guyot-Sionnest. “Mechanism of Silver(I)-Assisted Growth of Gold Nanorods and Bipyramids”. In: *The Journal of Physical Chemistry B* 109.47 (Dec. 2005), pp. 22192–22200.

[84] Enrique Carbó-Argibay et al. “Growth of pentatwinned gold nanorods into truncated decahedra”. en. In: *Nanoscale* 2.11 (Nov. 2010), pp. 2377–2383.

[85] Anand Gole and Catherine J. Murphy. “Seed-Mediated Synthesis of Gold Nanorods: Role of the Size and Nature of the Seed”. In: *Chemistry of Materials* 16.19 (Sept. 2004), pp. 3633–3640.

[86] Soraya Zaiba et al. “Transparent Plasmonic Nanocontainers Protect Organic Fluorophores against Photobleaching”. In: *Nano Letters* 11.5 (May 2011), pp. 2043–2047.

[87] Nikhil R. Jana, Latha Gearheart, and Catherine J. Murphy. “Wet Chemical Synthesis of High Aspect Ratio Cylindrical Gold Nanorods”. In: *The Journal of Physical Chemistry B* 105.19 (May 2001), pp. 4065–4067.

[88] Huanjun Chen et al. “Shape- and Size-Dependent Refractive Index Sensitivity of Gold Nanoparticles”. In: *Langmuir* 24.10 (May 2008), pp. 5233–5237.

[89] Jean Lermé et al. “Size Dependence of the Surface Plasmon Resonance Damping in Metal Nanospheres”. In: *The Journal of Physical Chemistry Letters* 1.19 (Oct. 2010), pp. 2922–2928.

[90] Nadia Grillet et al. “Plasmon Coupling in Silver Nanocube Dimers: Resonance Splitting Induced by Edge Rounding”. en. In: *ACS Nano* 5.12 (Dec. 2011), pp. 9450–9462.

[91] Benedetta Mennucci and Stefano Corni. “Multiscale modelling of photoinduced processes in composite systems”. en. In: *Nature Reviews Chemistry* 3.5 (May 2019), pp. 315–330.

[92] S. Corni and J. Tomasi. “Enhanced response properties of a chromophore physisorbed on a metal particle”. In: *The Journal of Chemical Physics* 114.8 (Feb. 2001), pp. 3739–3751.

[93] S. Corni and J. Tomasi. “Surface enhanced Raman scattering from a single molecule adsorbed on a metal particle aggregate: A theoretical study”. In: *The Journal of Chemical Physics* 116.3 (Dec. 2001), pp. 1156–1164.

[94] Marco Caricato, Oliviero Andreussi, and Stefano Corni. “Semiempirical (ZINDO-PCM) Approach to Predict the Radiative and Nonradiative Decay Rates of a Molecule Close to Metal Particles”. en. In: *The Journal of Physical Chemistry B* 110.33 (Aug. 2006), pp. 16652–16659.

[95] Sinisa Vukovic, Stefano Corni, and Benedetta Mennucci. “Fluorescence Enhancement of Chromophores Close to Metal Nanoparticles. Optimal Setup Revealed by the Polarizable Continuum Model”. en. In: *The Journal of Physical Chemistry C* 113.1 (Jan. 2009), pp. 121–133.

[96] Oliviero Andreussi et al. “Plasmon-Controlled Light-Harvesting: Design Rules for Biohybrid Devices via Multiscale Modeling”. en. In: *Nano Letters* 13.9 (Sept. 2013), pp. 4475–4484.

[97] Mahmoud A. Mahmoud and Mostafa A. El-Sayed. “Gold Nanoframes: Very High Surface Plasmon Fields and Excellent Near-Infrared Sensors”. In: *Journal of the American Chemical Society* 132.36 (Sept. 2010), pp. 12704–12710.

[98] Feng Hao et al. “Plasmon Resonances of a Gold Nanostar”. In: *Nano Letters* 7.3 (Mar. 2007), pp. 729–732.

[99] Andrés Guerrero-Martínez et al. “Nanostars shine bright for you: Colloidal synthesis, properties and applications of branched metallic nanoparticles”. en. In: *Current Opinion in Colloid & Interface Science* 16.2 (Apr. 2011), pp. 118–127.

[100] Hong Wei et al. “Quantum Dot-Based Local Field Imaging Reveals Plasmon-Based Interferometric Logic in Silver Nanowire Networks”. In: *Nano Letters* 11.2 (Feb. 2011), pp. 471–475.

[101] Eric C. Le Ru et al. “A Scheme for Detecting Every Single Target Molecule with Surface-Enhanced Raman Spectroscopy”. In: *Nano Letters* 11.11 (Nov. 2011), pp. 5013–5019.

[102] Xiaoshan Kou et al. “Growth of Gold Bipyramids with Improved Yield and Their Curvature-Directed Oxidation”. en. In: *Small* 3.12 (Dec. 2007), pp. 2103–2113.

[103] Julien R G Navarro et al. “Synthesis, electron tomography and single-particle optical response of twisted gold nano-bipyramids”. en. In: *Nanotechnology* 23.14 (Apr. 2012), p. 145707.

[104] Santosh Kumar Meena and Marialore Sulpizi. “From Gold Nanoseeds to Nanorods: The Microscopic Origin of the Anisotropic Growth”. In: *Angewandte Chemie International Edition* 55.39 (Aug. 2016), pp. 11960–11964.

[105] Stephan Link and Mostafa A. El-Sayed. “Spectral Properties and Relaxation Dynamics of Surface Plasmon Electronic Oscillations in Gold and Silver Nanodots and Nanorods”. In: *The Journal of Physical Chemistry B* 103.40 (Oct. 1999), pp. 8410–8426.

[106] Boris Khlebtsov et al. “A New T-Matrix Solvable Model for Nanorods: TEM-Based Ensemble Simulations Supported by Experiments”. In: *The Journal of Physical Chemistry C* 115.14 (Apr. 2011), pp. 6317–6323.

[107] Benjamin Saute and Radha Narayanan. “Solution-based direct readout surface enhanced Raman spectroscopic (SERS) detection of ultra-low levels of thiram with dogbone shaped gold nanoparticles”. en. In: *Analyst* 136.3 (Jan. 2011), pp. 527–532.

[108] Huanjun Chen et al. “Gold nanorods and their plasmonic properties”. en. In: *Chemical Society Reviews* 42.7 (Mar. 2013), pp. 2679–2724.

[109] Z. Cansu Canbek et al. “Twinned Gold Nanoparticles under Growth: Bipyramids Shape Controlled by Environment”. In: *Crystal Growth & Design* 15.8 (2015), pp. 3637–3644.

[110] García de Abajo, F. J., and A. Howie. “Retarded field calculation of electron energy loss in inhomogeneous dielectrics”. In: *Physical Review B* 65.11 (Mar. 2002), p. 115418.

[111] Viktor Myroshnychenko et al. “Modelling the optical response of gold nanoparticles”. en. In: *Chemical Society Reviews* 37.9 (Aug. 2008), pp. 1792–1805.

[112] Ulrich Hohenester and Andreas Trügler. “MNPBEM – A Matlab toolbox for the simulation of plasmonic nanoparticles”. en. In: *Computer Physics Communications* 183.2 (Feb. 2012), pp. 370–381.

[113] M. T. Homer Reid. "scuff-em: A comprehensive and full-featured computational physics suite for boundary-element analysis". In: (Mar. 2018). http://github.com/homerr

[114] Luca Bergamini and Stefano Corni. "Benchmarking Common Approximations for Determining the Particle-Size Dependence of Adsorbate-Induced Localized Surface Plasmon Resonance Shifts". In: *The Journal of Physical Chemistry C* 117.28 (July 2013), pp. 14742–14750.

[115] Luca Bursi et al. "Quantifying the Plasmonic Character of Optical Excitations in Nanostructures". en. In: *ACS Photonics* 3.4 (Apr. 2016), pp. 520–525.

[116] Luca Bursi et al. "Light-Induced Field Enhancement in Nanoscale Systems from First-Principles: The Case of Polyacenes". In: *ACS Photonics* 1.10 (Oct. 2014), pp. 1049–1058.

[117] G. Gil et al. "Excitation energy-transfer in functionalized nanoparticles: Going beyond the Förster approach". In: *The Journal of Chemical Physics* 144.7 (Feb. 2016), p. 074101.

[118] Silvio Pipolo and Stefano Corni. "Real-Time Description of the Electronic Dynamics for a Molecule Close to a Plasmonic Nanoparticle". en. In: *The Journal of Physical Chemistry C* 120.50 (Dec. 2016), pp. 28774–28781.

[119] M. T. Homer Reid and Steven G. Johnson. "Efficient Computation of Power, Force, and Torque in BEM Scattering Calculations". In: *IEEE Transactions on Antennas and Propagation* 63.8 (Aug. 2015), pp. 3588–3598.

[120] Christophe Geuzaine and Jean-François Remacle. "Gmsh: A 3-D finite element mesh generator with built-in pre- and post-processing facilities". en. In: *International Journal for Numerical Methods in Engineering* 79.11 (Sept. 2009), pp. 1309–1331.

[121] Johannes Schindelin et al. "The ImageJ ecosystem: An open platform for biomedical image analysis". en. In: *Molecular Reproduction and Development* 82.7-8 (2015), pp. 518–529.

[122] Henk G. Merkus. *Particle Size Measurements: Fundamentals, Practice, Quality*. en. Particle Technology Series. Springer Netherlands, 2009.

[123] Martin Moskovits. "Surface-enhanced spectroscopy". In: *Reviews of Modern Physics* 57.3 (July 1, 1985), pp. 783–826.

[124] Alan Campion and Patanjali Kambhampati. "Surface-enhanced Raman scattering". In: *Chemical Society Reviews* 27.4 (Jan. 1, 1998), pp. 241–250.

[125] Peter Johansson, Hongxing Xu, and Mikael Käll. "Surface-enhanced Raman scattering and fluorescence near metal nanoparticles". In: *Physical Review B* 72.3 (July 8, 2005), p. 035427.

[126] Pascal Anger, Palash Bharadwaj, and Lukas Novotny. "Enhancement and Quenching of Single-Molecule Fluorescence". In: *Physical Review Letters* 96.11 (Mar. 21, 2006), p. 113002.

[127] Sergei Kühn et al. "Enhancement of Single-Molecule Fluorescence Using a Gold Nanoparticle as an Optical Nanoantenna". In: *Physical Review Letters* 97.1 (July 7, 2006), p. 017402.

[128] Prabhat K. K. Pandey and George C. Schatz. “A detailed analysis of the Raman enhancement mechanisms associated with the interaction of a Raman scatterer with a resonant metal cluster: Results for Lin–H2”. In: *The Journal of Chemical Physics* 80.6 (Mar. 15, 1984), pp. 2959–2972.

[129] Hiromi Nakai and Hiroshi Nakatsuji. “Electronic mechanism of the surface enhanced Raman scattering”. In: *The Journal of Chemical Physics* 103.6 (Aug. 8, 1995), pp. 2286–2294.

[130] Joshua W. Gibson and Bruce R. Johnson. “Density-matrix calculation of surface-enhanced Raman scattering for p-mercaptoaniline on silver nanoshells”. In: *The Journal of Chemical Physics* 124.6 (Feb. 8, 2006), p. 064701.

[131] Lasse Jensen, Christine M. Aikens, and George C. Schatz. “Electronic structure methods for studying surface-enhanced Raman scattering”. In: *Chemical Society Reviews* 37.5 (Apr. 29, 2008), pp. 1061–1073.

[132] Mohamed Haggui et al. “Spatial Confinement of Electromagnetic Hot and Cold Spots in Gold Nanocubes”. In: *ACS Nano* 6.2 (Feb. 28, 2012), pp. 1299–1307.

[133] Santosh Kumar Meena et al. “The role of halide ions in the anisotropic growth of gold nanoparticles: a microscopic, atomistic perspective”. en. In: *Physical Chemistry Chemical Physics* 18.19 (2016), pp. 13246–13254.

[134] B. L. Darby et al. “Modified optical absorption of molecules on metallic nanoparticles at sub-monolayer coverage”. In: *Nat. Photonics* 10 (2016), p. 40.

[135] Baptiste Auguié and Eric C. Le Ru. “Optical Absorption of Dye Molecules in a Spherical Shell Geometry”. In: *The Journal of Physical Chemistry C* 122.33 (Aug. 23, 2018). Publisher: American Chemical Society, pp. 19110–19115.

[136] Alina Umerbekova et al. “Dissecting energy level renormalization and polarizability enhancement of molecules at surfaces with subsystem TDDFT”. In: *The European Physical Journal B* 91.10 (Oct. 1, 2018), p. 214.